Wesleyan University The Honors College

The Shadows of Distant Worlds: Exoplanetary Transit Timing Using the Perkin Telescope

by

Marshall C. Johnson
Class of 2011

A thesis submitted to the
faculty of Wesleyan University
in partial fulfillment of the requirements for the
Degree of Bachelor of Arts
with Departmental Honors in Astronomy

Middletown, Connecticut April, 2011

"Astronomy compels the soul to look upwards and leads us from this world to another."

–Plato

Acknowledgments

Let me thank first and foremost my advisor, Seth Redfield, who has been an amazing guide and mentor over the past few years as I have made my way into the field of exoplanetary science. Thank you for providing the opportunity to work on this project and for your patient help and suggestions, for taking me observing at McDonald Observatory and sending me to present an early version of these results at the American Astronomical Society meeting in Seattle.

Thanks to John Filhaber for donating his time and energy to aid with the polar alignment and general maintenance of the telescope; without you this work would not have been possible and the telescope would be in poorer condition. Thanks also to David Kipping, John Asher Johnson, and Eliza Miller-Ricci Kempton for helpful suggestions regarding the error analysis at the AAS meeting.

On a more personal note, I'd like to thank my family and all of my friends here at Wesleyan for supporting me during long hours of hard work on this thesis and for proofreading the manuscript. Thesis aside, thank you for an amazing four years here; and to the good people of 80 Lawn, for being a terrific senior house.

Thanks to my fellow astronomy students for levity amidst the long days of work, and especially to all of those who have been part of the Redfield research group over the years; thank you for productive discussions and help with problems large and small. Thanks also to all of the 24" student observers, without whom I would have much less data; special thanks to Tyler Desjardins and Karlen Shahinyan for observing above and beyond the call of duty.

This work was funded by an Undergraduate Fellowship from the NASA CT Space Grant Consortium, and made use of NASA's Astrophysics Data System Bibliographic Services.

Contents

Chapter 1

Introduction

For thousands of years humans have hypothesized that planets should exist around other stars, but it is only in the last twenty years that such planets have actually been detected. The ancient Greek philosopher Epicurus argued that an infinity of atoms implied an infinity of worlds like the Earth (Epicurus 300 B.C.E.). Almost two thousand years later, the Italian astronomer Giordano Bruno was condemned by the Inquisition and burned at the stake for proposing that the universe was infinite and that an infinity of other planets existed around other stars (Bruno 1584). Fortunately more recent exoplanetary scientists have suffered rather less harsh treatment at the hands of their critics.

By the nineteenth century the concept of planets around others stars had started to be widely accepted, and some claims of discoveries were even made, although these were all later refuted. For instance, Jacob (1855) claimed to have discovered a planet around one of the stars in the nearby binary system 70 Ophiuchi through slight deviations of the stars from their predicted orbit (see §1.1.3 for more detail on the astrometric method).

Perhaps the most well-known claim of a planetary discovery is that of van de Kamp (1963), whose data appeared to show a planet, later revised to two planets (van de Kamp 1969), in orbit around the nearby M dwarf Barnard's Star. Other observers, however, found no evidence for such planets, refuting the claim (e.g.,

Gatewood & Eichhorn 1973)[1].

When the first confirmed detection of a planetary system finally came in 1992, it was in an unexpected location. Wolszczan & Frail (1992) reported the discovery of two planets around a pulsar, an ultra-compact supernova remnant. Only three more years passed before the first bona fide detection of a planet around a main sequence star, and this, too, brought a surprise: Mayor & Queloz (1995) announced the discovery of a gas giant planet in an extremely close orbit (0.052 AU) around the G2 star 51 Pegasi. This system was obviously very different from our solar system, where all of the gas and ice giants lie far from the star, beyond the snow line.

Over the nearly twenty years since these discoveries, the number of known exoplanets has soared. Currently the Extrasolar Planets Encyclopaedia (Schneider 2011) lists more than 500 confirmed planets, while the *Kepler* mission team recently released more than 1200 planetary candidates (Borucki et al. 2011), some with radii as small as the Earth, and others located in the habitable zones of cool K dwarfs.

This recent bonanza of planetary discoveries has come with many more surprises and intriguing systems: a star with up to seven planets (Lovis et al. 2011), planets with extremely eccentric orbits (e.g., Naef et al. 2001), a massive system with planets extremely far from their host star (Marois et al. 2010), and many more. Clearly exoplanetary science is now entering a golden age, with a multitude of known and to-be-confirmed planets, and many techniques for follow-up observations and characterization of known planets. In the following sections I will describe the various discovery and characterization techniques currently in

[1]Historical footnote: some of the data used by Gatewood & Eichhorn (1973) were obtained on Van Vleck Observatory's 20-inch refractor.

use and proposed for future use.

1.1 Detection Methods

1.1.1 Imaging

Perhaps the most conceptually straightforward, and yet one of the most practically difficult methods of planetary discovery, is simply to directly image the planet. While determining whether a candidate planet is indeed bound to its host star is a simple matter—it is observed at several epochs in order to make sure that it follows a similar path across the sky as the star—determining its mass is significantly more difficult. The observed flux from the candidate planet is compared to evolutionary models of gas giant planets detailing how the infrared flux evolves as a function of age. In order to use this method the age of the system, usually determined from the star, needs to be known. This is a difficult and imprecise process, leading to an often significant uncertainty in the mass of the planet. In some cases it can even be unclear if the object is massive enough to have sustained deuterium fusion, and thus is a brown dwarf, and not a planet at all. For instance, the uncertainty in the mass of the recently-discovered planet HR 8799e is, depending upon the stellar age adopted, $\sim 50\%$ (Marois et al. 2010).

There are, however, a number of serious issues which must be overcome in order for this method to be used. As is obvious from simple visual observation of our own solar system, stars are much, much brighter than planets. In reflected light in the visible band it is straightforward to show that a Jupiter-sized planet is $\sim 10^{-9}$ times as bright as its host star. There is therefore a tremendous contrast issue that must be overcome. This can be mitigated by observing in the infrared, where thermal emission from the planet decreases the contrast ratio to $\sim 10^{-4}$;

however, this is still a challenging observation.

Due to these reasons the first direct detections of planets were around extremely faint, low-mass stars or brown dwarfs. There is some debate, however, as to whether to call these objects "planets" at all, as they likely formed through gravitational collapse, like stars, rather than through accretion in a disk, like traditional planets. The current definition of planet is that a planet is an object that is massive enough that it relaxes into hydrostatic equilibrium and substantially clears its orbital neighborhood of other objects, but is not so massive that it can sustain deuterium fusion, as brown dwarfs can. (e.g., Chauvin et al. 2004).

More recently, technical advances have allowed the direct detection of planets around higher-mass stars, even early-type stars (e.g., Kalas et al. 2008). These planets, however, are uniformly located very far from their host stars, where the wings of the stellar point spread function (PSF) have dwindled to a level where the contrast ratio is favorable. Additionally, it is generally necessary to suppress the flux of the host star, for example using a coronagraph.

Perhaps the most striking discovery of the direct imaging technique is the extraordinary system around the A5V star HR 8799 (Marois et al. 2008, 2010). Here four planets, each with $\sim 7-10$ times the mass of Jupiter, orbit at distances of $\sim 15-70$ AU from the host star, as shown in Fig. 1.1. As Marois et al. (2010) note, it is a challenge for current models of planet formation to produce so many very massive planets so far from a star. This is also a promising system for follow-up observations; for instance, Janson et al. (2010) have obtained a spectrum of HR 8799c, which suggests the existence of dust and/or non-equilibrium chemistry in the planetary atmosphere.

Future space-based missions, such as the *James Webb Space Telescope* (*JWST*), currently scheduled for launch around 2015, could greatly expand the range of tar-

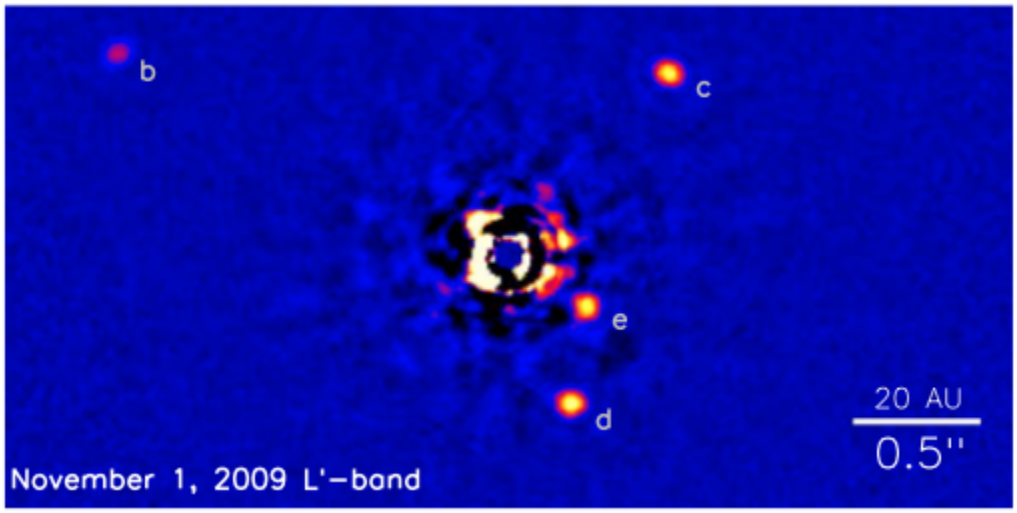

Figure 1.1: Near infrared image of the four planets orbiting HR 8799, Fig. 4 of Marois et al. (2010). The flux from the star has been suppressed, revealing the planets.

gets which can be observed via this method, especially around nearby stars.

1.1.2 Radial Velocity

Since the discovery of 51 Pegasi b (Mayor & Queloz 1995) via the radial velocity technique, this has been the dominant technique for the discovery of exoplanets (though it is starting to be eclipsed[2] by *Kepler* and the transit method). This method works by taking high-precision spectra of a star over a period of time. The planet exerts a small but non-negligible force on its host star as it orbits, causing the star to "wobble" back and forth slightly. The Doppler shift from the component of this motion along the line of sight can be detected using these high-precision spectra. Jupiter-mass planets produce stellar motions of ~ 100 m s^{-1}; the signals of Earth-mass planets would be ~ 10 cm s^{-1}.

The radial velocity method is most sensitive to massive planets close to their host stars, as these planets produce the greatest motion in the host star. Thus it

[2]Pun intended.

has turned up many "hot jupiters," i.e., massive gas giants orbiting within ~ 0.1 AU of their host star, like 51 Peg b. The radial velocity curve of 51 Peg b is shown in Fig. 1.2.

One disadvantage of the radial velocity method is that rather than delivering the mass m of a planet, it only delivers a lower limit on the mass, $m \sin i$, where i is the inclination of the planetary orbit relative to the line of sight (specifically, the sky-projected angle between the normal vector to the planet's orbital plane and the line of sight). This is because a given observed radial velocity variation of the host star could be caused either by a less massive planet on an orbit tilted near to the line of sight, or by a more massive object on an inclined orbit, where a smaller proportion of the total motion is directed along the line of sight. However, for some objects this degeneracy can be broken through the use of a second observation method to follow up on the discovery, as described in the next two sections.

1.1.3 Astrometry

Astrometry is in many ways complementary to the radial velocity method: it, too, exploits the reflex motion of a host star, but in the plane of the sky rather than along the line of sight. Essentially, the star is imaged periodically and its position calculated relative to background stars. The motion of the star relative to the sun will cause motion along a straight line, but if there is an orbiting planet the star will appear to wobble slightly around this trajectory. These observations are challenging due to the small size of the induced wobble, on the order of milliarcseconds.

This conceptually simple method was the first to be used to search for planets, even decades ago (Jacob 1855; van de Kamp 1963), but has yet to detect any

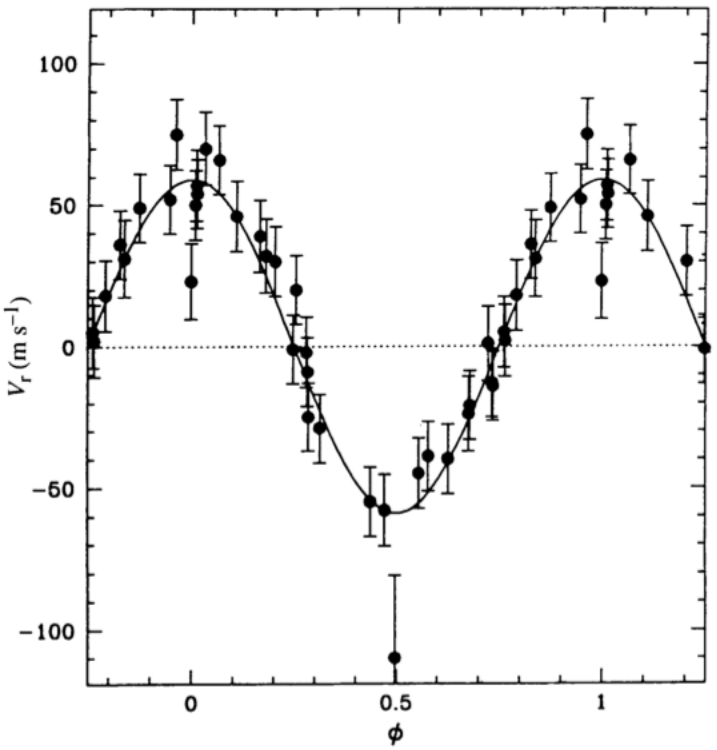

Figure 1.2: Phased radial velocity curve of 51 Peg, showing the reflex motion caused by 51 Peg b (Fig. 1 from Mayor & Queloz 1995).

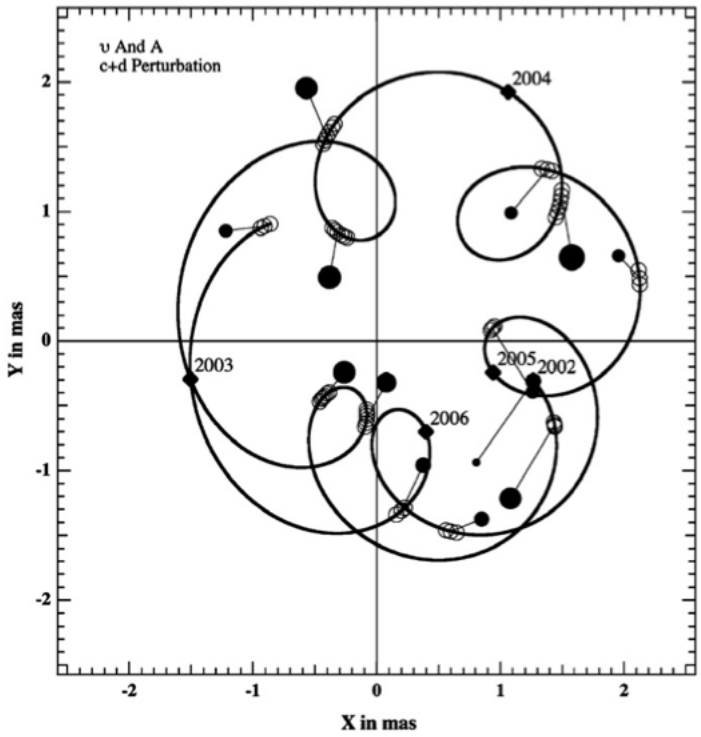

Figure 1.3: Astrometric reflex motion of υ And caused by planets c and d (Fig. 10 of McArthur et al. 2010). The solid line shows the model for the motion of the star, while the open circles denote the observations. The multi-looped structure of the curve is due to the superposed influence of two planets.

confirmed planets. It has, however, made a contribution to follow-up studies of planets detected using the radial velocity method. Astrometric detection of a planet gives the full 3-d space motion of its host star, allowing the planetary inclination to be determined, breaking the $m \sin i$ degeneracy and giving the true mass of the planet. For instance, McArthur et al. (2010) determined the true masses of the planets υ Andromedae c and d and calculated that the two planets' orbits are inclined by 29° relative to one another, a very different configuration than the largely coplanar orbits in our own solar system. The reflex motion determined in this paper is shown in Fig. 1.3.

1.1.4 Transits

The transit method relies simply on the geometry of an exoplanet's orbit. Here the planet's orbital plane is tilted such that the planet periodically passes between its host star and the Earth, blocking a small amount of the starlight, which can be detected. This dip, proportional to the planetary radius, is $\sim 1\%$ for Jupiter-sized planets, and $\sim 0.01\%$ for Earth-sized planets. The disadvantage of this method is that only a small percentage of planetary systems—those which happen to be favorably inclined relative to the line of sight—can be observed. However, the number of stars within a nearby volume of space is so large that there are still many planets which happen to transit.

There have been several successful ground-based transit detection campaigns, the most successful of which have been the Wide-Angle Search for Planets (SuperWASP, Pollacco et al. 2006) and the Hungarian Automated Telescope Network (HATNet, Bakos et al. 2004). These projects both survey wide swaths of the sky (eventually the entire sky) and are sensitive primarily to hot jupiters, but have discovered a handful of hot neptunes around small stars (e.g., Bakos et al. 2010a).

The field of transit detection has recently been revolutionized by the *Kepler* mission. *Kepler* is a 0.95-m aperture space telescope which stares continuously at a patch of sky in the constellations Cygnus and Lyra, obtaining sub-millimagnitude precision photometry on 150,000 stars at a 30-minute cadence for at least 3-4 years; at the time of this writing the mission has been ongoing for nearly two years. Designed to be able to find Earth-size planets in the habitable zones of sun-like stars, the spacecraft has already delivered more than 1200 candidate planets (Borucki et al. 2011) and fifteen confirmed planets, including a system of six planets, all transiting, around Kepler-11 (Lissauer et al. 2011a). An example

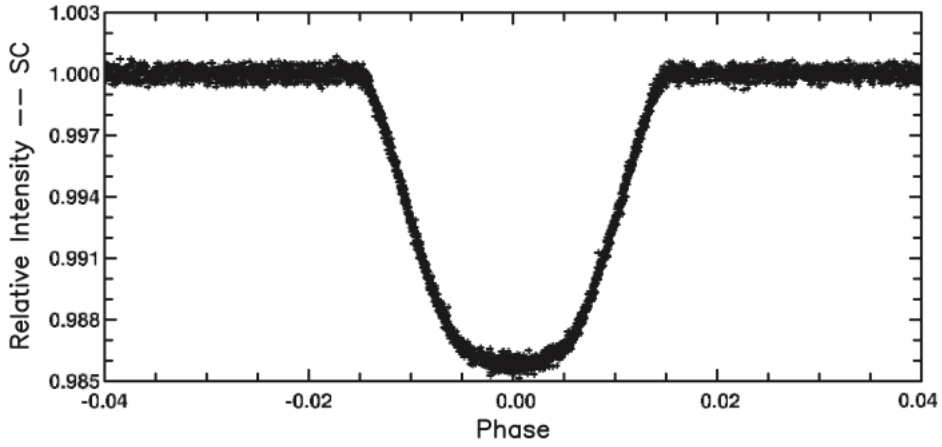

Figure 1.4: Multiple stacked transits of TrES-2b as observed by *Kepler* using short (1 minute) cadence observations (Fig. 4 from Gilliland et al. 2010).

of a *Kepler* transit lightcurve is shown in Fig. 1.4.

The transit method finds planets that are amenable to follow-up via several different techniques, as described in §1.2. Additionally, to produce a transit, the planetary orbit needs to be edge-on to the line of sight, and so the inclination can be tightly constrained; thus, with radial velocity data, the $m \sin i$ degeneracy can be broken.

However, the transit signature of a planet can be mimicked by a number of different astrophysical scenarios. For instance, a blend, where a background eclipsing binary is blended with the light of a brighter foreground star, can mimic planetary transits. Additionally, objects ranging in mass from highly inflated hot saturns to the lowest-mass M dwarfs, including brown dwarfs, can have very similar radii and so produce very similar transit signatures. Thus, it is necessary to have radial velocity follow-up observations to pin down the mass of a candidate transiting planet and confirm its planetary nature.

1.1.5 Microlensing

Microlensing relies on a prediction of Einstein's General Theory of Relativity, viz., that light is deflected in the presence of a gravitational field, which was confirmed in 1919 through observations of background stars near the sun during a solar eclipse (Dyson et al. 1920). The theory of lensing was later completed by Einstein himself (Einstein 1936).

Microlensing planet surveys operate by observing a rich distant background starfield, for instance the Galactic center. Foreground stars slowly drift across this field due to Galactic rotation. If a foreground star passes sufficiently close in projection to a bright background star, its gravitational field will focus the light from the background star. While the Einstein ring/arcs produced by this lensing are not resolved, the flux from the background star will appear to increase for a period of time before decreasing again to normal levels, resulting in a distinctive peaked lightcurve. If, however, a planet orbits the foreground lensing star, its gravity, too, will deflect the light slightly, resulting in a second peak. Multiple planets can cause complex lightcuves, like that shown in Fig. 1.5.

The planets found by microlensing are, on average, several kiloparsecs away, and in most cases the host star itself is not resolved. Indeed, it will be, on average, millions of years before a given system produces a second microlensing event, so followup is impossible for microlensing targets. However, this disadvantage is offset by the fact that the method is largely unbiased with regards to stellar type and planetary separation from the host star (once one takes into account the distribution of low-mass versus high-mass stars), allowing the accumulation of accurate statistics on the prevalence of planets.

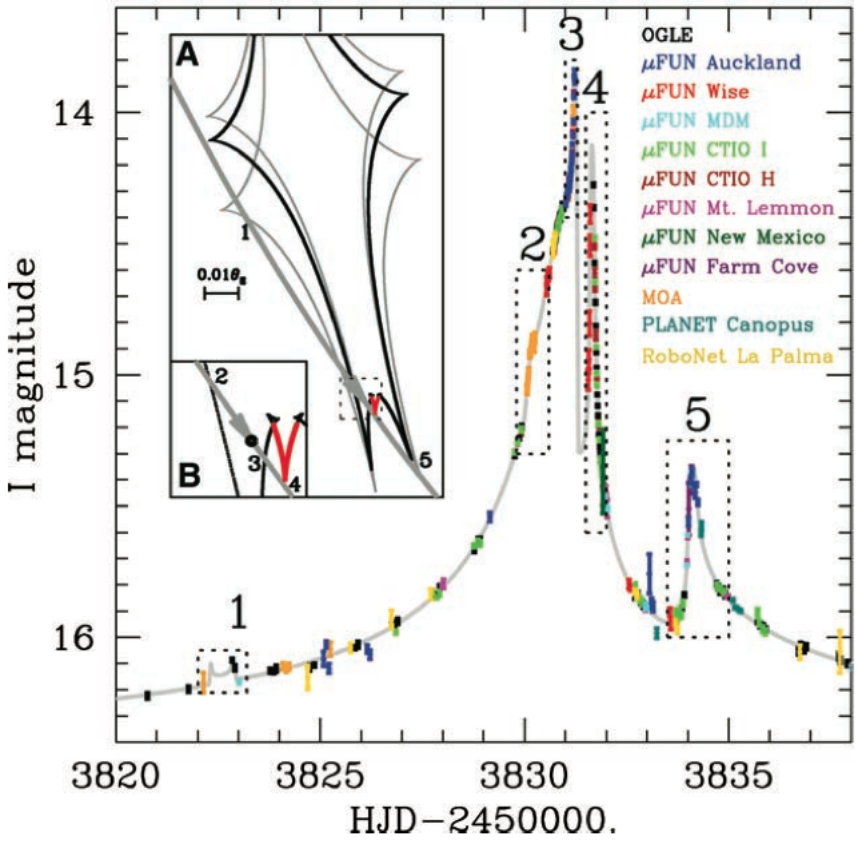

Figure 1.5: Microlensing lightcurve caused by the two planets of OGLE-2006-BLG-109 (Fig. 1 from Gaudi et al. 2008). The planetary masses, orbital radii, and equilibrium temperatures approximate a scaled-down version of Jupiter and Saturn in our own solar system. The inset shows the trajectory of the lensing star crossing a number of caustics caused by the presence of multiple planets, resulting in the sharp spikes seen in the lightcurve.

1.1.6 Timing

The timing technique was used to discover the first confirmed planets, those Wolszczan & Frail (1992) detected around a pulsar. Two varieties of the method exist, both relying upon the displacement of a body due to reflex motion. The first method makes use of displacement along the line of sight and the finite speed of light. Here the primary body must be some object which can provide a precise "clock," e.g. a spinning pulsar, short-period eclipsing binary system, or pulsating star. The reflex motion of the central star or stars causes variations in the distance between the star(s) and Earth, resulting in deviations of the observed pulse or eclipse times from regular intervals. Originally applied to pulsars, this method has detected planets around two such stars (Schneider 2011), and has recently resulted in detections of planets (even two-planet systems) around pulsating and eclipsing binary stars (e.g., Silvotti et al. 2007; Beuermann et al. 2010). The timing errors from PSR 1257+12b and -c, the first planets to be discovered, are shown in Fig. 1.6.

The second method—that of transit timing variations—can be used to detect additional planets in a system using the transits of known exoplanets, as described in §1.2.1. This technique relies upon the displacement of an object *perpendicular* to the line of sight.

1.2 Transit Follow-Up Methods

Transiting planets in particular are amenable to a wide variety of follow-up observations. One of these techniques is that of transit timing variations, which is the focus of this work.

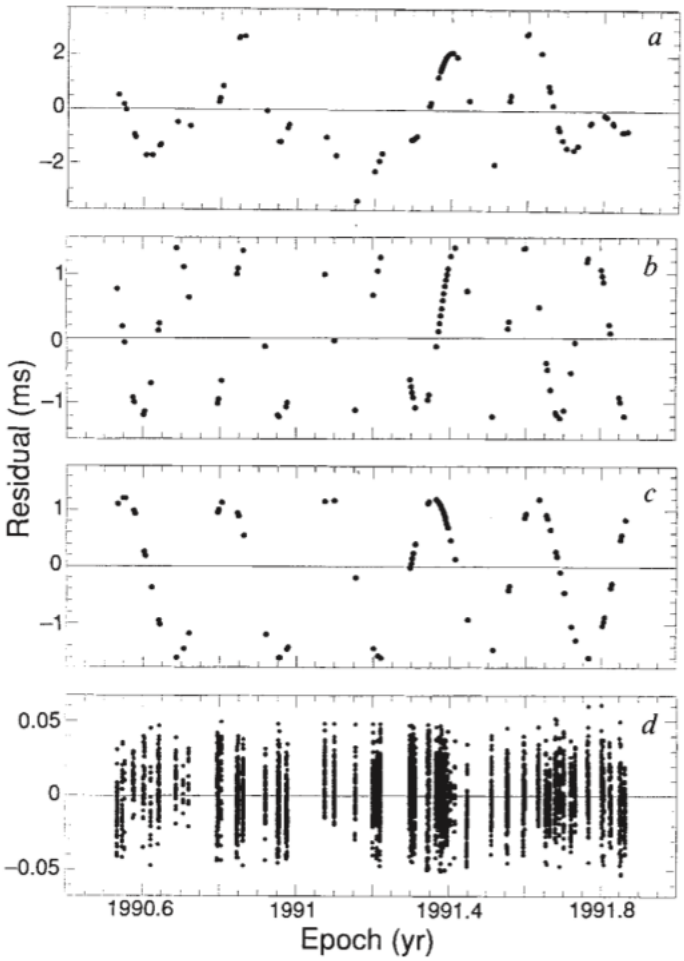

Figure 1.6: Timing errors in PSR1257+12 (Fig. 2 from Wolszczan & Frail 1992). a) The timing errors observed in the pulsar; b) and c) timing errors caused by each planet; d) residuals after the two planetary signals had been subtracted.

1.2.1 Transit Timing and Duration Variations

Exoplanet transits provide a powerful tool for probing other objects in a system. In particular, the technique of transit timing variations (TTVs; Agol et al. 2005; Holman & Murray 2005) is potentially sensitive to planets as small as the Earth in mean-motion resonances with transiting planets. This technique depends on the mutual gravitational perturbations between multiple planets orbiting the same star. If only one planet orbits a star, then its orbit will be Keplerian and its transits will occur at regular intervals. If, however, additional planets exist in the system, interactions with the transiting planet can cause the transits to deviate slightly from the expected transit ephemeris. Unlike the timing technique described in §1.1.6, TTVs are caused by the physical displacement of the planet perpendicular to the line of sight, rather than light travel time effects resulting from displacement of the star along the line of sight.

The transit timing variation method is most sensitive to planets in mean-motion resonance, as demonstrated in Figs. 1.7 and 1.8. While we would not expect many planets to lie at or near mean-motion resonances if planetary semi-major axes were distributed randomly, it appears that planetary migration preferentially results in planets which occupy mean-motion resonances—planets migrate into resonances and then are trapped in the resonance. For instance, Jupiter's moons Io, Europa, and Ganymede are locked in a 4:2:1 mean-motion resonance, and it is possible that HR 8799 e, d, and c are also in a 4:2:1 resonance. In an analysis of the multiple systems in the Borucki et al. (2011) *Kepler* dataset, Lissauer et al. (2011b) find that a significant number of systems lie near mean-motion resonances, especially the 2:1 resonance. It thus seems likely that a large number of transiting systems could show transit timing variations due to a companion in

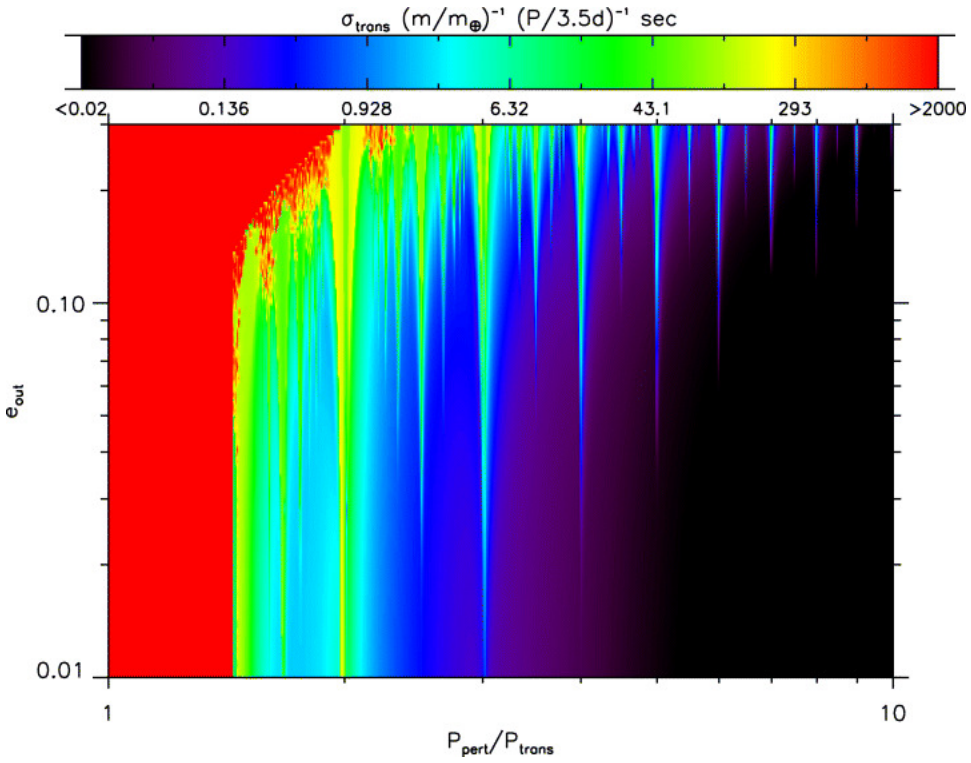

Figure 1.7: Magnitude of transit timing variations of HD 290458b that would be caused by an Earth-mass exterior perturber with a variety of periods and eccentricities (Fig. 5 from Agol et al. 2005). Note the spikes of large TTV amplitudes at mean-motion resonances, poetically termed "flames of resonance" by e.g. Payne et al. (2010).

or near a mean-motion resonance. Lest I sound too optimistic a note, however, Latham et al. (2011), also using the *Kepler* data set, find that systems harboring a hot jupiter are less likely to harbor additional planets than those hosting a hot neptune or hot super-earth, decreasing the probability that any given hot jupiter will exist in a system with a second, perturbing planet.

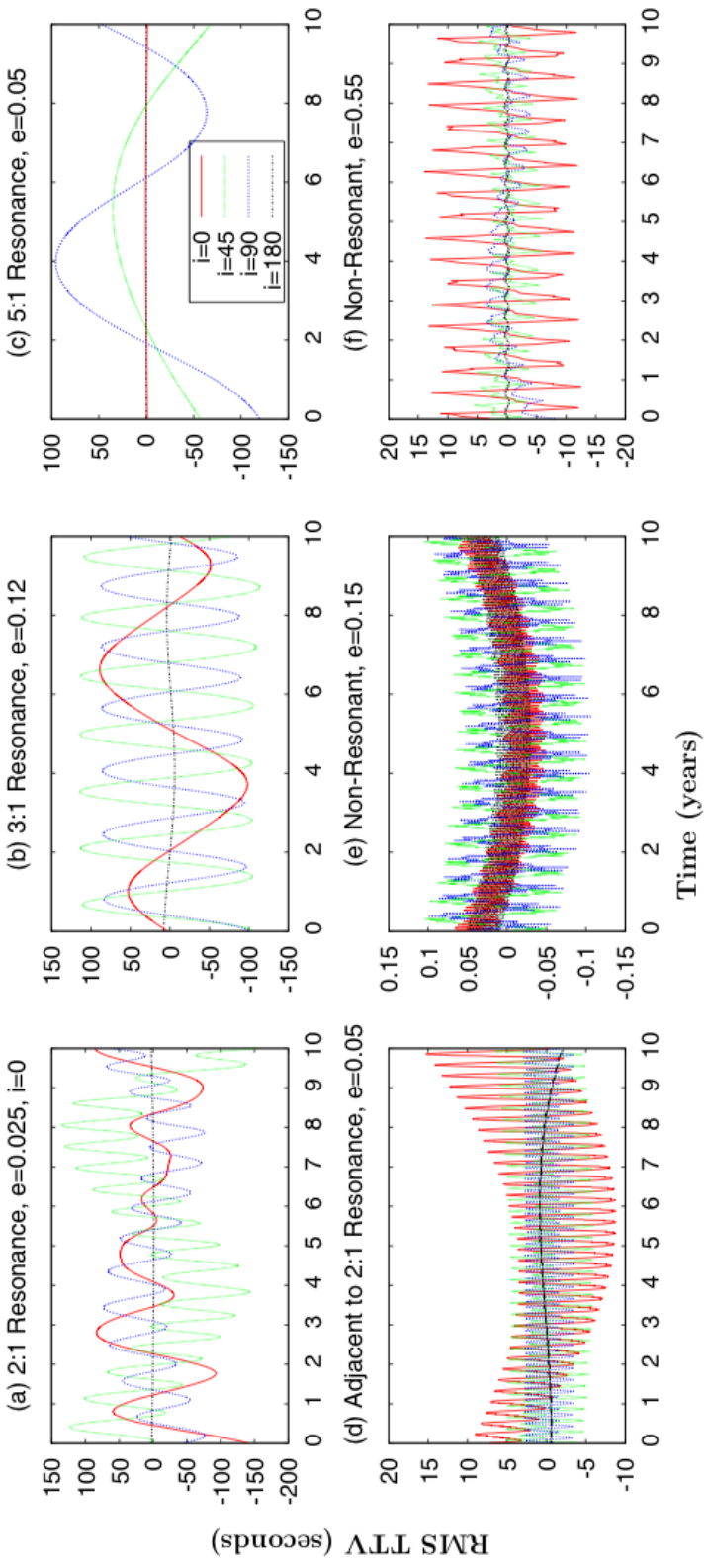

Figure 1.8: Comparison of TTV patterns caused by perturbers with a variety of orbital characteristics, Fig. 1 from Payne et al. (2010). The transiting planet is a hot jupiter and the perturbing body a non-transiting Earth-mass planet. Each panel is labeled with the orbital location relative to the transiting body and eccentricity of the perturbing body. The different colors show the signals caused by different mutual inclinations between the orbital planes of the transiting and perturbing bodies, as shown in the legend in panel c. Note the varying TTV amplitudes (from ~100 seconds down to ~ 1 second) and periods (from weeks to years).

The past year has seen an explosion of TTV observations, with ground-based detections of periodic or plausibly periodic TTVs found for WASP-3b (Maciejewski et al. 2010a), WASP-10b (Maciejewski et al. 2010b), and HAT-P-13b (Pál et al. 2011). Meanwhile, TTVs observed in the data from the *Kepler* spacecraft have been used to determine the masses and confirm the planetary nature of two of the three planets around Kepler-9 (Holman et al. 2010) and five of the six transiting planet candidates in the remarkable Kepler-11 system (Lissauer et al. 2011a). The TTVs for WASP-3b are shown in Figs. 1.9 and 1.10. Fig. 1.9 is an example of an $O - C$ (observed minus calculated) diagram; it simply shows the difference between the observed and calculated transit times as a function of time. A linear trend would result from an incorrect period for the planet, while a periodic or quasi-periodic trend, such as those shown in Figs. 1.8 and 1.10, could be caused by another planet.

Additional planets, however, are not the only possible cause of measurable effects on the transit. For instance, if a moon is present around an exoplanet it can induce both TTVs and transit duration variations (TDVs) (Simon et al. 2007; Kipping 2009). Trojan planets could also cause TTVs (Ford & Holman 2007). Such effects, however, have yet to be detected. Precession of a planet's orbital plane can also generate TDVs. While for most systems this effect would be far too small to measure, Iorio (2010) has proposed that both classical and relativistic precession could be measurable over timespans of $\sim$10 years for WASP-33b, a planet transiting a massive, fast-rotating star on a highly inclined orbit. Finally, Watson & Marsh (2010) propose that long-term TTVs could probe the dynamo structure of active stars via the Applegate effect. This effect is caused by changes in the angular momentum distribution within a star as a result of magnetic torques during a cycle of magnetic activity. This changes the quadrupole moment of the

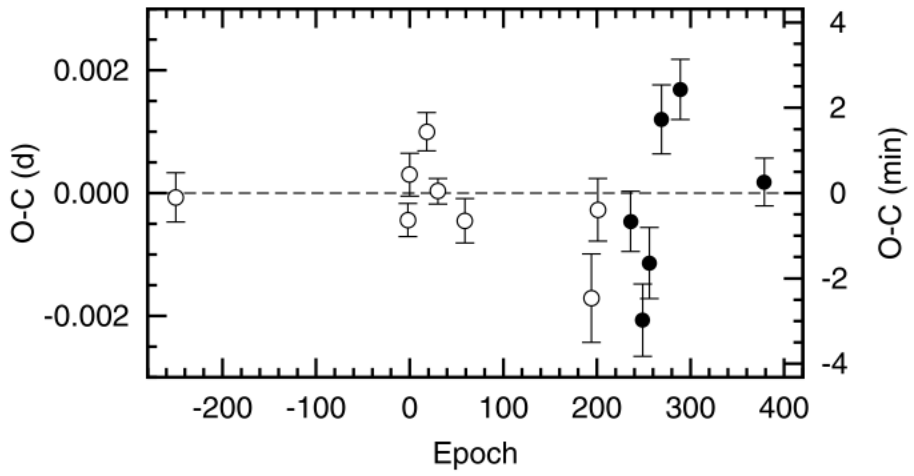

Figure 1.9: $O - C$ diagram for WASP-3b (Fig. 2 from Maciejewski et al. 2010a), showing a non-linear variation in the transit times.

star's gravitational field, thus altering the orbit of any companion (Applegate 1992).

1.2.2 Transmission Spectroscopy and Multiband Photometry

A potentially very powerful technique that is enabled by the transit geometry is transmission spectroscopy. It is one of only a few techniques that has the potential to detect biomarkers in the atmospheres of any earth-like planets discovered in the future.

In transmission spectroscopy observations, the spectrum of a transiting system is taken during transit and again when the planet is out of transit. The two spectra are then subtracted, removing the stellar contribution to the spectrum but leaving the signature of the light absorbed by the planet's atmosphere. In practice it is necessary to obtain many observations in order to attain a sufficiently high signal-to-noise ratio (SNR).

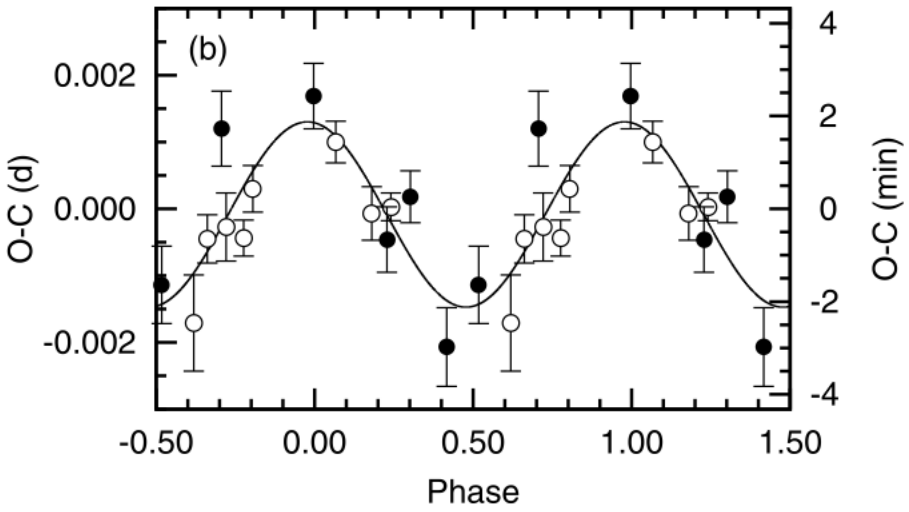

Figure 1.10: The transit timing variations for WASP-3b from Fig. 1.9 phased with an ∼128 day period (Fig. 3b from Maciejewski et al. 2010a).

Thus far this technique has been limited to relatively bright exoplanet host stars. Atoms and molecules that have been detected using this technique include Na I, H_2O, and CH_4 (Redfield et al. 2008; Beaulieu et al. 2010; Swain et al. 2008), as well as H_2 in an exosphere around HD 209458b (Vidal-Madjar et al. 2003). These observations, however, require either space-based instruments, such as the *Hubble Space Telescope* (*HST*), or very large ground-based telescopes, such as the 9.2-m Hobby-Eberly Telescope (HET). Future instruments such as the *James Webb Space Telescope* (*JWST*) may be able to extend this technique to terrestrial planets found by the *Kepler* mission.

While transmission spectroscopy can give detailed spectral information on an exoplanetary atmosphere over a wide wavelength range, it requires a large amount of data from large telescopes, and is furthermore restricted to the very brightest transiting planet host stars, such as HD 189733 (V = 7.7; Redfield et al. 2008) and HD 209458 (V = 7.65; Schneider 2011; Beaulieu et al. 2010).

A complimentary technique which has also been used is multiband transit

photometry. This technique involves either simultaneous transit observations or observations of multiple transits through different filters. The transit depth in each filter is compared; a deeper transit in a given filter indicates a larger effective radius for the planet in that band, resulting from greater atmospheric absorption. While this technique can be applied to fainter host stars than transmission spectroscopy can, it only probes the spectrum at a handful of discrete points, which then must be compared to atmospheric models to derive information about the planetary atmosphere.

This technique has been used primarily in the infrared, where broad molecular bands exist which can be detected using this technique (e.g., Bean et al. 2010). Recently, however, two teams have used tunable filters on the 10.4-m Gran Telescopio Canarias to probe narrow wave bands immediately around the optical K I line, resulting in detections of this atom in the atmospheres of two exoplanets around fainter host stars, HD 80606b (V = 8.93; Colon et al. 2010; Schneider 2011) and XO-2b (V = 11.18; Sing et al. 2011; Schneider 2011).

1.2.3 Lightcurve Phase Variations and Secondary Eclipses

Detailed observations of the lightcurve when a planet is out of transit can reveal the signature of reflected light from the planet. Essentially, the flux from the system varies with the phase of the planet. Near secondary eclipse the planet is in a "full" phase, reflecting a large amount of light, and so the flux is higher than when the planet is near the transit, in a "new" phase, reflecting essentially no light towards Earth. As this technique only needs the planet's phase to vary, it does not require the planet to transit, and so can be applied to non-transiting planets, such as υ Andromedae b (Crossfield et al. 2010), although the inclination

must still be close to 90°.

A similar technique has also been used in the infrared in order to map the temperature distribution on exoplanets. This has revealed that some tidally locked hot jupiters experience extremely high-velocity winds, as the point of highest atmospheric temperature is displaced by some amount from the sub-stellar point (e.g., Knutson et al. 2009). Similarly, observations of the secondary eclipse in the infrared allow the determination of the planet's infrared flux and thus its temperature (e.g., Smith et al. 2011).

1.3 Exoplanets at Wesleyan

Although such techniques as transmission spectroscopy and lightcurve phase variations require large-aperture telescopes, more modest facilities such as those operated by Wesleyan can and have made an impact on the field through the observations of transits. The first known transiting planet, HD 209458b, was discovered via radial velocity and shown to transit using a very small (9.9 cm) telescope (Charbonneau et al. 2000). Many of the current wide-angle transiting planet surveys, such as HATNet and SuperWASP (Bakos et al. 2004; Pollacco et al. 2006) utilize small telescopes (11 cm for both surveys). Small telescopes can also search for transit timing variations, and indeed the observations suggesting the existence of WASP-3c were obtained on small telescopes (60 and 90 cm; Maciejewski et al. 2010a). Even beyond such high-profile finds, small telescopes can make real contributions by refining the ephemerides of transiting systems (see e.g., Dittmann et al. 2010). An additional advantage of small telescopes is the large field of view that they afford, providing a large number of comparison stars. In contrast, large telescopes with small fields of view are limited to targets with

appropriate comparison stars nearby. Finally, it is desirable to have a charge-coupled device (CCD) camera with as short a readout time as possible in order to obtain a high photometric cadence.

Wesleyan University is well-suited to take part in such observations. The 24-inch Perkin Telescope at Van Vleck Observatory (with a CCD readout time of ~ 12 seconds) has been used for many years to observe the variability of T Tauri stars (e.g., Herbst et al. 2010), and the same facilities can be extended to the observations of transits. To this end the Wesleyan Transiting Exoplanet Program (WesTEP) has been initiated to conduct transit observations with an emphasis on searching for transit timing variations. Much of the pipeline was constructed and a few observations conducted by Leiner (2010). In this work I describe another year's worth of progress on the project, including observations of nearly two dozen exoplanetary transits.

Chapter 2

Observations

Observations for this work were conducted using the 24-in Perkin Telescope at Wesleyan University's Van Vleck Observatory (hereafter VVO). The telescope is equiped with an electromechanically-cooled 2048 $\times$ 2048 Apogee Instruments CCD (charge-coupled device) camera. Readout time for the whole chip is $\sim$12 seconds, providing a high photometric cadence. The observational equipment is described in Konon (2008).

Transit observations were conducted in the Cousins I band, as this is the reddest band available on the Perkin Telescope and limb darkening is less severe at longer wavelengths (see Fig. 3 of Knutson et al. 2007). Exposures ranged from 5 to 120 seconds, depending on the magnitude of the target star. In addition to the science exposures, twilight sky flats were taken where possible, and dark exposures and bias frames were collected every night.

In order to maximize the quality of the data we conducted a number of tests to optimize our observing strategies and improve the mechanical workings of the telescope. These tests included experimentation with manual guiding and degree of defocusing.

2.1 Test Observations

The 24-in telescope is not equipped with an autoguider and the telescope tends to drift during observations , so manual recentering had to be employed. It is desirable to keep the PSF of the target star centered (or to otherwise minimize pixel drift) for two reasons. First, if the PSF occupies a small set of pixels for the entire observation, random pixel-to-pixel variations will remain approximately the same through the entire data set and so will have a minimal effect on the data. Second, the aperture photometry process (see §3.1) is expedited if the routine has to search a smaller number of pixels for the PSF centroid.

In order to manually recenter the telescope a ± 10 pixel box is defined around the center of the chip, i.e., [1014:1014]–[1034:1034]. After each set of exposures the centroid of the target PSF is checked and if it strays outside of this box the telescope is manually recentered until the centroid has returned to the box. This results in the centroid being confined to a 20 × 20 pixel box, thereby reducing the impact of pixel-to-pixel errors and expediting the aperture photometry process. Fig. 2.1 shows the degree of drift caused by no use of recentering, and Fig. 2.2 the improvement made by implementing recentering. The cumulative effect of this is shown in Fig. 2.3, where the number of exposures for which the target centroid has been on a given pixel during observations of seventeen transits is displayed. The effects of pixel drift are discussed in more detail in §3.2.1.

2.1.1 Defocusing

Defocusing the telescope to some degree has previously been used to obtain higher precision in exoplanet transit observations (see e.g., Dittmann et al. 2010;

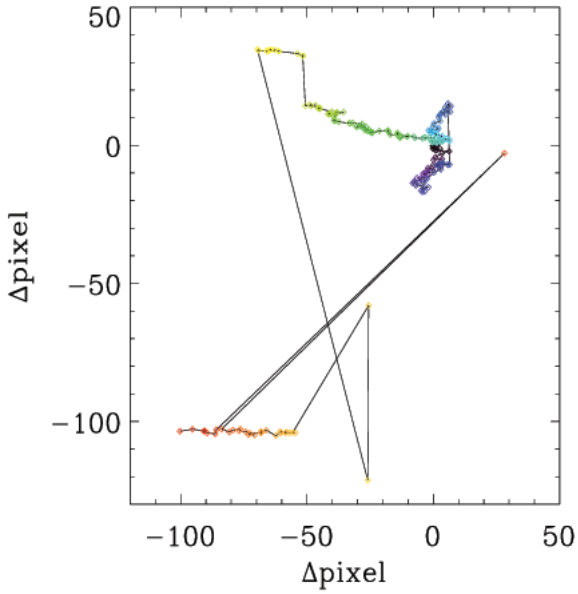

Figure 2.1: Drift in the PSF centroid when recentering is not used, from the XO-5b transit of 2009 February 24. The progression of colors of the points indicates their time order, with the earliest points in purple and the latest points in red. Fig. 4.1 from Leiner (2010). Note the much larger scale of pixel drift with respect to Fig. 2.2.

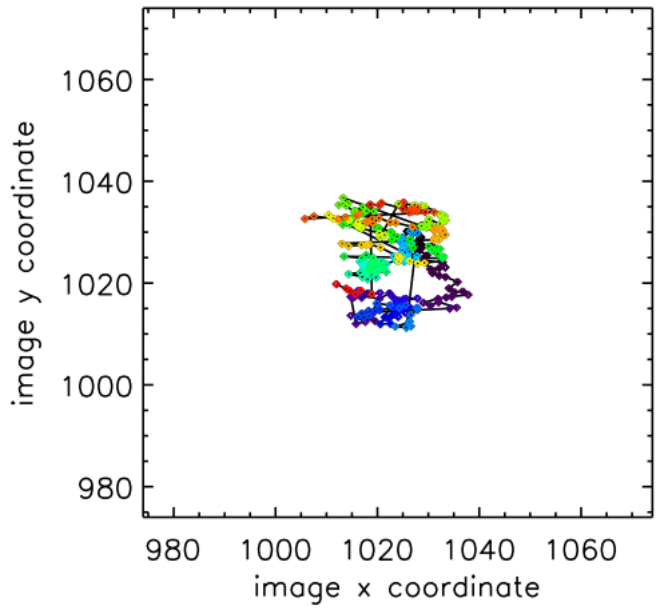

Figure 2.2: Drift in the PSF centroid when recentering is used, from the WASP-3b transit of 2010 August 27-28. The progression of colors of the points indicates their time order, with the earliest points in purple and the latest points in red.

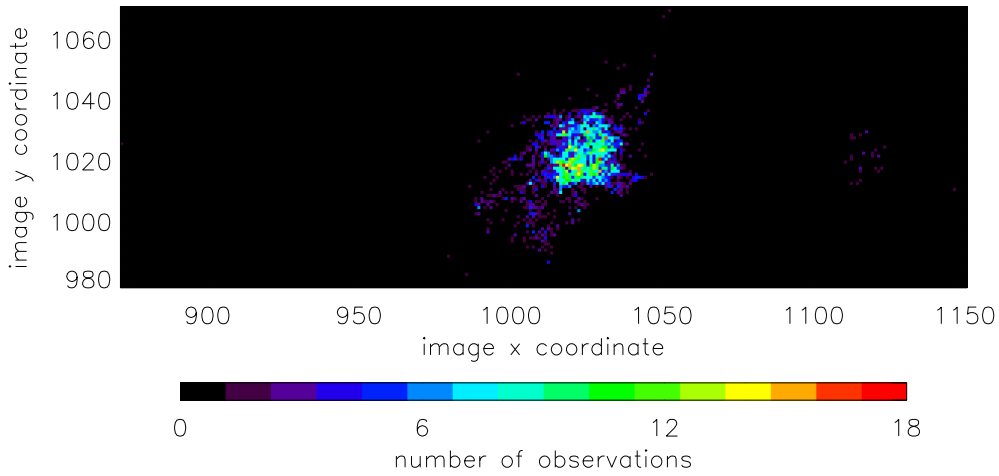

Figure 2.3: Number of data points over seventeen transits for which the target centroid was on a given pixel. The 20×20 pixel region around the center of the chip is clearly visible.

Southworth et al. 2009). In order to determine what degree of defocusing would result in the highest SNR in the final lightcurve, we conducted three sets of observations of non-varying stars.

Each test observed a transiting exoplanet host star that has not been found to vary while no transit was occurring. HAT-P-2 was used for the first test, on 2010 July 15, HAT-P-11 for the second, on 2010 July 25, and HD 209458 for the third, on 2010 August 28. The observing method was as follows. The telescope was focused and a set of 10 exposures (15 for HD 209458) taken. The telescope was then defocused by some amount, 10 (15) more exposures taken, and the process repeated. The exposure times were constant even as the defocusing occurred.

The data were then flat field, bias, and dark corrected in IRAF, and aperture photometry was performed in IDL, as described in §3.1. A range of aperture radii was used, from 10 to 50 pixels. As the full-width half-maximum (FWHM) of the PSF varied throughout the data set, any apertures which excluded more than 0.1% of the flux were discarded.

The results from the tests are shown in Figs. 2.4, 2.5, and 2.6 respectively; these figures show the standard deviations of the residuals for each set of 10 (15) images as a function of the average PSF width in that set. The observations for the first test were interrupted by clouds part way through, corresponding to the discontinuity in the points at a PSF width of $\sim$4.5 pixels (Fig. 2.4). This illustrates that the quality of the data (i.e., the scatter of photometric data points) can be highly dependent upon observing conditions. Two data sets for the first test had to be discarded due to the clouds. Some care also had to be taken with the first data set because two of the comparison stars were significantly brighter than the target star and were saturated in the low-PSF images.

The results of these tests are somewhat inconclusive. Though interpretation

of the first test (Fig. 2.4) is complicated by the presence of the discontinuity, it appears that the points to the left of the discontinuity follow a trend of slightly decreasing scatter in the residuals with increasing PSF width. The second test (Fig. 2.5 is even more inconclusive, with no trend apparent. For the third test (Fig. 2.6) there appears to be an overall trend of *increasing* standard deviation of the residuals with increasing PSF width, though with significant scatter. Also note that the standard deviations of the residuals for the third test are larger than those for the other tests, and also have a wider scatter, possibly indicating poor-quality data.

Given that the above tests were inconclusive, we have elected to observe with a mildly defocused PSF, with a PSF FWHM of ∼7-8 pixels (roughly equivalent to a PSF width of 4 pixels). The focused FWHM for the 24" and CCD is ∼5-6 pixels, depending upon the observing conditions, and can range as high as 8 pixels in poor conditions. However, it would be beneficial to perform more tests in the future to better quantify the effect of defocusing. For instance, instead of holding the exposure length constant it could be adjusted so that the peak flux in all images is approximately the same, as the decreasing SNR in the current observations as the aperture increases (the same amount of flux is spread over more pixels) likely masks some of the true signal.

2.1.2 Tracking Improvement and Polar Alignment

The addition of an autoguider to the Perkin Telescope would be useful for transit observations, as it would allow the PSF to be kept on precisely the same set of pixels through the entire observation, and would additionally reduce the downtime between sets of observations due to manual recentering, improving our

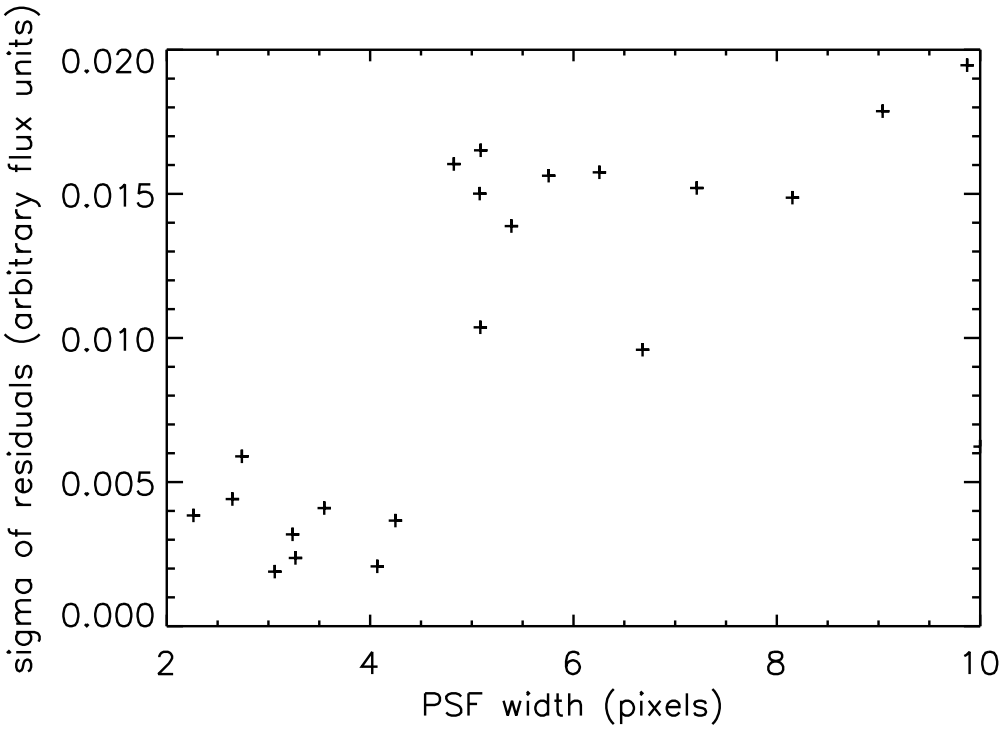

Figure 2.4: Standard deviation of the residuals as a function of PSF width for the first defocusing test, 2010 July 15; the observed star was HAT-P-2.

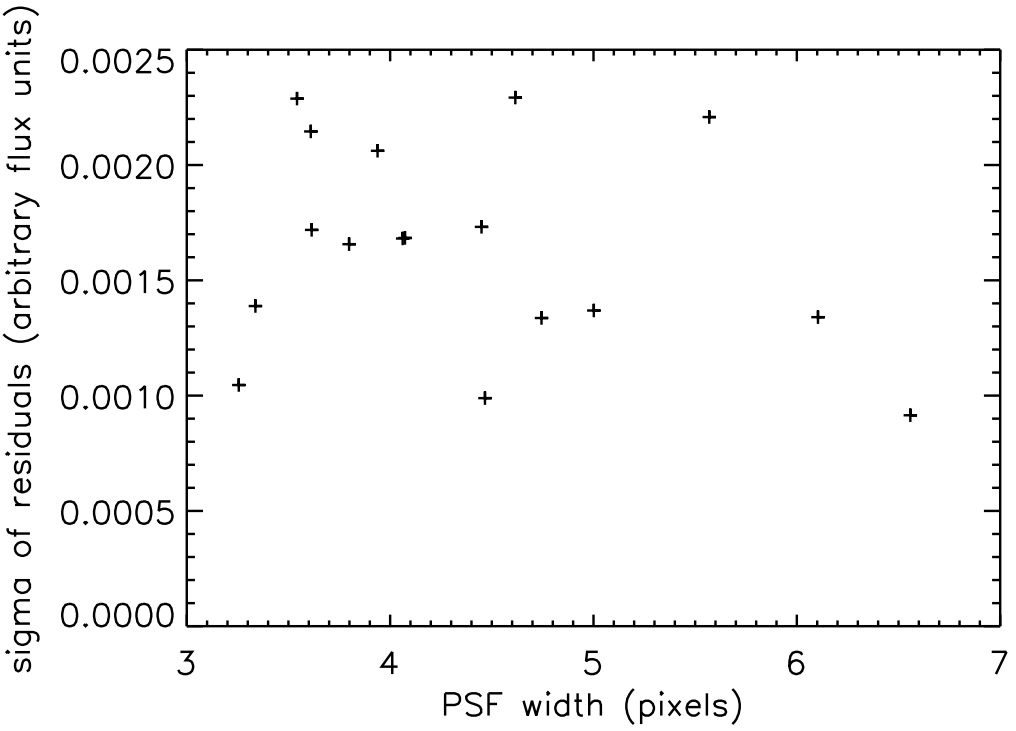

Figure 2.5: Standard deviation of the residuals as a function of PSF width for the second defocusing test, 2010 July 25; the observed star was HAT-P-11.

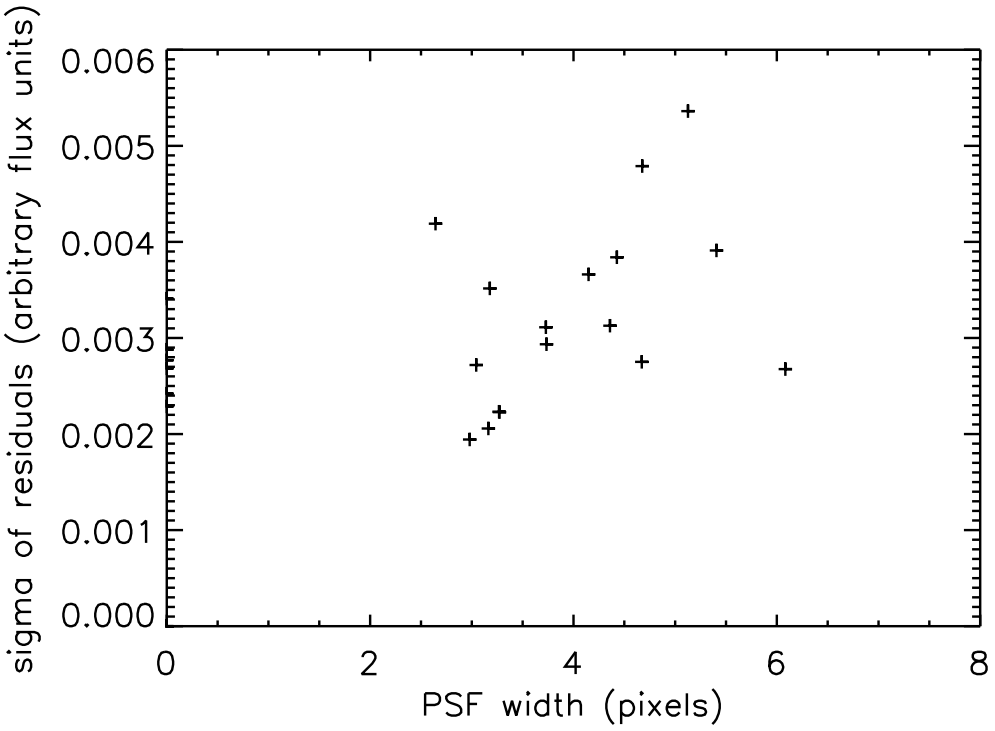

Figure 2.6: Standard deviation of the residuals as a function of PSF width for the third defocusing test, 2010 August 28; the observed star was HD 209458.

time resolution and duty cycle slightly.

Improvements could also be made by reducing the magnitude of drift that the telescope experiences. There could be three major sources for the drift: the clock drive running at an incorrect speed, a misalignment in the polar axis of the telescope, or physical flexure of the telescope optics as the telescope points to different parts of the sky. At present there is nothing that we can do about flexure, but tracking and polar alignment errors can in principle be eliminated through simple electronic and mechanical adjustments.

In order to make any necessary adjustments it was first necessary to quantify the magnitude of drift, including as a function of position on the sky, to give some indication as to whether the drift was caused by tracking or polar alignment errors, or a combination thereof. Two varieties of tests were conducted.

For a set of six short drift observations, a bright star was chosen and observed with one-second exposures. Only a 200 $\times$ 200 region of the CCD around the star was read out in order to maximize the cadence of the observations. Thirty exposures were taken in each set. Targets were observed at a variety of declinations and hour angles, as enumerated in Table 2.1.

Three longer drift observations were also taken at a variety of declinations and hour angles. For these tests the exposure length was 120 seconds, and the entire chip was read out. Thirty exposures were taken for each set, except for the first, which was cut short by clouds after 27 exposures. These observations are enumerated in Table 2.2.

From these tests we determined that a large component of the drift is likely due to misalignment of the polar axis of the telescope, with a smaller component from an incorrect clock drive rate. In order to quantify the drift due to polar axis misalignment, we made a further two sets of long drift observations, both on the

Table 2.1. Observations of stars used for the short drift tests

Target	Date	Time[a]	Dec (J2000.0)	HA
16 Cyg	July 16	00:29	+50 31 30	−1 32
σ Ser	July 17	22:11	+01 01 45	0 41
19 UMi	July 17	22:52	+75 52 39	1 34
43 Cyg	July 28	22:22	+49 23 00	−3 31
τ Aql	July 28	22:37	+07 16 41	−2 09
19 CVn	July 30	21:47	+40 51 19	−1 32

[a]Times are in local time (EDT/GMT-4).

Table 2.2. Observations of fields used for the long drift test

Target	Date	Time (center)[a]	Dec (J2000.0)	HA (center)
1	July 28	∼22:20	+40 00 00	0 00
2	July 31	22:25	+00 00 00	0 42
3	July 31	23:43	+70 00 00	−2 00

[a]Times are in local time (EDT/GMT-4).

celestial equator, and measured the drift of the field in declination only. Ideally, one observation would be taken as some equatorial star field transits the meridian, and the other as another star field rises or sets. In these orthogonal directions the effect of the two orthogonal components of the misalignment are decoupled; at the meridian only the azimuthal error in the polar axis alignment contributes to the drift in declination, while at the horizon the declination drift is caused only by the altitude error (J. Filhaber, personal communication 2010).

The practical complication is that it is generally not possible to observe at the horizon. At VVO the farthest east that can be observed on the equator is at an hour angle of approximately -4^h35^m before a tree blocks the line of sight, while the western extent of the equator is even more constrained. Therefore, the "horizon" observation was taken between hour angles of $\sim -4^h30^m$ and $\sim -3^h30^m$.

The results of these drift tests are shown in Figs. 2.7 and 2.8. For the meridian observation a linear fit was taken to the data in order to calculate the drift. For the eastern observation the trend was distinctly non-linear as more and more of the azimuthal error in polar alignment contributed to the declination drift over the course of the observation. Therefore, a linear fit was taken to the first ~ 20 minutes of observations, when the drift rate was approximately linear and had the least contribution from the azimuthal error, and this fit was extrapolated over the hour in order to compute the total drift rate. The altitude and azimuth errors were then calculated using spherical trigonometry. The derived errors were -49" in azimuth and -5' 11" in altitude.

The polar axis of the telescope was realigned on the night of 2010 September 17-18 under the direction of J. Filhaber. The alignment was not completed as an urgent mechanical issue with the telescope was discovered, and the polar axis was moved only in altitude. While the drift is still present, a drift test at $\sim -4^h35^m$

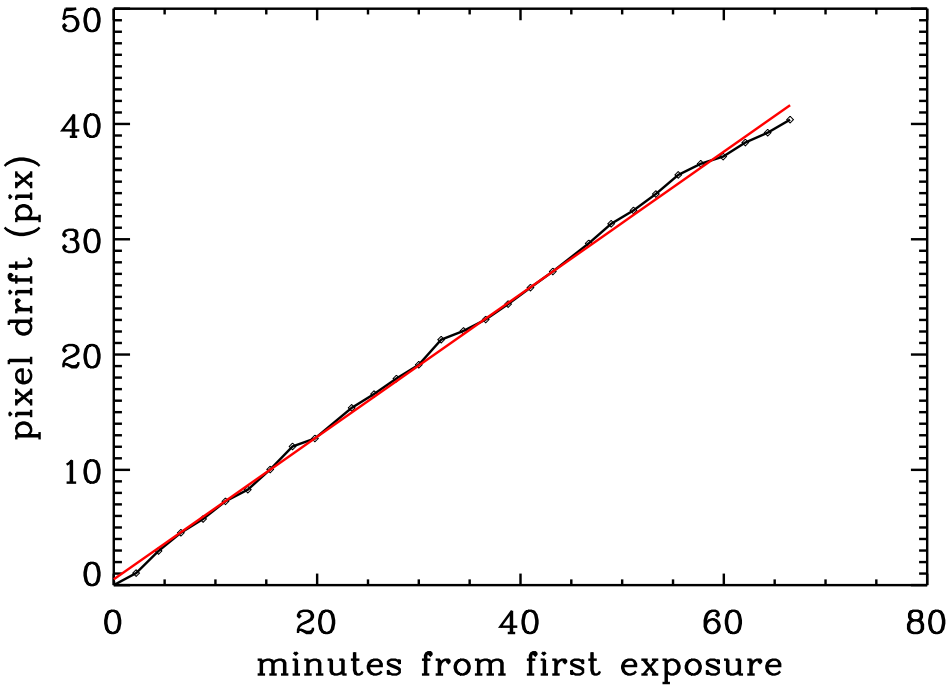

Figure 2.7: Drift in declination of an equatorial star field observed crossing the meridian prior to the realignment, showing a linear fit to the drift. The drift amounted to 37.6 pixels per hour, or 12.8" per hour.

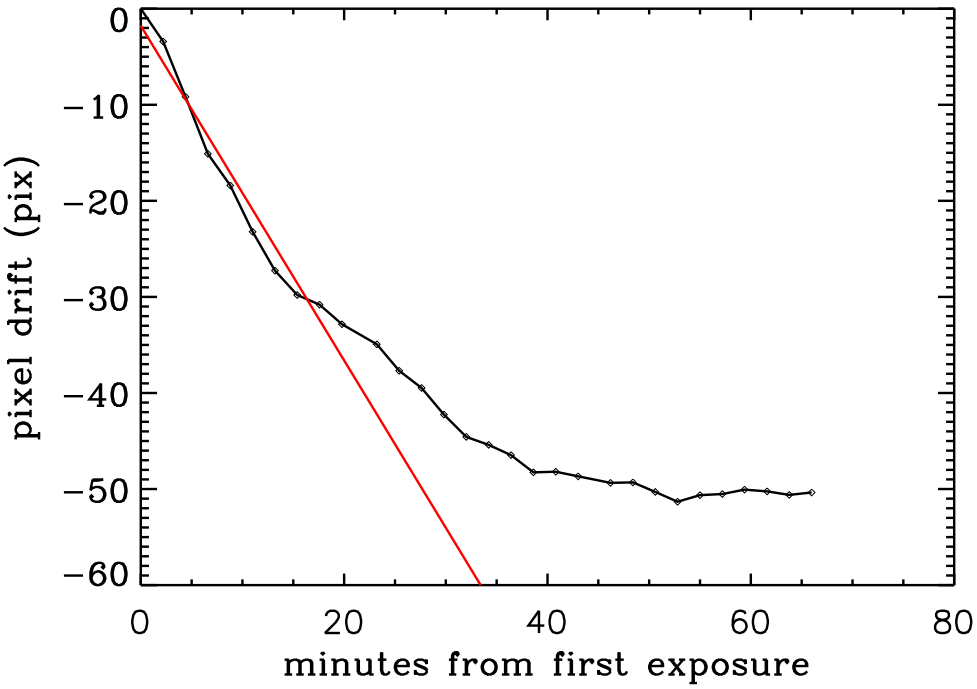

Figure 2.8: Drift in declination of an equatorial star field observed near an hour angle of $\sim$ 5h prior to the realignment, showing a linear fit to the first 20 minutes of drift. The drift amounted to -106 pixels per hour, or -36.1" per hour.

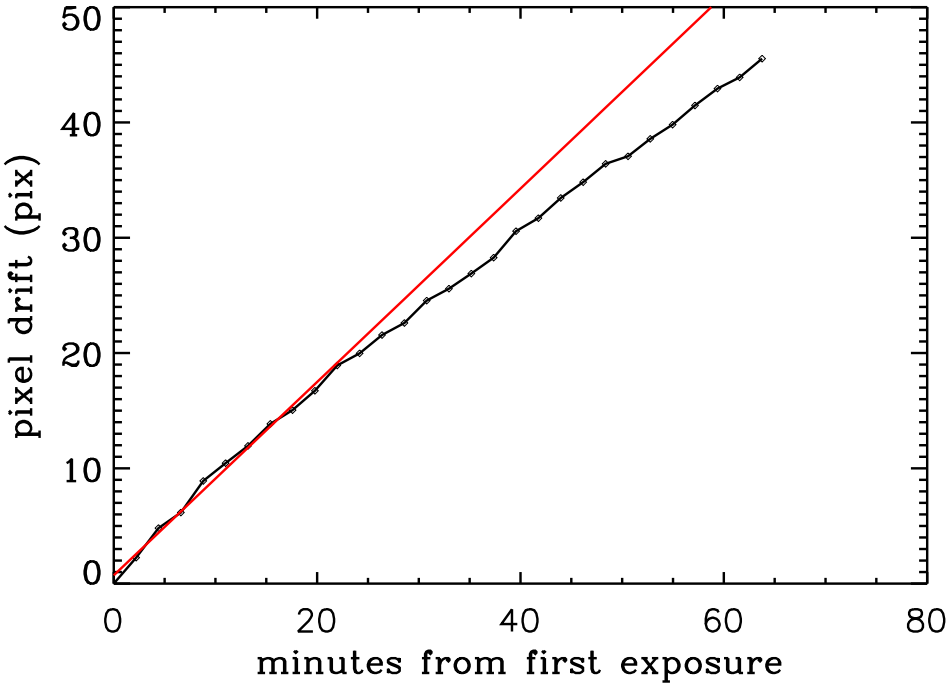

Figure 2.9: Drift in declination of an equatorial star field observed near an hour angle of $\sim$ 5h after the polar realignment, showing a linear fit to the first 20 minutes of drift. The drift amounts to 51.0 pixels per hour, or 17.3" per hour.

after the alignment (see Fig. 2.9) shows that the magnitude of the drift has been cut in half, and moreover has changed in sign. Thus, while the drift due to polar axis misalignment has not been eliminated, it has been mitigated to some extent. Current and future work on an autoguider for the 24" (J. Schaeffer, personal communication 2011) will likely obviate the need for precise polar alignment.

2.1.3 Local Horizon

On the night of August 28, as there were no favorable transits, I determined the local horizon as viewed from the 24". The telescope was slewed east and west until an obstacle blocked the view of the sky, and the hour angle was recorded.

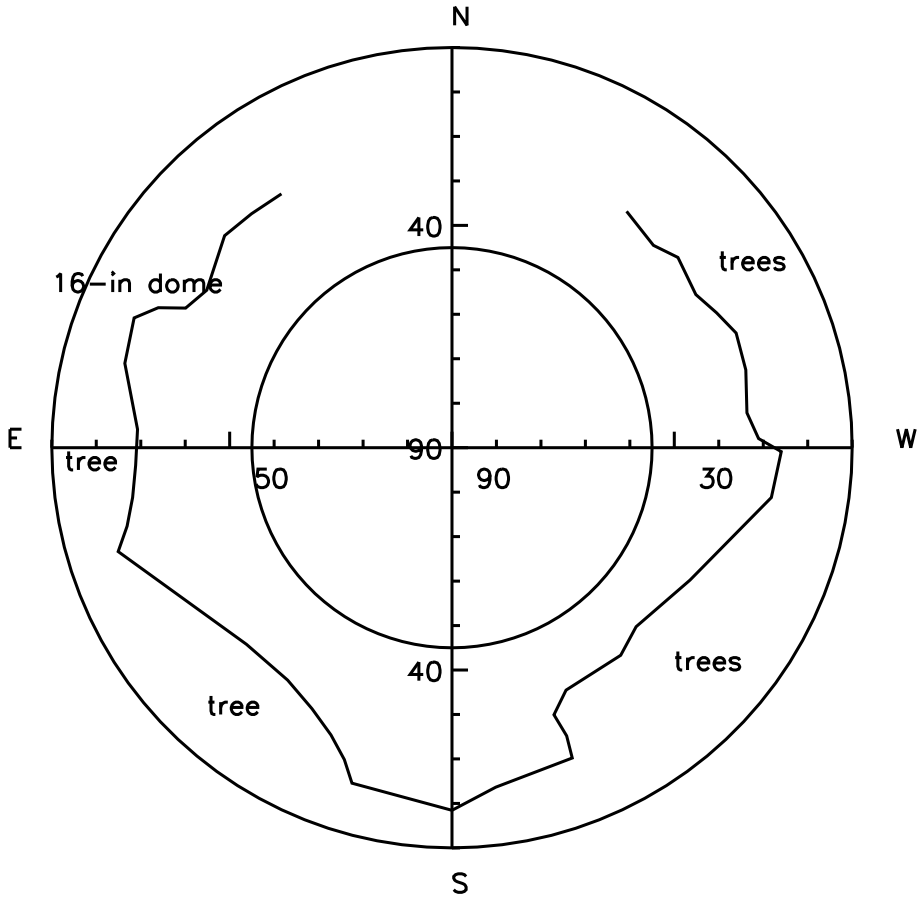

Figure 2.10: Local horizon as viewed from the 24", with declinations between +55° and −35°. The outer circle is the horizon and the inner deliniates an altitude of 45°. Axes are altitude and the units are degrees.

Measurements were taken in decriments of 5° over the range $-35° \leq \delta \leq +55°$. Hour angle coverage at $\delta > +55°$ was great enough that it was not measured, and the telescope's horizon limit and latitude prevent it from achieving $\delta < -35°$. The local horizon as determined by these tests is plotted in Fig. 2.10.

The local horizon was also incorporated into our IDL routine that calculates what transits will be visible from VVO. Previously the routine had used a simple airmass limit to determine whether the target was in the sky, which resulted in attempted observations of some transits that were foiled when it was discovered

that the target was behind some local obstruction, e.g., the dome of the VVO 16-in Fiducia Telescope. The routine now selects only transits where the target is above the local horizon for the entire duration of the transit, and the duration of the transit occurs entirely between sunset and sunrise. However, as the routine only excludes transits that begin or end during daylight, some transits are still selected which start too close to sunset or end too close to sunrise to be observed. Thus it would likely be better in the future to modify the cutoff to exclude transits which start $\lesssim$30-90 minutes after sunset or end the same amount before sunrise.

2.2 Transit Observations

2.2.1 WASP-33b and HAT-P-16b

Two systems with known transiting exoplanets were selected as primary targets: WASP-33 (Collier Cameron et al. 2010) and HAT-P-16 (Buchhave et al. 2010). These planets were selected for several reasons. First, they were newly discovered at the time this work began, and so our observations could add significantly to the knowledge base on these worlds. Second, both orbit bright stars (V = 8.3 and 10.8, respectively). Third, both stars had many transits visible from VVO during the summer and fall of 2010. Finally, both are intriguing for other reasons.

HAT-P-16b is one of a small number of hot jupiters with an eccentric orbit, which could plausibly be caused by resonant interactions with a second planet in the system counteracting the effects of tidal circularization. Other possible explanations exist, however, such as a longer tidal circularization timescale than previously considered (Buchhave et al. 2010).

WASP-33b is one of the few known planets orbiting an early-type star, an area

of parameter space that is poorly sampled because of the difficulty in confirming discoveries using the radial velocity technique due to the relatively featureless spectra of hot stars (Collier Cameron et al. 2010). It is currently the hottest known planet (Smith et al. 2011), and orbits a δ Scuti variable (Herrero et al. 2011). Additionally, Iorio (2010) has proposed that, due to WASP-33b's status as a planet on a highly-inclined orbit close to a massive, fast-rotating star, its orbit should undergo pronounced precession due to both classical and relativistic factors. Athough Iorio (2010) calculates that the resulting transit duration variations would be very small (on the order of 1 part in 3×10^{-6}), such an effect could become measureable over a period of 10 years or less. Although such a lengthy campaign is beyond the scope of this work, WASP-33b could be a promising target for long-term observations at VVO.

The properties of each star are given in the first part of Table 2.3 and the orbiting planets in Table 2.4. Observations of HAT-P-16 are detailed in Table 2.5, and those of WASP-33 in Table 2.6. To date, one complete and one partial HAT-P-16 transit and six complete WASP-33 transits have been observed; observations of four other transits of WASP-33b were foiled due to various issues, as noted in Table 2.6.

Table 2.3. Properties of observed stars

ID	RA (J2000.0)	Dec (J2000.0)	Spec. type	V mag	D (pc)	T_{eff} (K)	N_{obs}
HAT-P-16	00 38 18	+42 27 47	F8	10.8	235 ± 10	6158 ± 80	2
WASP-3	18 34 32	+35 39 42	F7V	10.64	223	6400 ± 100	2
WASP-33	02 26 51	+37 33 02	A5	8.3	116 ± 16	7400 ± 200	6
CoRoT-Exo-1	06 48 19	-03 06 08	G0V	13.6	$> 460 \pm 100$	5950 ± 150	1
CoRoT-Exo-2	19 27 07	+01 23 02	G7V	12.57	300 ± 100	5625 ± 120	1
HAT-P-5	18 17 37	+36 37 18	···	12	340 ± 30	5960 ± 100	0
HAT-P-11	19 50 50	+48 04 51	K4	9.59	38 ± 1.3	4780 ± 50	1
HAT-P-12	13 57 34	+43 29 37	···	12.84	$142.5^{+4.2}_{-3.3}$	4650 ± 60	1
HAT-P-13	08 39 32	+47 21 07	G4	10.62	214 ± 12	5638 ± 90	0
HAT-P-14	17 20 28	+38 14 32	F	9.98	205 ± 11	6600 ± 90	2
HAT-P-23	20 24 30	+16 45 44	G0V	12.43	···	6000 ± 125	1
HD 189733	20 00 43	+22 42 39	K1-K2	7.67	19.3 ± 0.2	4890 ± 200	1
Kepler-5	19 57 38	+44 02 06	···	13.9	···	6297 ± 60	1
TrES-1	19 04 09	+36 37 57	K0V	11.79	157 ± 6	···	0
TrES-3	17 52 07	+37 32 46	G	12.4	···	5720 ± 150	0
WASP-2	20 30 54	+06 25 46	K1V	11.98	144	5200 ± 200	2
WASP-12	06 30 33	+29 40 20	G0	11.69	146 ± 11	6300 ± 150	1
WASP-32	00 15 51	+01 12 02	G	11.3	···	6100	1

Note. — The stars above the horizontal line are the primary targets of this work; those below the line are those for which other transits have been observed, with each class in alphabetical order. N_{obs} is the number of transits (full and partial) of each system that have been successfully observed; some stars have $N_{obs} = 0$ due to transits that were interrupted by clouds or were of poor data quality. All data are from Schneider (2011)

Table 2.4. Properties of observed planets

Name	$M(M_J)$	$R(R_J)$	a (AU)	P (days)	e	$i(^\circ)$
HAT-P-16b	4.193 ± 0.094	1.289 ± 0.066	0.0413 ± 0.0004	$2.77596 \pm 3 \times 10^{-6}$	0.036 ± 0.004	86.6 ± 0.7
WASP-3b	2.06 ± 0.13	1.454 ± 0.084	0.0313 ± 0.0001	$1.846837 \pm 1 \times 10^{-6}$	0	$85.06^{+0.15}_{-0.16}$
WASP-33b	< 4.59[a]	$1.438^{+0.062}_{-0.03}$	0.02558 ± 0.00023	$1.21986967 \pm 4.5 \times 10^{-7}$	0	$87.67^{+1.6}_{-2.4}$
CoRoT-Exo-1b	1.03 ± 0.12	1.49 ± 0.08	0.0254 ± 0.0004	$1.5089557 \pm 6.4 \times 10^{-6}$	0	85.1 ± 0.5
CoRoT-Exo-2b	3.31 ± 0.16	1.465 ± 0.029	0.0281 ± 0.0009	$1.7429964 \pm 1.7 \times 10^{-6}$	0	87.84 ± 0.1
HAT-P-5b	1.06 ± 0.11	1.26 ± 0.05	0.04075 ± 2.788491	$2.788491 \pm 2.5 \times 10^{-5}$	0	86.75 ± 0.44
HAT-P-11b	0.081 ± 0.009	0.452 ± 0.02	$0.053^{+0.0002}_{-0.0008}$	$4.887804 \pm 4 \times 10^{-6}$	0.198 ± 0.046	88.5 ± 0.6
HAT-P-12b	0.211 ± 0.012	$0.959^{+0.029}_{-0.021}$	0.0384 ± 0.0003	$3.2130598 \pm 2.1 \times 10^{-6}$	0	89.0 ± 0.4
HAT-P-13b	0.85 ± 0.038	1.28 ± 0.079	$0.0426^{+0.0006}_{-0.0012}$	$2.916293 \pm 1 \times 10^{-5}$	$0.0142^{+0.0052}_{-0.0044}$	83.3 ± 0.62
HAT-P-14b	2.2 ± 0.04	1.2 ± 0.04	0.0594 ± 0.0004	$4.627657 \pm 5 \times 10^{-6}$	0.095 ± 0.011	83.2 ± 0.2
HAT-P-23b	2.09 ± 0.11	1.368 ± 0.09	0.0232 ± 0.0002	$1.212884 \pm 2 \times 10^{-5}$	0.106 ± 0.044	85.1 ± 1.5
HD 189733b	1.138 ± 0.025	$1.178^{+0.016}_{-0.023}$	0.03142 ± 0.00052	$2.21857312^{+3.6\times10^{-7}}_{-7.6\times10^{-7}}$	$0.0041^{+0.0025}_{-0.002}$	$85.51^{+1}_{-0.05}$
Kepler-5b	2.114 ± 0.064	1.431 ± 0.048	0.05064 ± 0.0007	$3.54846 \pm 3.2 \times 10^{-5}$	0	86.3 ± 0.6
TrES-1b	0.761 ± 0.05	1.099 ± 0.035	0.0393 ± 0.0007	$3.0300722 \pm 2 \times 10^{-7}$	0	88.4 ± 0.3
TrES-3b	$1.91^{+0.06}_{-0.08}$	$1.305^{+0.028}_{-0.09}$	0.0226 ± 0.0013	$1.30618608 \pm 3.8 \times 10^{-7}$	0	82.15 ± 0.21
WASP-2b	0.847 ± 0.045	1.079 ± 0.033	0.03138 ± 0.011	$2.1522254 \pm 1.5 \times 10^{-6}$	0	84.73 ± 0.19
WASP-12b	1.404 ± 0.099	1.736 ± 0.092	0.02293 ± 0.00078	$1.0914222 \pm 1.1 \times 10^{-6}$	$0^{+0.015}_{-0.01}$	86 ± 3
WASP-32b	3.6 ± 0.07	1.18 ± 0.07	0.0394 ± 0.0003	$2.71865 \pm 8 \times 10^{-5}$	0.018 ± 0.0065	85.3 ± 0.5

Note. — The planets above the horizontal line are the primary targets of this work; those below the line are those for which other transits have been observed, with each class in alphabetical order. All data are from Schneider (2011)

[a]WASP-33b is not detected by the radial velocity method due to its hot, fast-rotating host star; this is a 3σ upper limit on the mass.

Table 2.5. Transits of HAT-P-16 during the 2010-2011 observing season visible from VVO

Date	Start Time	Airmass	Date	Center Time	Airmass	Date	End Time	Airmass
July 18	01:34	1.410	July 18	03:06	1.138	July 18	04:03	1.021
July 29	*04:03*	*1.016*	*July 29*	*05:35*	*1.008*	*July 29*	*07:07*	*1.094*
Aug. 1	22:41	2.289	Aug. 2	00:13	1.532	Aug. 2	01:44	1.197
Aug. 13	01:10	1.176	Aug. 13	02:42	1.035	Aug. 13	04:14	1.001
Aug. 26	**22:17**	**1.632**	**Aug. 26**	**23:49**	**1.242**	**Aug. 27**	**01:21**	**1.062**
Sept. 7	00:47	1.171	Sept. 7	02:19	1.000	Sept. 7	03:50	1.147
Sept. 20	21:54	1.619	Sept. 20	23:25	1.086	Sept. 21	00:57	1.009
Oct. 2	00:23	1.051	Oct. 2	01:55	1.026	Oct. 2	03:27	1.362
Oct. 13	02:53	1.052	Oct. 13	04:25	1.481	Oct. 13	05:56	3.438
Oct. 15	21:30	1.290	Oct. 15	23:02	1.013	Oct. 16	00:34	1.076
Oct. 27	00:00	1.002	Oct. 27	01:31	1.118	Oct. 27	04:03	1.755
Oct. 29	18:37	1.945	Oct. 29	20:09	1.163	Oct. 29	21:41	1.000
Nov. 9	20:06	1.111	Nov. 9	21:38	1.004	Nov. 9	23:10	1.222
Nov. 20	22:36	1.015	Nov. 21	00:08	1.305	Nov. 21	01:40	2.568
Dec. 4	19:43	1.023	Dec. 5	21:15	1.056	Dec. 5	22:47	1.501
Dec. 29	19:19	1.001	Dec. 29	20:51	1.182	Dec. 29	22:23	2.025
Jan. 23	18:56	1.039	Jan. 23	20:28	1.426	Jan. 23	22:00	3.173

Note. — Observed transits are listed in bold type; transits that were partially observed are italicized. Times are in local time (EDT/GMT-4 before Nov. 7, EST/GMT-5 after Nov. 7).

Table 2.6. Transits of WASP-33b during the 2010-2011 observing season visible from VVO

Date	Start Time	Airmass	Date	Center Time	Airmass	Date	End Time	Airmass
July 15	03:03	1.666	July 15	04:23	1.279	July 15	5:45	1.089
July 25[a]	02:31	1.587	July 25	03:53	1.238	July 25	05:14	1.071
Aug. 6	**02:01**	**1.512**	**Aug. 6**	**03:22**	**1.204**	**Aug. 6**	**04:44**	**1.055**
Aug. 6	02:01	1.995	Aug. 6	03:22	1.204	Aug. 6	04:44	1.007
Aug. 17	01:30	1.450	Aug. 17	02:52	1.171	Aug. 17	04:13	1.042
Aug. 21	22:37	3.257	Aug. 21	23:58	1.945	Aug. 22	01:20	1.406
Aug. 28[b]	01:00	1.769	Aug. 28	02:21	1.145	Aug. 28	03:43	1.003
Sept. 8	00:29	1.679	Sept. 8	01:51	1.119	Sept. 8	03:12	1.003
Sept. 14	02:52	1.086	Sept. 14	04:14	1.007	Sept. 14	05:35	1.202
Sept. 18	23:59	1.593	Sept. 19	01:20	1.098	Sept. 19	02:42	1.005
Sept. 23	21:05	4.184	Sept. 23	22:27	1.638	Sept. 23	23:48	1.110
Sept. 25	02:22	1.068	Sept. 25	03:43	1.012	Sept. 25	05:05	1.239
Sept. 29	23:28	1.523	Sept. 30	00:50	1.077	Sept. 30	02:11	1.009
Oct. 4	20:35	3.670	Oct. 4	21:56	1.563	Oct. 4	23:17	1.090
Oct. 6	01:51	1.053	Oct. 6	3:13	1.020	Oct. 6	04:34	1.277
Oct. 10	**22:58**	**1.216**	**Oct. 11**	**00:19**	**1.061**	**Oct. 11**	**01:41**	**1.004**
Oct. 15	20:04	3.310	Oct. 15	21:26	1.490	Oct. 15	22:47	1.070
Oct. 17	**01:21**	**1.004**	**Oct. 17**	**02:42**	**1.028**	**Oct. 17**	**04:04**	**1.141**
Oct. 21[c]	*22:27*	*1.399*	*Oct. 21*	*23:49*	*1.046*	*Oct. 22*	*01:10*	*1.023*
Oct. 26	19:34	2.971	Oct. 26	20:55	1.431	Oct. 26	22:16	1.056
Oct. 28	00:50	1.028	Oct. 28	02:12	1.040	Oct. 28	03:33	1.369
Nov. 1	21:57	1.344	Nov. 1	23:18	1.034	Nov. 2	00:39	1.032
Nov. 3	03:13	1.061	Nov. 3	04:45	1.460	Nov. 3	04:56	3.125
Nov. 6	19:03	2.726	Nov. 6	20:25	1.373	Nov. 6	21:46	1.041
Nov. 7	23:20	1.019	Nov. 8	00:41	1.053	Nov. 8	02:03	1.426
Nov. 12 [d]	*20:26*	*1.300*	*Nov. 12*	*21:48*	*1.024*	*Nov. 12*	*23:09*	*1.045*
Nov. 14	01:43	1.079	Nov. 14	03:04	1.523	Nov. 14	04:26	3.488
Nov. 17	17:33	2.488	Nov. 17	18:54	1.326	Nov. 17	20:15	1.030
Nov. 18	22:49	1.012	Nov. 19	00:11	1.069	Nov. 19	01:32	1.485
Nov. 23	19:56	1.256	Nov. 23	21:17	1.016	Nov. 23	22:38	1.058
Nov. 25	01:12	1.098	Nov. 25	02:34	1.599	Nov. 25	03:55	3.900

Table 2.6 (cont'd)

Date	Start Time	Airmass	Date	Center Time	Airmass	Date	End Time	Airmass
Nov. 29	22:19	1.007	Nov. 29	23:40	1.086	Nov. 30	01:01	1.549
Dec. 4	**19:25**	**1.085**	**Dec. 4**	**20:47**	**1.010**	**Dec. 4**	**22:08**	**1.014**
Dec. 10	21:48	1.004	Dec. 10	23:10	1.108	Dec. 11	00:31	1.632
Dec. 15	18:55	1.186	Dec. 15	20:16	1.005	Dec. 15	21:37	1.094
Dec. 21	21:18	1.002	Dec. 21	22:39	1.130	Dec. 22	00:00	1.712
Dec. 26	18:24	1.158	Dec. 26	19:45	1.003	Dec. 26	21:07	1.117
Jan. 1	20:47	1.003	Jan. 1	22:09	1.158	Jan. 1	23:30	1.818
Jan. 6	17:54	1.130	Jan. 6	19:15	1.002	Jan. 6	20:36	1.140
Jan. 12	20:17	1.006	Jan. 12	21:38	1.186	Jan. 12	22:59	1.922
Jan. 23[d]	**19:46**	**1.062**	**Jan. 23**	**21:07**	**1.218**	**Jan. 23**	**22:29**	**1.546**
Feb. 3[d]	**19:16**	**1.080**	**Feb. 3**	**20:37**	**1.256**	**Feb. 3**	**21:58**	**1.619**
Feb. 14	18:45	1.024	Feb. 14	20:06	1.296	Feb. 14	21:28	2.381

Note. — Observed transits are listed in bold type; transits that were partially observed are italicized. Times are in local time (EDT/GMT-4 before Nov. 7, EST/GMT-5 after Nov. 7). Unobserved transits were missed due to poor weather unless otherwise noted.

[a]Not observed due to problems with the CCD camera.

[b]Not observed due to conflict with WASP-3b transit (see Table 2.7).

[b]Obscured by clouds before ingress.

[c]Observations started too close to ingress to obtain good data.

[d]Observed simultaneously at Swarthmore College, Peter van de Kamp Observatory.

2.2.2 WASP-3b

In addition to the observations of WASP-33b and HAT-P-16b detailed above, we also took part in a multi-institutional international campaign of observations of transits of WASP-3b. Maciejewski et al. (2010a) presented evidence for TTVs of this planet, suggesting the presence of a second planet in the system, WASP-3c. Their best fit suggests a planet with a mass of $\sim 15 M_{\oplus}$ and located in the exterior 2:1 resonance with WASP-3b; such a planet would have a period of ∼3.7 days. We observed two transits during the fall of 2010, in collaboration with Maciejewski et al. and a similar observing project at Swarthmore College, also using a 24-inch telescope, albeit of a newer design than that at VVO. Observations of WASP-3b transits are detailed in Table 2.7.

Table 2.7. Transits of WASP-3b during the 2010-2011 observing season visible from VVO

Date	Start Time	Airmass	Date	Center Time	Airmass	Date	End Time	Airmass
July 9	01:08	1.006	July 9	02:28	1.113	July 9	03:48	1.647
July 21	23:34	1.005	July 22	0:44	1.042	July 22	2:04	1.169
Aug. 2	01:21	1.169	Aug. 2	02:41	1.440	Aug. 2	04:01	2.013
Aug. 3	21:40	1.023	Aug. 3	23:00	1.009	Aug. 4	00:20	1.073
Aug. 14	*23:37*	*1.074*	*Aug. 15*	*00:57*	*1.240*	*Aug. 15*	*02:17*	*1.586*
Aug. 27	**21:53**	**1.022**	**Aug. 27**	**23:13**	**1.116**	**Aug. 28**	**00:33**	**1.331**
Sept. 9	20:09	1.030	Sept. 9	21:29	1.043	Sept. 9	22:49	1.375
Sept. 20	22:06	1.061	Sept. 20	23:26	1.448	Sept. 21	00:46	3.081
Oct. 3	20:22	1.016	Oct. 3	21:42	1.245	Oct. 3	23:02	2.157
Nov. 9	17:51	1.063	Nov. 9	19:11	1.456	Nov. 9	20:21	3.120
Mar. 6	02:16	2.925	Mar. 6	03:36	1.419	Mar. 6	04:55	1.056
Apr. 12	01:44	2.078	Apr. 12	03:04	1.225	Apr. 12	04:24	1.013
Apr. 25	00:01	2.890	Apr. 25	01:20	1.416	Apr. 25	02:40	1.054
May 6	01:57	1.348	May 6	03:17	1.037	May 6	04:37	1.036
May 19	00:13	1.613	May 19	01:33	1.104	May 19	02:53	1.007

Note. — Observed transits are listed in bold type; transits that were partially observed are italicized. Times are in local time (EDT/GMT-4 before Nov. 7 and after Mar. 13, EST/GMT-5 between Nov. 7 and Mar. 13).

2.2.3 Other Systems

On nights when there was no transit of HAT-P-16b, WASP-33b, or WASP-3b, transits of other known planets were observed. These observed transits are listed in Table 2.8, while the properties of these stars are given in the second part of Table 2.3 and the planets in the second part of Table 2.4. To date, 13 full transits have been successfully observed. Several other transits were also observed, but either the data are of poor quality or the observations were interrupted by clouds.

Table 2.8. Observations of other transiting systems during the 2010-2011 observing season

Planet Name	Start Date	Start Time	Start Airmass	Center Date	Center Time	Center Airmass	End Date	End Time	End Airmass	Comments
HAT-P-14b	July 1	23:50	1.004	July 2	00:56	1.044	July 2	02:01	1.141	mild defocusing
Kepler-5b	July 3	22:45	1.226	July 4	01:12	1.013	July 4	03:39	1.053	
TrES-3b	July 5	23:49	1.002	July 6	00:28	1.012	July 6	01:07	1.040	data of poor quality
TrES-1b	July 18	00:16	1.004	July 18	01:31	1.041	July 18	02:46	1.157	interrupted by clouds
WASP-2b	July 29	23:24	1.306	July 30	00:18	1.233	July 30	01:12	1.227	
HD 189733b	July 30	23:47	1.063	July 31	00:41	1.061	July 31	01:36	1.104	
HAT-P-5b	Aug. 7	00:06	1.092	Aug. 7	01:33	1.303	Aug. 7	03:03	1.773	interrupted by clouds
HAT-P-14b	Aug. 8	00:21	1.256	Aug. 8	01:26	1.522	Aug. 8	02:32	2.018	
WASP-2b	Aug. 14	00:58	1.270	Aug. 14	01:52	1.393	Aug. 14	02:46	1.631	
HAT-P-11b	Aug. 28	02:32	1.401	Aug. 28	03:41	1.752	Aug. 28	04:50	2.373	data of poor quality
HAT-P-11b	Sept. 1	23:50	1.071	Sept. 2	00:59	1.185	Sept. 2	04:08	1.385	
CoRoT-Exo-2b	Oct. 8	20:00	1.341	Oct. 8	21:11	1.517	Oct. 8	22:21	1.944	
WASP-32b	Oct. 23	21:29	1.442	Oct. 23	22:32	1.322	Oct. 23	23:45	1.343	interrputed by clouds
HAT-P-23b	Nov. 2	20:55	1.310	Nov. 2	22:00	1.614	Nov. 2	23:05	2.263	
WASP-32b [ab]	Nov. 11	21:03	1.320	Nov. 11	22:16	1.431	Nov. 11	23:29	1.751	
HAT-P-13b	Dec. 24	21:02	1.695	Dec. 24	22:39	1.274	Dec. 25	00:16	1.078	data of poor quality
CoRoT-Exo-1b	Feb. 22	20:04	1.413	Feb. 22	21:17	1.438	Feb. 22	22:31	1.645	data not yet reduced
WASP-12b	Mar. 3	19:46	1.023	Mar. 3	21:14	1.088	Mar. 3	22:42	1.291	data not yet reduced
HAT-P-12b	Mar. 29	01:58	1.004	Mar. 29	03:08	1.011	Mar. 29	04:18	1.073	data not yet reduced

Note. — Times are in local time (EDT/GMT-4 before Nov. 7 and after Mar. 13, EST/GMT-5 between Nov. 7 and Mar. 13).

[a]Observed simultaneously at Swarthmore College, Peter van de Kamp Observatory.

[b]Observed simultaneously at Gettysburg College.

Chapter 3

Data Reduction and Error Analysis

3.1 Data Reduction

Before we can learn anything from the transit data we first need to reduce the images to get them into a usable form. The data reduction pipeline utilizes both IRAF and IDL procedures, as outlined in Leiner (2010). The data first undergo flat field, dark, and bias correction using standard IRAF tasks. A custom IDL task, CENTFWHM, is then used to determine the centroid and full width half maximum (FWHM) of the target star and each comparison star in each image, which requires the manual input of a box around each star for the routine to search. This is accomplished by fitting a two-dimensional Gaussian function to the PSF. A second custom routine, CENTDIAG, compiles a number of diagnostic plots, such as centroid pixel drift, variations of FWHM over time, etc. Examples of such plots are shown in Figs. 3.1 and 3.2.

A third IDL routine, DOAPER, performs the actual photometry by calling on the standard IDL aperture photometry routine APER and also computes the flux differences necessary for differential photometry. Finally, the APERTEST routine uses the data from DOAPER to construct a transit lightcurve. It performs a linear

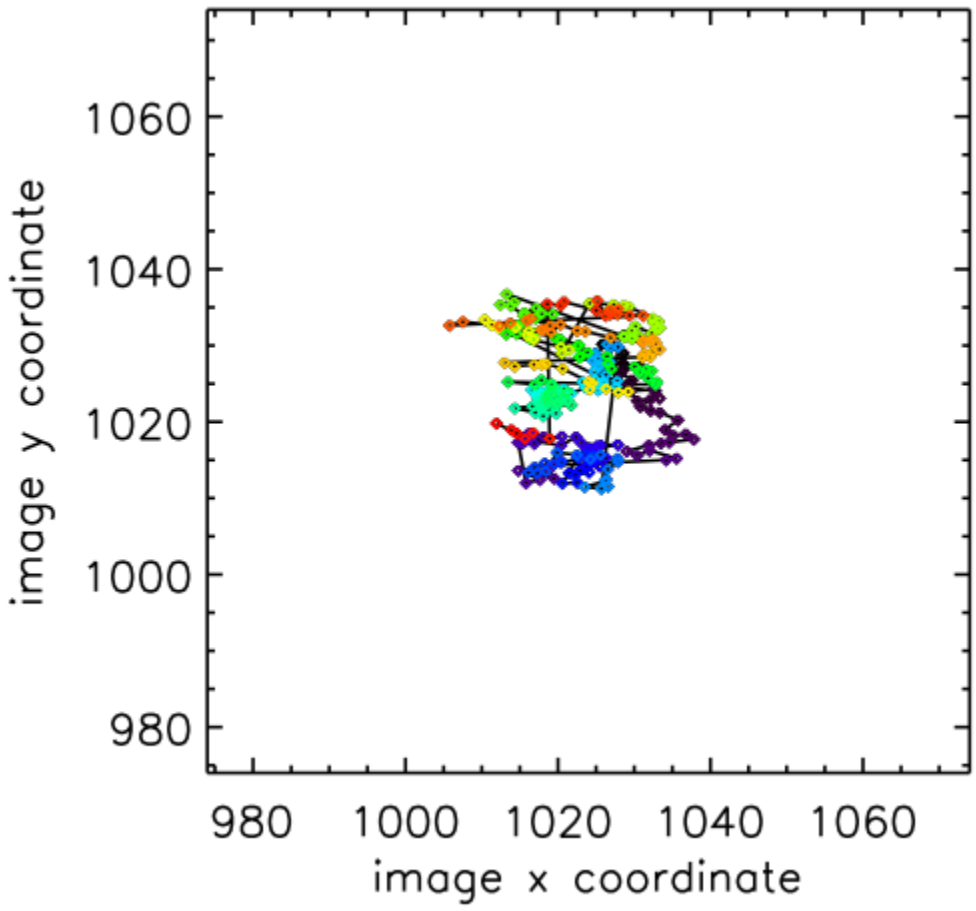

Figure 3.1: Drift in the position of the target centroid over time for the WASP-3b transit of 2010 August 27-28. The progression of colors of the points indicates their time order, with the earliest points in purple and the latest points in red.

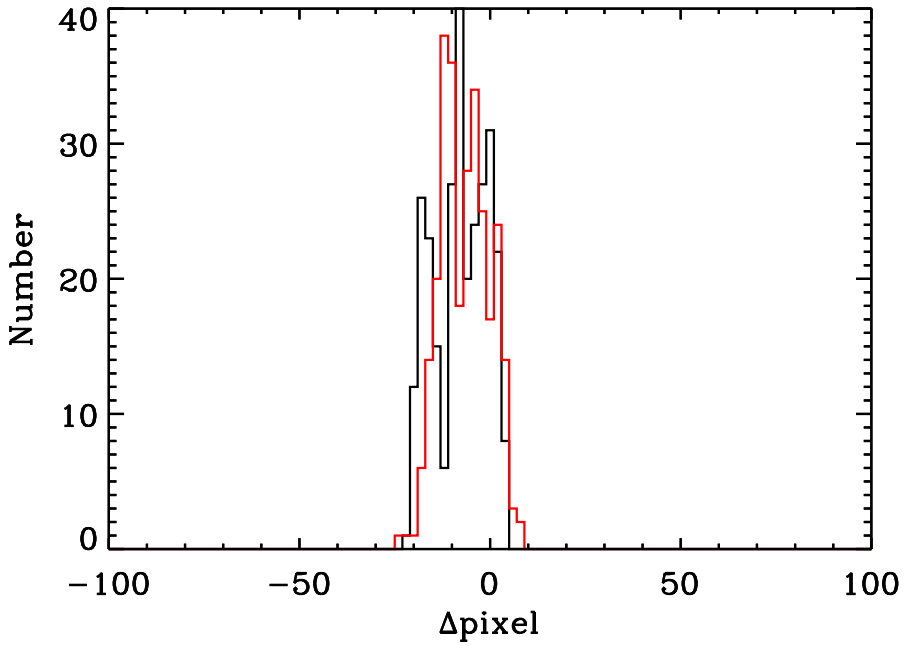

Figure 3.2: Histogram of the pixel drift on the x and y axes during the WASP-3b transit of 2010 August 27-28. For each i^{th} exposure, $\Delta x = x_i - x_0$, and similarly for y. The x drift is plotted in black and the y drift in red. The standard deviation of the distribution is 6.3 pixels in the x direction and 6.9 pixels in the y direction.

fit to the out-of-transit lightcurve and divides the differential flux by the fit in order to produce a normalized lightcurve. This lightcurve is then passed to the fitting routine.

3.1.1 Lightcurve Fitting

After the data reduction has been completed a lightcurve needs to be fit to the data; this fit includes parameters such as the planetary and stellar radii and the orbital inclination. I used the IDL routines written by Leiner (2010), based upon the formulae presented in Mandel & Agol (2002) and the venerable AMOEBA algorithm (Press 1988), which utilizes the downhill simplex method first introduced by Nelder (1965).

Leiner (2010) produced two versions of the lightcurve fitting routines, one with fitted limb darkening parameters and the other with these parameters held fixed; both versions used a quadratic limb darkening law, as described in Mandel & Agol (2002). I found that fitting the limb darkening gave noticeably poorer fits to the data or resulted in unphysical light curves, as shown in Fig. 3.3, so for all of the fits discussed hereafter I fix the limb darkening parameters at those given for the I band by Claret et al. (1995) for the stellar parameters closest to those listed in the literature for each host star. I use this source rather than the more recent Claret (2000) as the latter source does not include the quadratic limb-darkening parameters required by the Leiner (2010) routines.

The free parameters for the fitting routine are the stellar and planetary radii, inclination, and transit centroid, while the semimajor axis and orbital period are fixed at the literature values. The routine also assumes zero eccentricity, which is a good assumption for most hot jupiters; however, some planets, such as HAT-

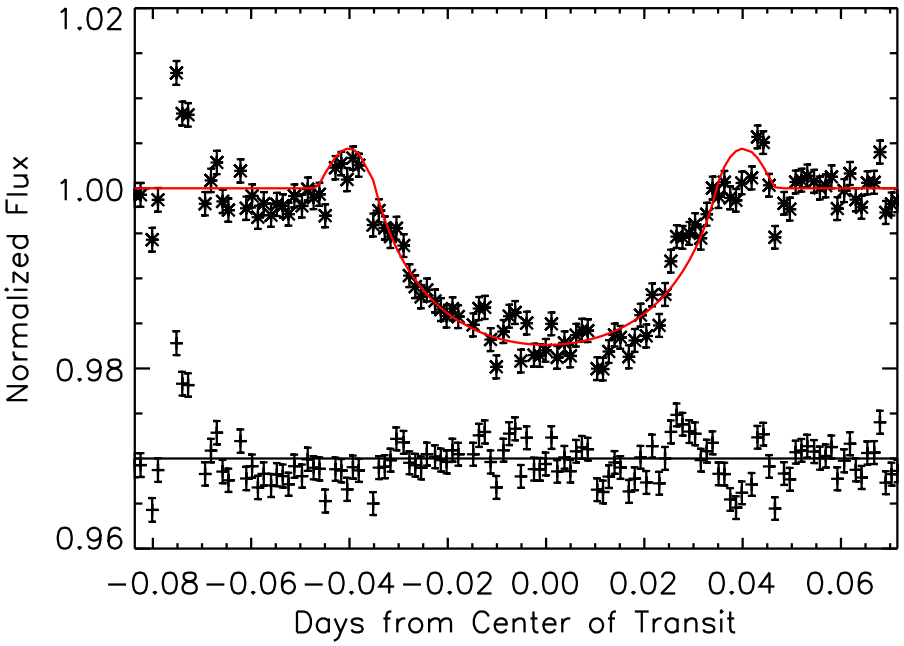

Figure 3.3: WASP-2b transit of 2010 July 29-30 fit with free limb darkening coefficients. Note the unphysical light curve, with peaks at ingress and egress. See Figs. 4.1 and 4.18 for the best-fit lightcurve with fixed limb darkening coefficients.

P-16b, show non-zero eccentricities. Modifying the fitting routines to account for this is an area for future work.

For those systems where we observe multiple transits, we fit the transits both individually and jointly. For the joint fits the planetary and stellar radii and inclination are the same for each transit, with a different centroid for each transit. As originally coded by Leiner (2010) the routine could only handle up to four transits at once, so I modified it to fit up to six transits at once, since we observed six transits of WASP-33b (Table 2.6).

3.2 Error Analysis

It is a relatively straightforward matter to determine the photometric errors on the data from photon noise, read noise, etc.; indeed, these tasks are handled automatically by the Leiner (2010) routines. It is more difficult, however, to assess systematic errors and their effect on the data. In this section we explore various sources of systematic error and the deviations of the data from the Gaussian statistics caused by photometric noise, while in §3.3 we consider methods of quantifying the errors. Of particular importance is correlated ("red") noise, which seems to be a major problem for our data.

3.2.1 Pixel Drift

The 24" telescope suffers from pixel drift due to imperfect tracking and occasional backlash, as described in §2.1.2. We performed an analysis to determine the relationship between pixel drift and systematics in the light curves, which appear to be correlated with large degrees of pixel movement. We also search for correlations between the position of the stellar centroid on the CCD chip and the residuals to the lightcurve fits. An example of correlated noise is shown in Fig. 3.4. A comparison between pixel shifts and systematics in a lightcurve is shown in Fig. 3.5. Similar correlated noise has been seen by other teams, e.g. Steele et al. (2008), due simply to drift of the PSF across the CCD; compare Fig. 9 of Steele et al. (2008).

To investigate the effects of pixel drift on the residuals, for each of the N data points in a set of transit observations, the parameters Δx, Δy, Δr were calculated, where $\Delta x = x_i - x_{i-1}$, $\Delta y = y_i - y_{i-1}$, $\Delta r = \sqrt{(\Delta x^2) + (\Delta y^2)}$. The results of

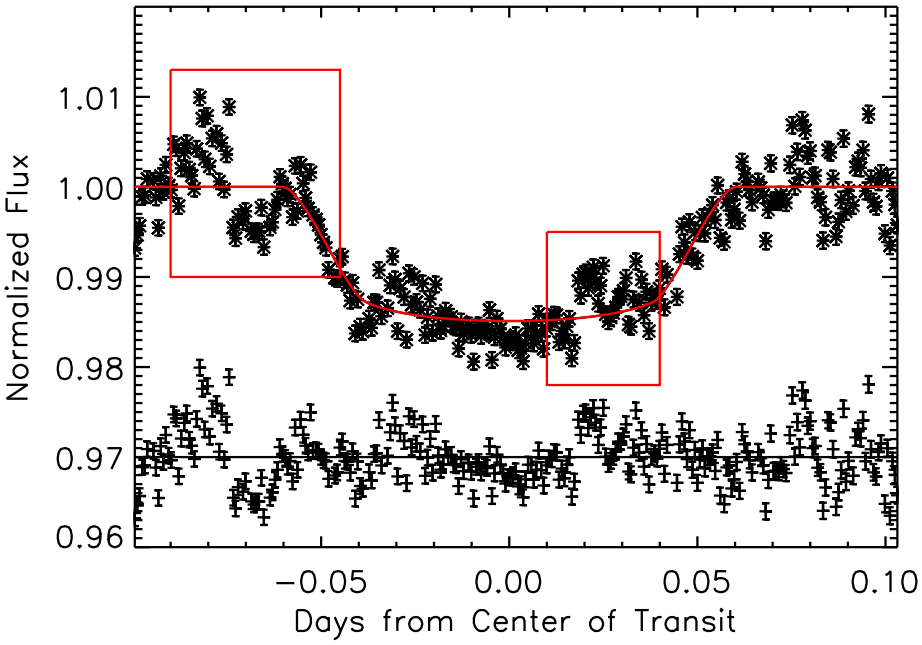

Figure 3.4: Transit lightcurve of WASP-3b, 2010 August 27-28. Correlated (red) noise has been highlighted in the red boxes.

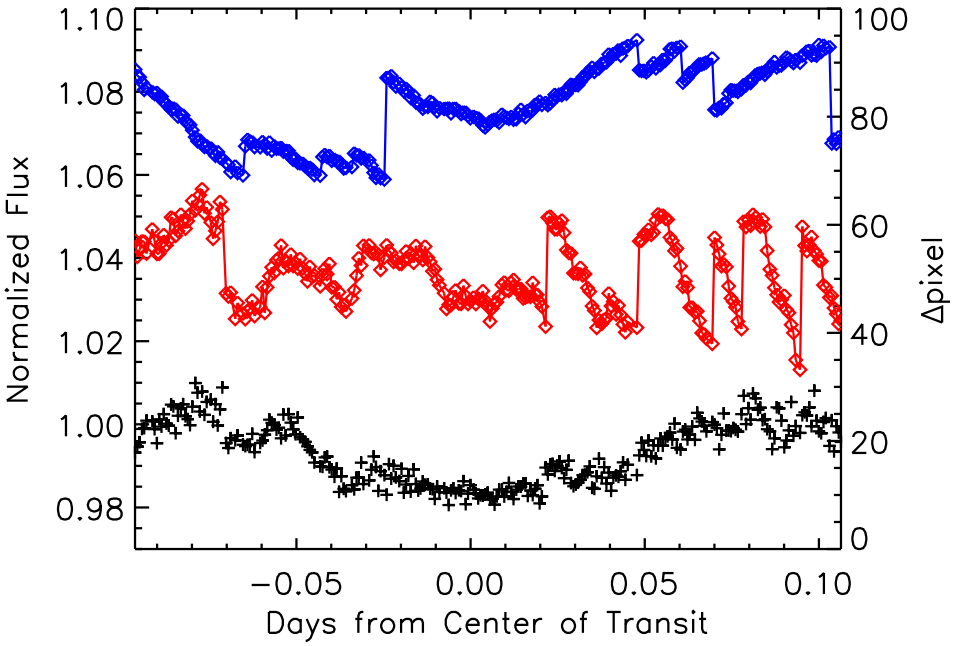

Figure 3.5: WASP-3b transit of 2010 August 27-28, with the pixel centroid shifts overplotted, Δx in red, Δy in blue. The centroid shifts are offset by an arbitrary amount. No error bars or best fit for the transit are plotted for clarity. Note correspondences between large pixel shifts and discontinuities in the lightcurve.

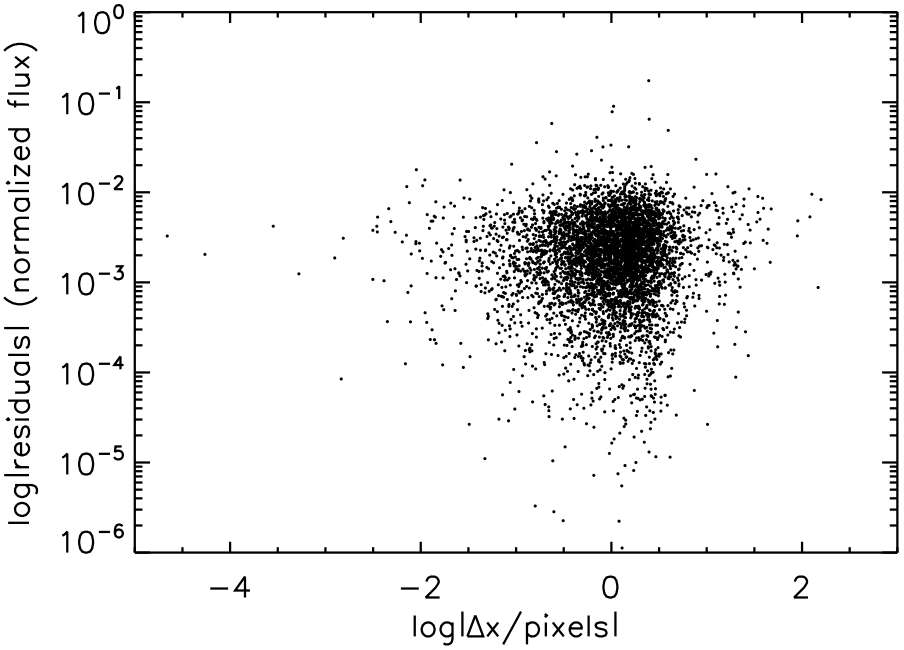

Figure 3.6: Absolute values of the residuals to the best-fit lightcurves as a function of difference in the x_i, x_{i-1} (Δx) positions on the CCD of the target centroid.

this analysis are presented in Figs. 3.6 and 3.7. These figures show the absolute values of the residuals as a function of, respectively, Δx and Δy. 5208 data points from 17 transits were used in this analysis. No trend is seen in this analysis, so for each $\Delta x, y, r$ point I computed the root-mean-square (RMS) of the $i, ..., i+4$ points and plotted these as a function of $\Delta x, y, r$. Binning by 5 points was chosen as a representative small bin size. These are plotted in Fig. 3.8. Again, no trend is visible.

How are we to reconcile the obvious discontinuities seen in Figs. 3.4 and 3.5 with the apparent lack of such discontinuities in Figs. 3.6, 3.7, and 3.8? Two possibilities spring to mind. It may be that the deviant residuals do not occur at exactly the same exposure as the pixel jumps, blurring the signal. Alternatively, correlated noise could also be caused by less sudden pixel drift, again blurring the

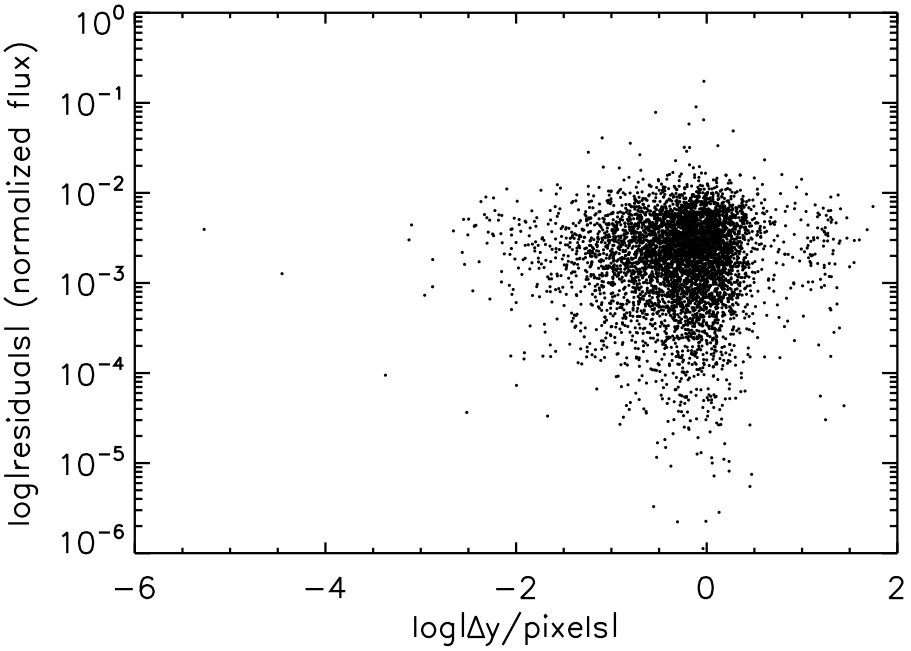

Figure 3.7: Absolute values of the residuals to the best-fit lightcurves as a function of difference in the y_i, y_{i-1} (Δy) positions on the CCD of the target centroid.

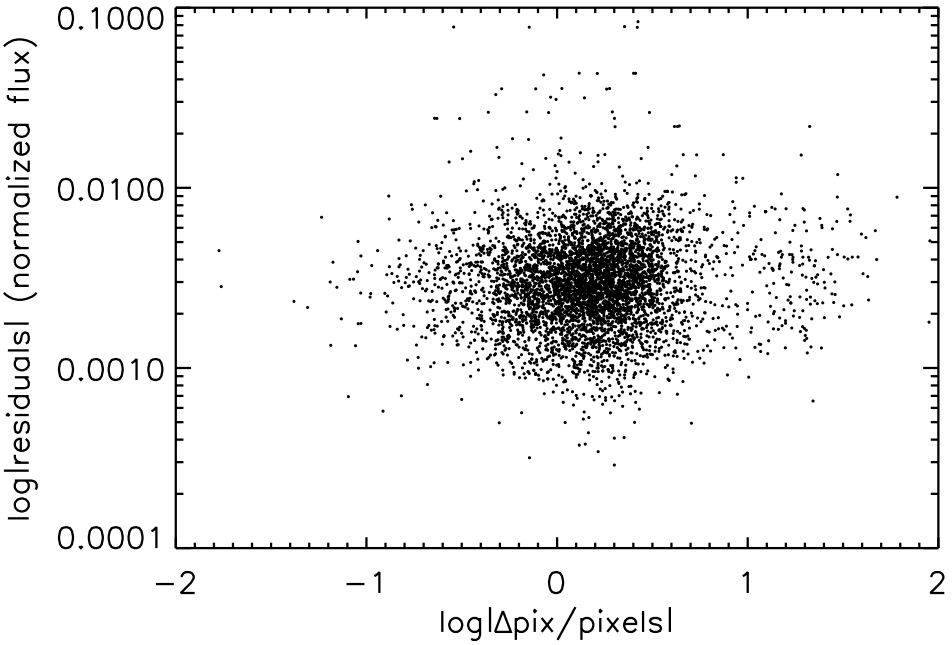

Figure 3.8: Absolute values of the residuals to the best-fit lightcurves as a function of difference in the r_i, r_{i-1} ($r = \sqrt{x^2 + y^2}$, Δr) positions on the CCD of the target centroid with 5-datapoint binning, as described in the text.

signal. Finally, we have included both photometrically clean and photometrically noisy transits in the sample, possibly again hiding the signal.

For the comprehensive data set (here 5224 data points for 17 transits) we assigned the RMS of the residuals for all observations in a given pixel to that pixel. The results are plotted in Fig. 3.9. It is apparent that most of the observations took place over a region near the center of the chip, with some other exposures existing farther away from the center due to pixel drift and backlash. There is a relatively uniform distribution around the center of the chip, illustrating that drift exists in both the RA and Dec axes. There are, however, some isolated clusters of points far out along the x axis, illustrating the backlash in the system that occasionally causes the telescope to jerk tens of pixels in RA, sometimes in mid-exposure. Most of the pixels show relatively low RMS, but there are a number of pixels with higher RMS, apparently randomly scattered about the relevant region of the CCD. No significant structures are apparent.

For comparison, Fig. 3.10 displays how many data points were collected on each pixel of the CCD. The points obviously cluster about the square region of the center of the chip where the centroid is kept through recentering.

From the above analysis it seems that pixel drift is indeed a serious issue. Work is currently ongoing on an autoguider for the Perkin Telescope, which will solve this issue and should improve the quality of our observations (J. Schaeffer, personal communication 2011).

3.2.2 Gaussian Error Analysis

We performed an analysis in order to determine to what extent our errors are Gaussian and to what extent the noise is correlated (e.g., Croll et al. 2011).

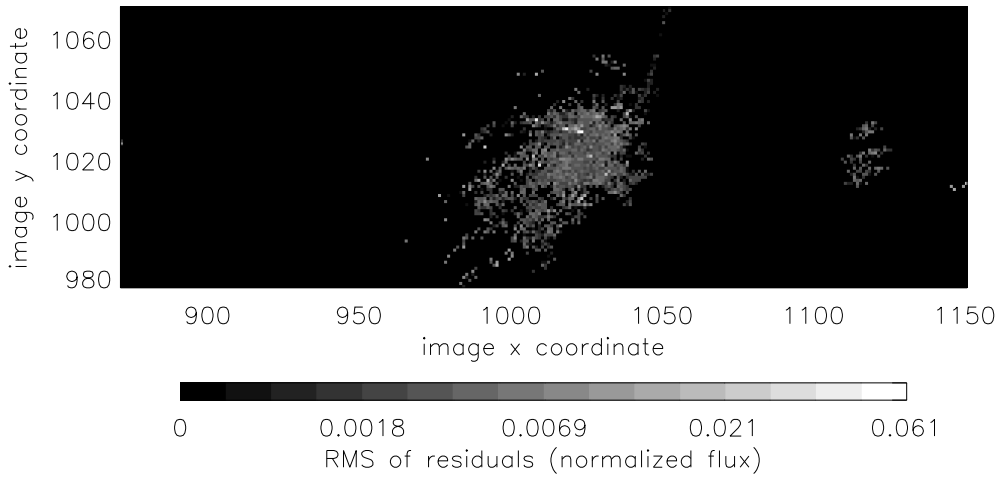

Figure 3.9: Root-mean-square of the residuals to the best-fit lightcurves as a function of target centroid position on the CCD chip. The median of the distribution is 0.0029 in units of normalized flux.

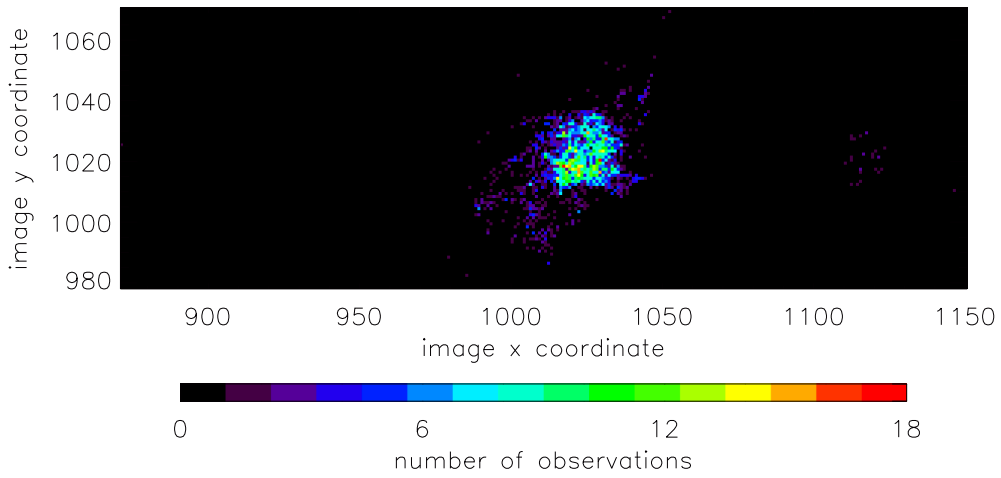

Figure 3.10: Number of data points used for the analysis described in §3.2.1 as a function of position on the CCD.

The out-of-transit residuals for each transit were computed, and then each $n = 1, 2, \ldots N$ points binned and the RMS of the resulting binned data computed. If the noise is Gaussian then the RMS will follow a $n^{-\frac{1}{2}}$ trend, whereas any systematics or correlated noise will cause the binned data to lie above $n^{-\frac{1}{2}}$. Plots showing the RMS as a function of number of binned points are shown in Figs. 3.11 through 3.16. Figs. 3.11, 3.12 and 3.13 show all of the transits with the same vertical scale, displaying the different noise levels in each transit, whereas Figs. 3.14, 3.15, and 3.16 display each transit with its own vertical scale. Our data range from nearly Gaussian to significantly non-Gaussian. Several transits actually lie below $n^{-\frac{1}{2}}$. The reason for this is unclear, though it may be simply due to small number statistics. The most obvious example of low values is the Oct. 8 transit of CoRoT-Exo-2b (Figs. 3.12, 3.15); this transit only has 70 exposures for the entire transit. Another sub-$n^{-1/2}$ transit, that of HAT-P-23 (again, Figs. 3.12, 3.15), has 85 exposures. Compare this to the WASP-33b transits, which have ∼400-700 exposures each. It thus seems clear that this is simply a result of a small number of data points.

3.3 Error Determination

The routines of Leiner (2010) provide a simple error estimation protocol using a χ^2 confidence interval test, as described in §3.0.5 of that work. As discussed there, however, this is not a rigorous error determination method. Moreover, the routine has a tendency in some cases to not be able to find a χ^2 minimum, resulting in no error determination. It is thus necessary to explore other methods of calculating the errors.

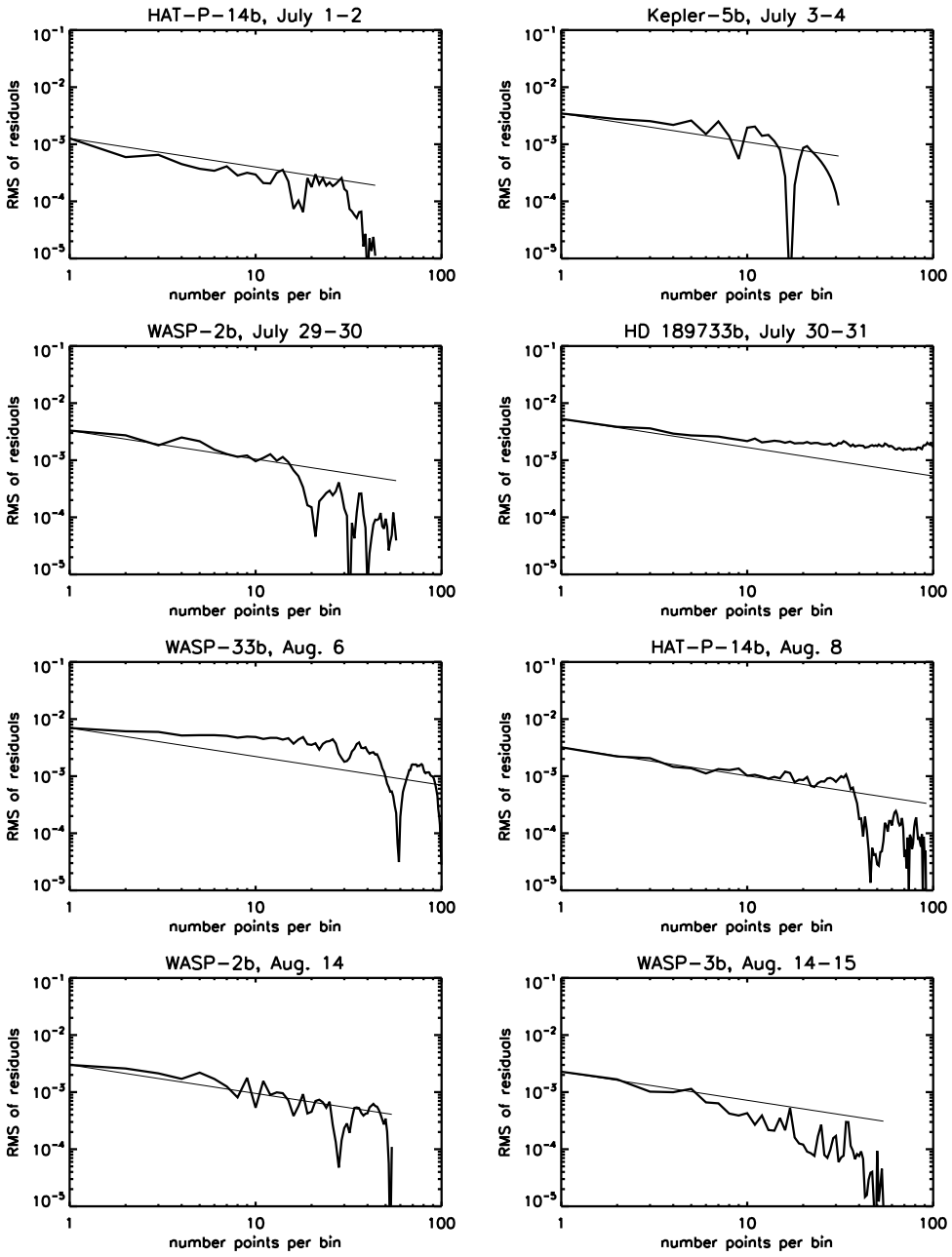

Figure 3.11: Gaussian errors for observed transits. Each plot is labeled with the name and date of the transit. All plots have the same vertical scale.

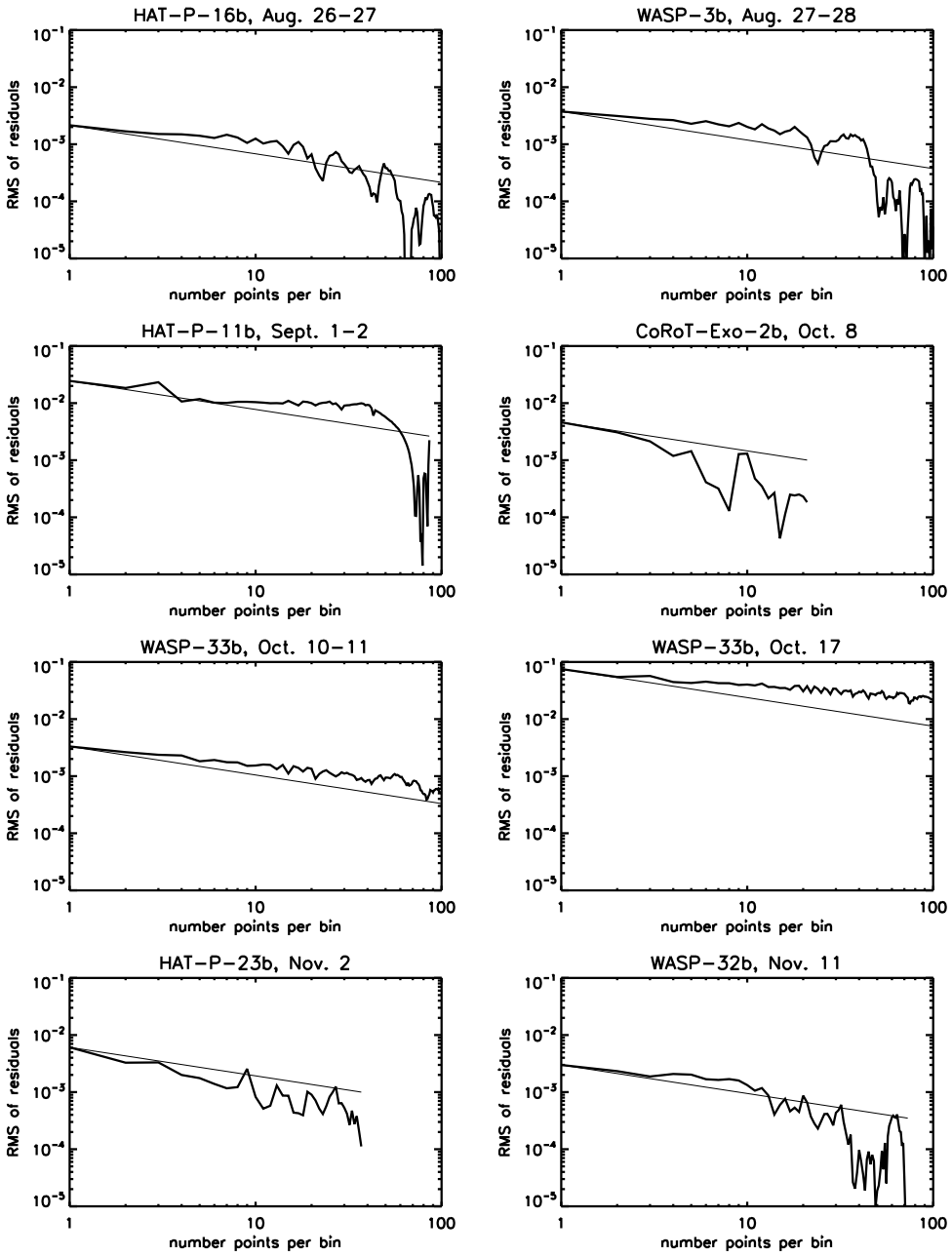

Figure 3.12: Gaussian errors for observed transits. Each plot is labeled with the name and date of the transit. All plots have the same vertical scale.

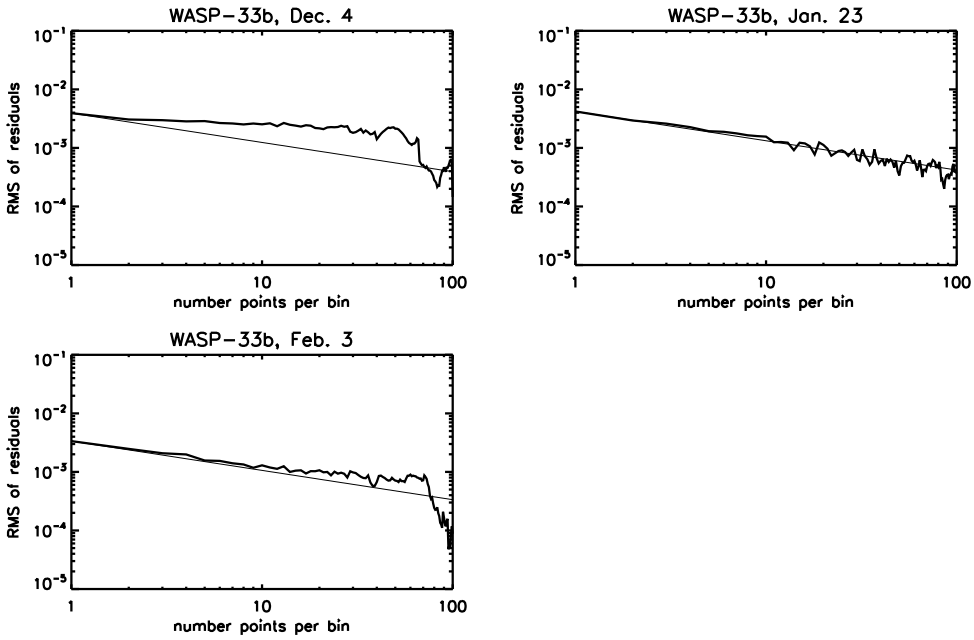

Figure 3.13: Gaussian errors for observed transits. Each plot is labeled with the name and date of the transit. All plots have the same vertical scale.

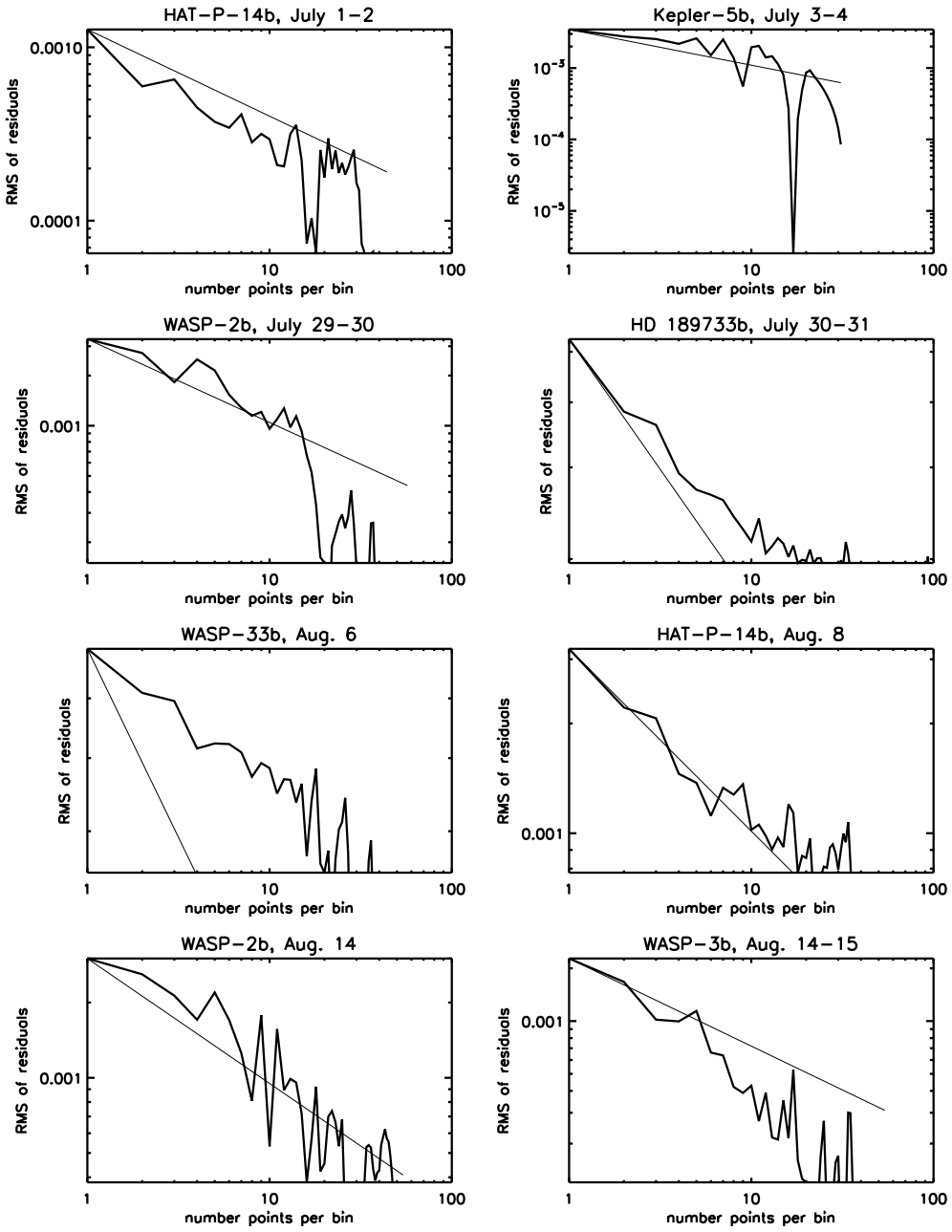

Figure 3.14: Gaussian errors for observed transits. Each plot is labeled with the name and date of the transit. All plots are scaled individually.

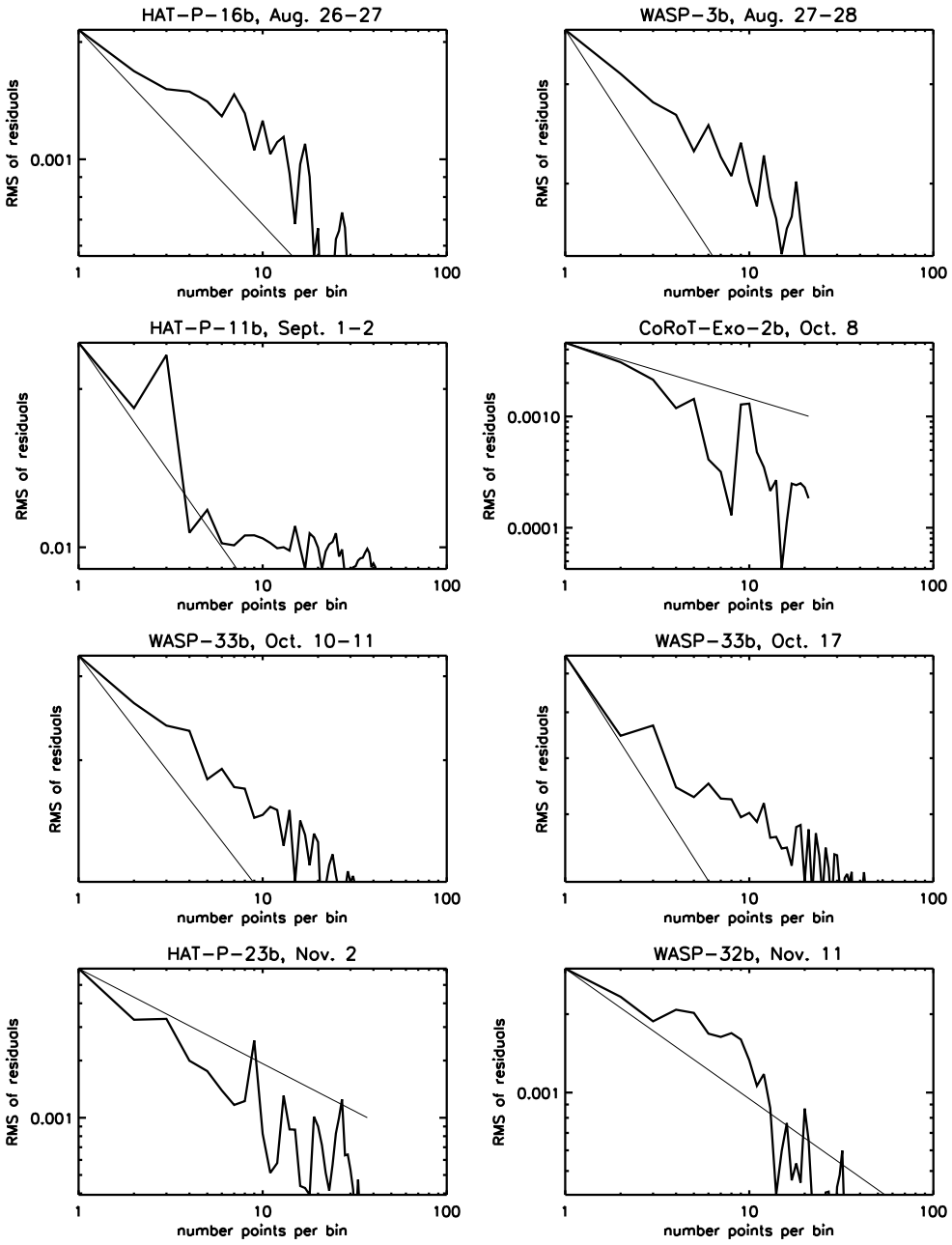

Figure 3.15: Gaussian errors for observed transits. Each plot is labeled with the name and date of the transit. All plots are scaled individually.

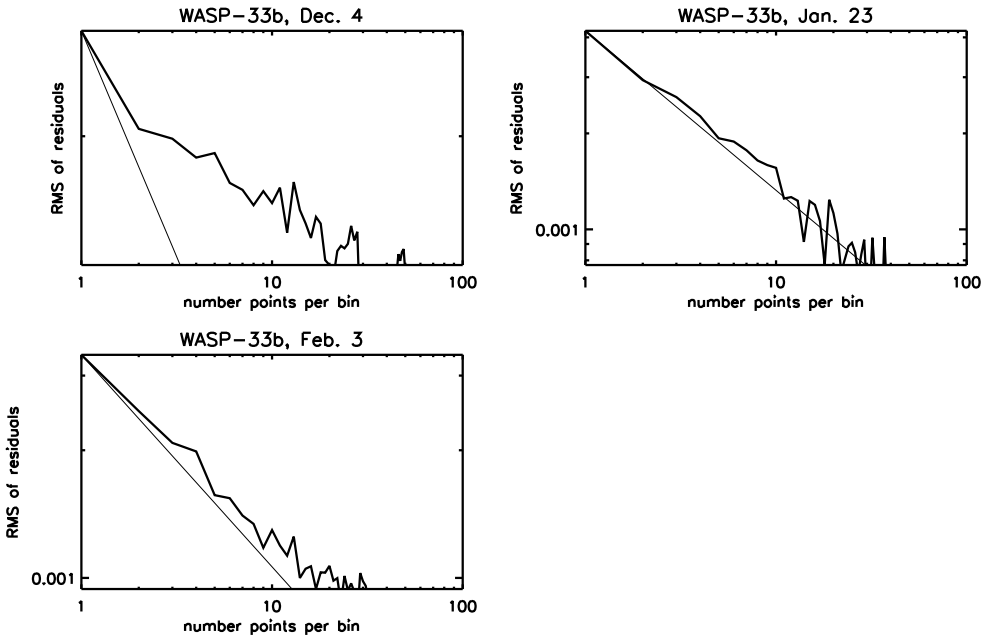

Figure 3.16: Gaussian errors for observed transits. Each plot is labeled with the name and date of the transit. All plots are scaled individually.

3.3.1 Markov Chain Monte Carlo

While the determination of photometric errors, including readout noise, is a simple process, one that is handled easily by the IDL task APER, sources of systematic error also need to be considered. Perhaps the most rigorous method of estimating the impact of these errors is using the Markov Chain Monte Carlo (MCMC) algorithm. The use of MCMCs for error analysis is outlined in Appendix A of Tegmark et al. (2004) This method has been applied extensively to the analysis of transit errors (e.g., Winn et al. 2007a,b).

Essentially, in order to perform a MCMC simulation, the data and a model are considered. The model parameters are selected randomly to form some set J_i, and the model is then fit to the data. Next the model parameters are adjusted randomly according to a Gaussian distribution (one "jump"), and the new model parameters J_{i+1} are fit to the data and the reduced χ^2 ($\chi^2_\nu = \chi^2/N_{dof}$, where N_{dof} is the number of degrees of freedom) is computed.

If $\chi^2_{\nu,i} \leq \chi^2_{\nu,i+1}$ then the jump is accepted, and we set $J_i = J_{i+1}$. If, however, $\chi^2_{\nu,i} > \chi^2_{\nu,i+1}$, then the jump is executed with probability $\exp(-\Delta\chi^2_\nu/2)$ (other probability functions can be used; this is the one adopted by Winn et al. 2007b). After the simulation has converged, a period known as "burn-in," the model parameters selected are a random sampling of the probability function; thus, the errors on the model parameters can be estimated by calculating the 1σ, 2σ, etc. values of these distributions.

One possible source of error that is often not considered robustly is the effect of stellar limb-darkening coefficients on the lightcurve. These coefficients are primarily responsible for the shape of the lightcurve between second and third contact and also play a part during ingress and egress (Mandel & Agol 2002).

These coefficients, however, can be difficult to determine.

Two primary methods have been used with regards to limb-darkening coefficients. The first is to determine these coefficients from stellar atmospheric models, as tabulated in sources such as Claret (2000) or Claret et al. (1995) for a range of different stellar properties. The coefficients are then simply inserted into the lightcurve-fitting program and not allowed to vary. This method has been utilized by e.g., Holman et al. (2006); Southworth et al. (2007), among others. The second method is to leave the limb-darkening coefficients as free parameters during the fit, an approach adopted by e.g. ,Kipping & Bakos (2011), although this is most appropriate for very high signal-to-noise (S/N) data, such as that from *Kepler* used by these authors.

Winn et al. (2007b) adopt a hybrid approach. They input coefficients derived from a source such as Claret (2000) and use these as initial guesses; their χ^2 is weighted such that the limb-darkening coefficients are biased to stay within 20% of the input values. Quantitatively, their χ^2 function is

$$\chi^2 = \sum_{j=1}^{1149} \left[\frac{f_j(obs) - f_j(calc)}{\sigma_j} \right]^2 + \left[\frac{(I_1/I_0) - 0.43}{0.086} \right] \tag{3.1}$$

where

$$\frac{I_1}{I_0} = \frac{1}{1 - u_1 - u_2} \tag{3.2}$$

where u_1 and u_2 are the quadratic limb-darkening coefficients. There are 1149 points in the data set. We adopt this weighted χ^2 function for our MCMC.

Despite the fact that some calculated parameters of the lightcurve, such as the depth, depend critically on the limb darkening, others do not. My tests have shown that the transit centroids are largely insensitive to the limb-darkening

parameters. Thus, the exact limb-darkening method adopted should not have much effect upon the results of this work, which focus on transit timing.

Our MCMC algorithm was tested on the data used by Winn et al. (2007b), available online at the NASA/IPAC/NExSci Star and Exoplanet Database (NStED)[1]. The results of this simulation were checked against those of Winn et al. (2007b) in order to confirm that our algorithm was functioning properly and giving self-consistent results.

Despite much work on the MCMC, I have been unable to make it work correctly. The chain converges within a few thousand iterations, but despite the χ^2 penalty on the limb darkening coefficients these parameters wander into unphysical regions of parameter space. While our final parameter distributions are relatively well-behaved, they are larger than those computed by Winn et al. (2007b) by more than an order of magnitude, as displayed in Figs. 3.17 and 3.18. Completing the development of our MCMC is a topic for future work.

3.3.2 Transit Analysis Package

Due to the problems with implementing our own MCMC, we also utilized an error analysis and transit fitting algorithm built into the Transit Analysis Package (TAP; Gazak et al. 2011). TAP fits the lightcurves using the equations of Mandel & Agol (2002), together with a treatment of the red noise using the wavelet-fitting approach of Carter & Winn (2009). In our TAP runs we have adopted an approach similar to that of Winn et al. (2007b), adding a Gaussian penalty term for the limb darkening coefficients to the χ^2 parameter; TAP includes a provision for adding such a penalty term for any of the fit parameters.

While TAP seems to mostly give good results, there are notable exceptions.

[1] http://nsted.ipac.caltech.edu/

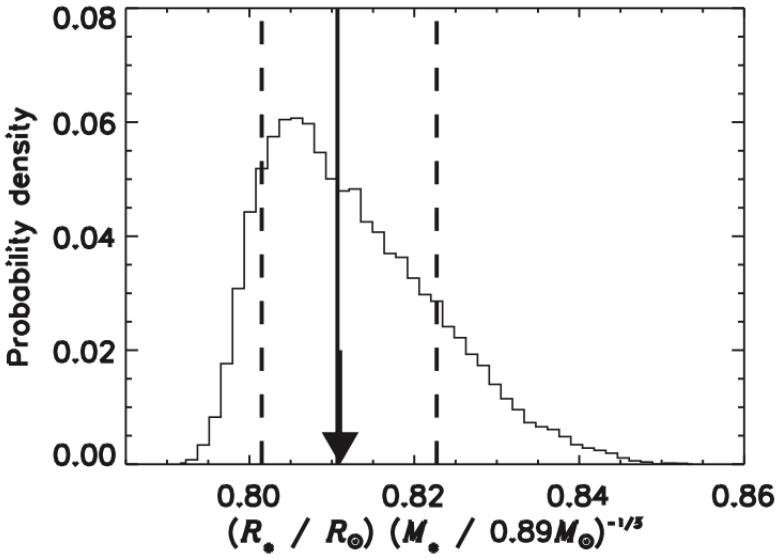

Figure 3.17: The probability distribution of the stellar radius of TrES-1, from Fig. 3 of Winn et al. (2007b). Compare to our results in Fig. 3.18. The solid line displays the median value of the stellar radius, the arrow the value which minimizes χ^2, and the dashed lines the 68% (1-σ) confidence interval.

As discussed in greater detail in §3.3.5, for somewhat noisy transits it can produce unplausibly large error bars (e.g., 0.61 days, longer than the length of the dataset!), or refuse to fit the transit at all and find a transit centroid time outside of the dataset. It thus seems that the Leiner (2010) routines may be more robust for fitting noisy transits, even if the error found via this method is not believable.

In order to compare TAP with other works, I ran the TAP MCMC on the TrES-1b dataset used by Winn et al. (2007b) and an additional Transit Lightcurve Project dataset, for OGLE-TR-111b (Winn et al. 2007a). In order to achieve the best possible comparison I set TAP to follow as similar a process as possible to that of Winn et al. (2007b). The two MCMCs, however, used different treatments of the limb-darkening penalties—Winn et al. (2007b) only penalized the sum of the two limb darkening parameters, $u_1 + u_2$, whereas TAP penalized each individually. The specific penalties were

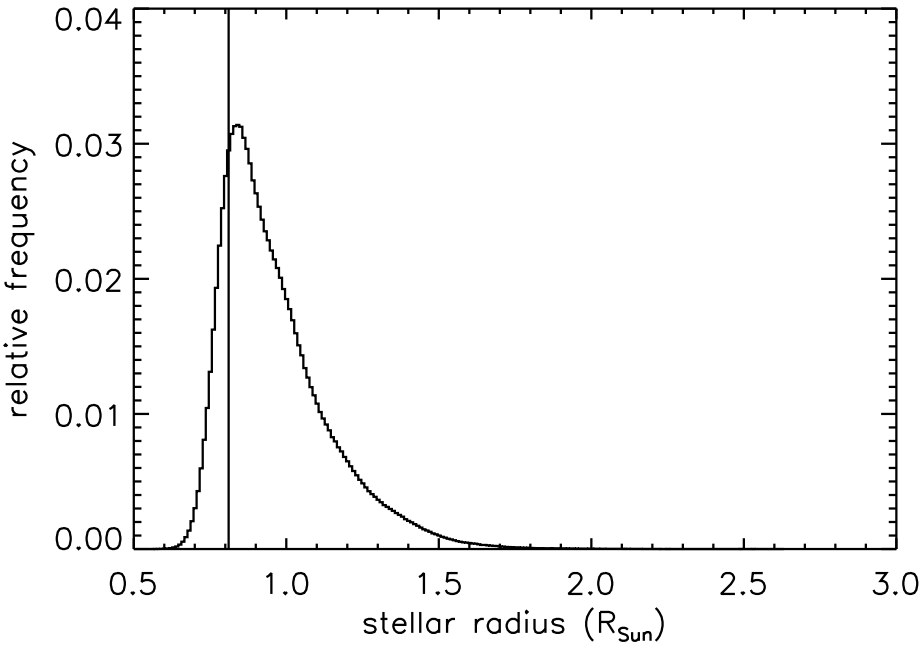

Figure 3.18: The probability distribution of the stellar radius of TrES-1, from our MCMC. The radius found by Winn et al. (2007b) is marked by a vertical line. The distribution is much wider than that from Winn et al. (2007b) shown in Fig. 3.17, as is, indeed, implausibly large, indicating that our MCMC is not working correctly.

$$\left[\frac{(I_1/I_0) - 0.43}{0.086}\right], \frac{I_1}{I_0} = \frac{1}{1 - u_1 - u_2} \tag{3.3}$$

from Winn et al. (2007b) and

$$e^{-(x-x_i)^2/\sigma^2} \tag{3.4}$$

for TAP, where x is the input theoretically-known value of a parameter, x_i is the i^{th} value of that parameter in the chain, and σ is the uncertainty in the theoretical value of the parameter (Gazak et al. 2011). The authors' treatment of the limb darkening is very different for the Winn et al. (2007a) dataset, however; they use a linear limb-darkening law rather than the quadratic law used by the Leiner (2010) routines, TAP, and Winn et al. (2007b). Nonetheless, fitting these data with a quadratic limb-darkening law is instructive for comparison.

Winn et al. (2007b) adopt a 20% uncertainty on the theoretically known values of the limb-darkening parameters, based on the deviations of stars observed via interferometry from the expected limb darkening. I ran two iterations of the TAP MCMC on the Winn et al. (2007b) data, one using a 20% uncertainty in the limb darkening parameters for direct comparison and one using fixed errors of 0.2 for each of the limb-darkening parameters. The results of these tests are presented in Table 3.1. I also used a 20% uncertainty for the OGLE-TR-111b test.

The 20% error run resulted in values and errors very similar to those from Winn et al. (2007b) on the ratio between the planetary and stellar radii, but errors on the limb-darkening parameters that were $\sim 1/2 - 1/3$ those found by Winn et al. (2007b). Most interestingly for this work, however, the errors on the transit centroids found by TAP are $\sim 1.5\times$ as large as those calculated by Winn et al. (2007b). The three transit times calculated by TAP for the TrES-

1b dataset vary from those of Winn et al. (2007b) by 0.17, 0.038, and 0.33 σ, respectively. This again suggests that TAP overestimates the errors on the transit centroid. The transit centroid is rather insensitive to the errors on the limb-darkening parameters; in the 0.2 limb-darkening error run, the transit times and errors varied by ≤ 0.00001 days from those found in the 20% run, much less than the errors. The results from the OGLE-TR-111b run were similar with respect to the Winn et al. (2007a) values, and are also presented in Table 3.1.

3.3.3 Bootstrapping

A bootstrapping analysis was performed in order to better quantify the effect on the results of the systematics in the lightcurves. In order to accomplish this, the best-fit transit lightcurve for each dataset was computed and subtracted from the data. The resulting residual for each n^{th} data point was then assigned to the $(n+1)^{th}$ data point and added back in to the best-fit lightcurve. This synthetic data set was then fit, and the residuals were then added to the $(n+2)^{th}$ data point and refit, and so on. Examples of the distributions of transit centroid values from the bootstrapping analysis are shown in Figs. 3.19 and 3.20. This method has been used extensively for determining the errors in radial velocity planet searches (e.g., Marcy et al. 2005).

In order to determine how robust the errors determined by the bootstrapping method are, we ran the data on the TrES-1b and OGLE-TR-111b datasets of Winn et al. (2007b) and Winn et al. (2007a), respectively. The results of this analysis are presented in Table 3.1 and Fig. 3.21. Our bootstrapping method returns transit centroids that differ from the literature centroids by much less than the error bars of either method, and differs the literature errors by an average of 85%, in all

cases underestimating the errors.

Looking at our own data (see Table 3.2 and Fig. 3.22), for the WASP-33 transit of 2010 December 4 the bootstrapping method finds a significantly larger standard deviation for the transit times than do the other methods, suggesting that for this transit systematic errors are a large problem. For the cleaner transit of 2011 January 23, however, the bootstrapping errors are smaller than those generated by TAP, while still larger than those from the Leiner (2010) routines. For the very noisy WASP-33 transit of 2010 October 16, the bootstrapping routine finds a standard deviation of 0.00868 days, much larger than the errors computed by any other routine. This suggests that systematics are a serious problem for this transit, which can be visually verified by inspecting the lightcurve (see Figs. 4.2 and 4.4). Thus it appears that the bootstrapping method is useful for assessing the degree to which systematics affect the transit lightcurve, but the standard deviations that it returns should not be used directly as an error bar, at least for red noise-dominated transits.

3.3.4 Exoplanet Transit Database

For comparison we also fit our data with the online tools provided by the Exoplanet Transit Database (ETD)[2], as described in Pejcha (2008). This routine uses the Levenberg-Marquardt non-linear least squares fit of Press (1988) and the equations of Mandel & Agol (2002) in order to fit the data; the literature values of the planetary parameters are used as initial guesses for the fit. The transit centroid and duration and the planetary radius are fit while the impact parameter and the limb-darkening coefficient are held fixed (linear limb-darkening is used). In particular, the limb-darkening coefficient is fixed at $c_1 = 0.5$ for all

[2]http://var2.astro.cz/ETD/index.php

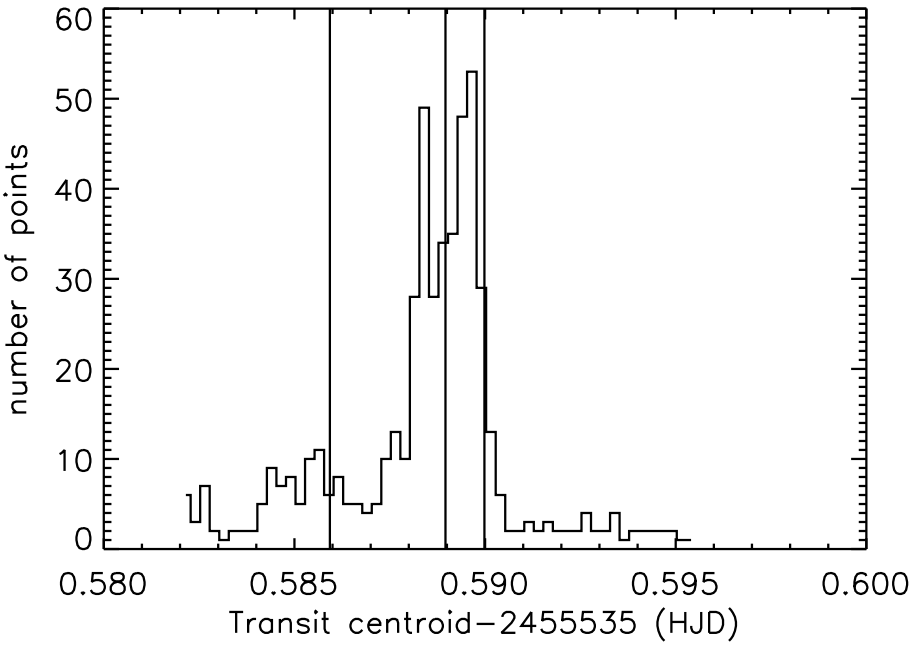

Figure 3.19: Distribution of values of the transit centroid from the bootstrapping analysis of the WASP-33b transit of 2010 December 4. The bin size is 0.00025 days. The center vertical line marks the median of the distribution, whereas the left and right vertical lines mark the 15.9% and 84.1% values of the distribution, respectively.

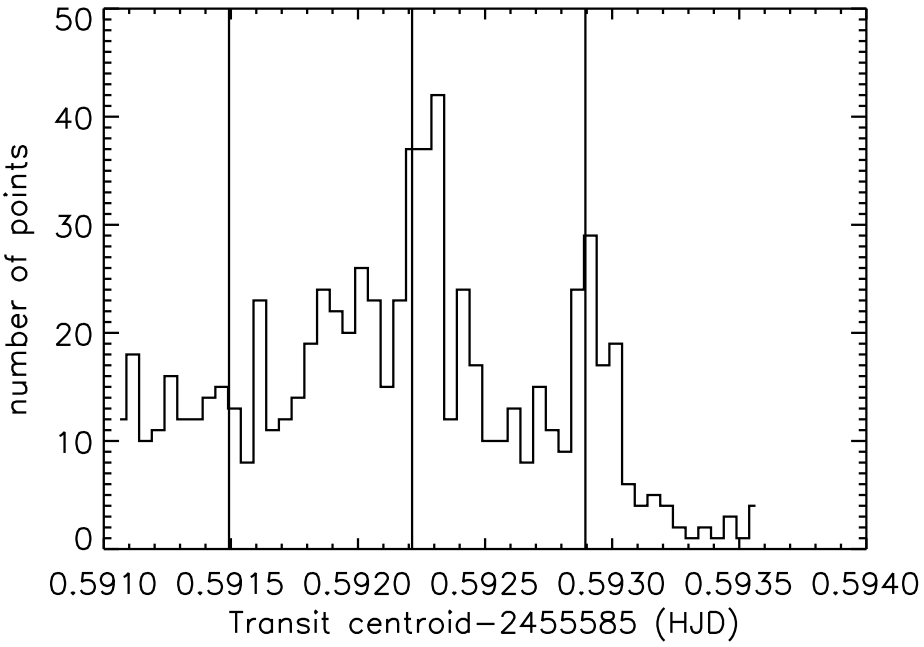

Figure 3.20: Distribution of values of the transit centroid from the bootstrapping analysis of the WASP-33b transit of 2011 January 23. The bin size is 0.00005 days. The center vertical line marks the median of the distribution, whereas the left and right vertical lines mark the 15.9% and 84.1% values of the distribution, respectively.

stars, but they find that the exact value of this parameter has little effect on the other parameters of the fit. Only a relatively small number of iterations of the fitting routine are used, so the results would seem to be possibly not as reliable as more rigorous methods such as an MCMC. Additionally, in computing the errors this routine rescales the photometric error bars to ensure that $\chi^2 = N - g$, where N is the number of data points and g is the number of free parameters. The actual number of degrees of freedom is difficult to evaluate, however, and due to uncertainties in the data the equation $\chi^2 = N - g$ itself has some uncertainty (Andrae et al. 2010). Therefore this is not necessarily a robust method to use, even though such scaling is commonly used throughout the astronomical community. For instance, Winn et al. (2007b) also scale their error bars in this manner. This fitting routine has been used by Maciejewski et al. (2010a) for their data.

In order to test the ETD routine, we ran it on the Winn et al. (2007b) and Winn et al. (2007a) datasets mentioned above. The results of these fits (see Table 3.1) show that ETD is actually *better* at reproducing the errors found by Winn et al. (2007b) and Winn et al. (2007a) than are any of the other fitting methods tested. This suggests that the ETD algorithm does indeed produce robust error bars, at least for relatively clean, high signal-to-noise transits.

ETD seems to not do so well, however, for low signal-to-noise transits. As demonstrated in Fig. 3.22, ETD has problems with such transits, and thus is probably not a good method for fitting our data, which have, on average, relatively high amounts of noise.

3.3.5 Comparison of Fitting and Error Analysis Methods

In order to consider which is the best method of fitting the our data, we fit the publicly-available datasets of Winn et al. (2007b) and Winn et al. (2007a) with four different fitting/error calculation methods: jointly with the Leiner (2010) routines (§3.2); bootstrapping (§3.3.3); TAP (§3.3.2); and the ETD (§3.3.4). The results of this analysis are presented in Table 3.1 and are shown graphically in Fig. 3.21. On average, the errors found by the Leiner (2010) routines are underestimated and differ from those found by Winn et al. (2007b) and Winn et al. (2007a) by 37%; bootstrapping underestimates by 15%; TAP overestimates by 55%; and ETD can either under- or overestimate, and on average differs by 2.7%. ETD differs from the literature values by a maximum of 5.6%. Thus it is obvious that the ETD routines do the best job of finding the errors for these datasets.

In Table 3.2 and Fig. 3.23 we present the results for same analysis carried out on three of our own WASP-33b transits. It is apparent that the calculated errors vary widely from method to method. Indeed, the largest calculated error is that from TAP. This error bar is somewhat too large to be plausible (see Fig. 5.1, and it seems that TAP has some trouble handling even mildly noisy transits such as that of 2010 December 4.

Simply looking at our data, this poses a problem. Which of these error calculation methods is the most accurate? Should we go with the more conservative TAP error bars, but risk having the true errors be overestimated? Or with one of the less conservative methods, but risk underestimating the errors? Or adopt different approaches on a case-by-case basis?

It is obvious from the comparison of the different methods with the MCMCs of Winn et al. (2007b) and Winn et al. (2007a) that the ETD fitting routines come

the closest to replicating their error bars for these five transits. It could also be argued, however, that the TAP MCMC produces appropriately-sized error bars, and Winn et al. (2007b) and Winn et al. (2007a) underestimated *their* errors. It is impossible to determine this for certain with the information that we have available; however, given that in some cases MCMCs tend to overestimate the errors (D. Kipping, personal communication 2011), this seems unlikely.

There is the additional issue that all five of the transits presented by Winn et al. (2007b) and Winn et al. (2007a) are very clean, high signal-to-noise transits, unlike some of ours. This could, in theory, have an effect upon how accurate error bars a given error-computation method finds. In order to investigate this possibility we fit two of our noisiest transits, the WASP-33b transits of 2010 October 10-11 and 17, with several different methods. The data for the first of these transits contains several large gaps due to recentering and refocusing, which unfortunately mean that ingress and egress are not sampled at all. The second transit, meanwhile, was observed through thin, high clouds, resulting in a great deal of noise. The transits can be seen in Figs. 4.2 and 4.4.

Four fitting methods were used: individual and joint fits to all WASP-33b transits with the Leiner (2010) routines, TAP, and ETD. The results are shown in $O-C$ diagram form in Fig. 3.22. Obviously there is a great deal more scatter between the points than there is for the literature data in Fig. 3.21. In particular, the fits to individual transits (those of the Leiner (2010) fits and ETD) tend to be farther from the $O-C=0$ line than those from the joint fits (TAP and Leiner 2010). As both the joint Leiner (2010) fit and TAP return similar values for both transits, it seems that these are likely the most robust fitting methods.

Thus, and in order to be conservative, I have used the TAP error bars and fits in much of the analysis hereafter (Chapter 4). We must recognize, however, that

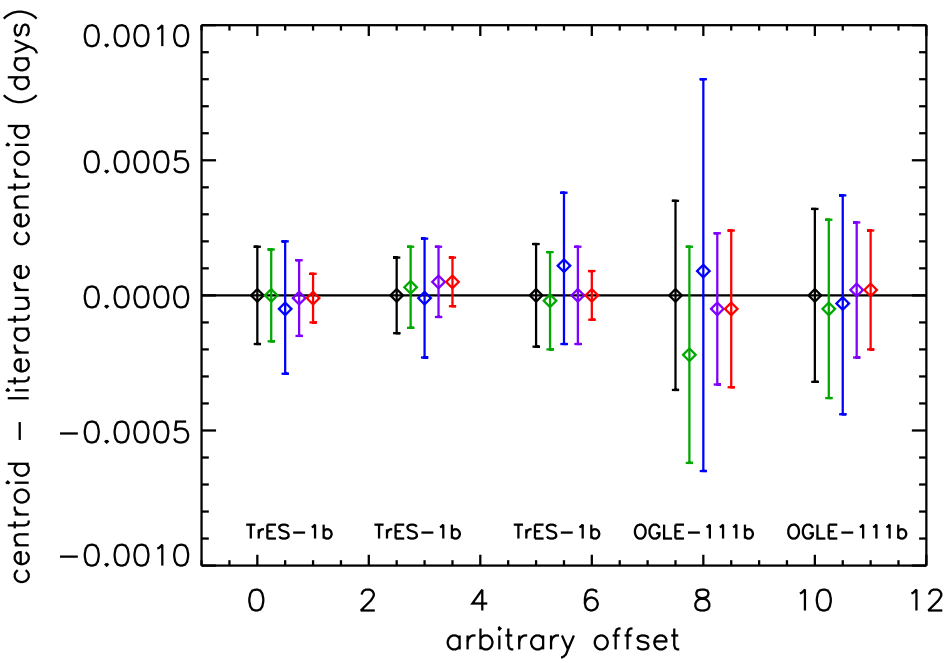

Figure 3.21: The differences between the transit times found by the various methods listed in Table 3.1 and those in the literature are presented in this figure, along with the relevant errors, for each transit. The different methods for each transit are clumped together, and the points have been offset horizontally by an arbitrary amount for clarity. The black points are the literature values (Winn et al. 2007b,a); green, ETD; blue, TAP; purple, bootstrapping; and red, the Leiner (2010) routines. Each set is labeled with the planet, and the data for each planet are in chronological order from left to right.

these are likely to be overestimates, even significant overestimates; this is taken into account in the discussion in Chapter 5.

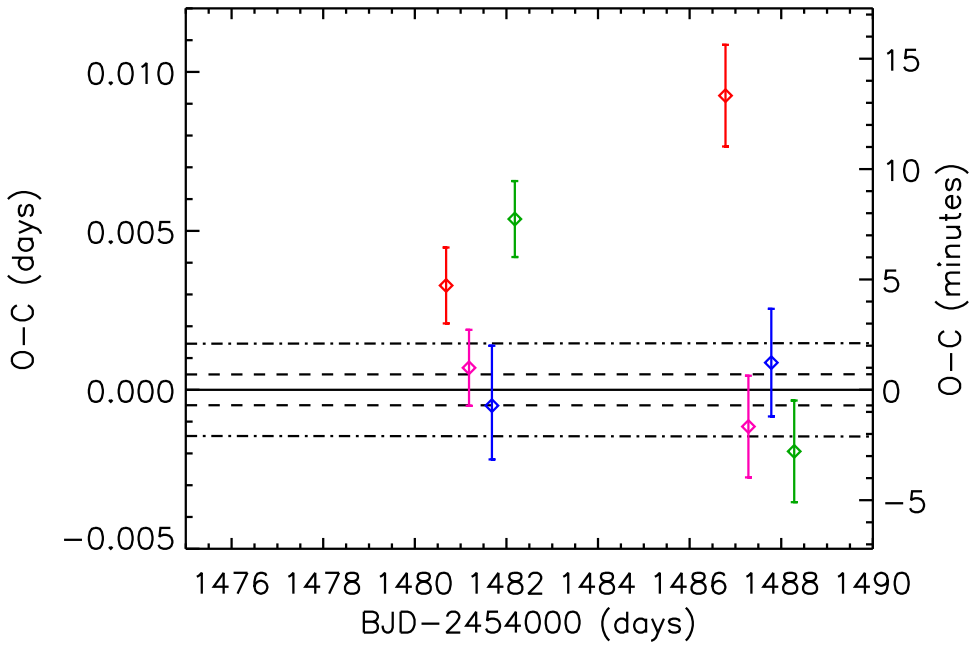

Figure 3.22: Detail of the $O - C$ diagram for WASP-33b (see Figs. 4.5, 4.6, and 4.7, showing the transits of 2010 October 10-11 and October 17. The data points found by four fitting methods are shown: Leiner (2010) fit to the transits individually (red), Leiner (2010) joint fit to all six WASP-33b transits (pink), TAP (blue), and ETD (green). The points for each fitting method have been offset horizontally by an arbitrary amount for clarity. Note the large scatter for these noisy transits, suggesting that systematics are important. The dashed lines show the level of linear TTV that would be caused by a 1σ error in the period, while the dash-dotted lines show that from a 3σ error.

Table 3.1. Comparison of fit parameters and errors for the different fitting methods: transits from the literature. Mid-transit times (HJD-2400000)

Transit	Leiner (2010)	Bootstrapping[a]	TAP	ETD	Original Reference
TrES-1b	53895.84298 ± 0.00009	53895.84298 ± 0.00014	$53895.84302^{+0.00025}_{-0.00024}$	53895.84297 ± 0.00017	53895.84297 ± 0.00018
TrES-1b	53898.87336 ± 0.00009	53898.87336 ± 0.00013	53898.87342 ± 0.00022	53898.87338 ± 0.00015	53898.87341 ± 0.00014
TrES-1b	53901.90372 ± 0.00009	53901.90372 ± 0.00018	$53901.90361^{+0.00027}_{-0.00029}$	53901.90374 ± 0.00018	53901.90372 ± 0.00019
OGLE-TR-111b	53787.70859 ± 0.00029	53787.70859 ± 0.00028	$53787.70845^{+0.00071}_{-0.00074}$	53787.70876 ± 0.00040	53787.70854 ± 0.00035
OGLE-TR-111b	53799.75136 ± 0.00022	53799.75136 ± 0.00025	$53799.75141^{+0.00040}_{-0.00041}$	53799.75143 ± 0.00033	53799.75138 ± 0.00032

Note. — These data are presented graphically in Fig. 3.21.

[a]The bootstrapping routine was run on the residuals to the joint fit for each transit individually, as running the routine over all combinations of errors for the three transits jointly would have required fitting the light curves $\sim 5.6 \times 10^7$ times. As each joint fit to the three light curves takes $\sim 1 - 2$ minutes, this is not computationally feasible.

Table 3.2. Comparison of fit parameters and errors for the different fitting methods: mid-transit times (HJD-2400000)

Transit and Date	Transit Quality	Leiner (2010)	Bootstrapping	TAP	ETD
WASP-33b, Oct. 17	very noisy	55486.78103 ± 0.00114	55486.79159 ± 0.00868	55486.7823 ± 0.0016	55486.78041 ± 0.00150
WASP-33b, Dec. 4	noisy	55535.58850 ± 0[a]	$55535.58896^{+0.00102}_{-0.00303}$	$55535.5850^{+0.0120}_{-0.0041}$	55535.58625 ± 0.00059
WASP-33b, Jan. 23	clean	55585.59221 ± 0[a]	$55585.59221^{+0.00068}_{-0.00072}$	55585.59270 ± 0.00099	55585.59235 ± 0.00040

Note. — These data are presented graphically in Fig. 3.23.

[a]The Leiner (2010) error calculation routine fails to find a minimum χ^2 value for some datasets, making the determination of error bars using this method impossible.

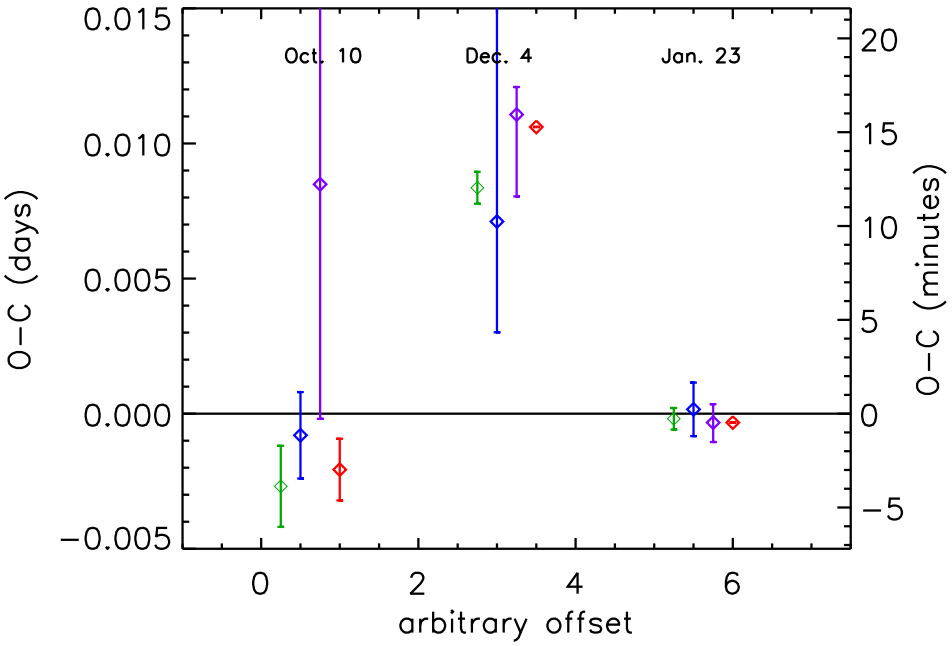

Figure 3.23: The transit timing variations as found by four different fitting methods for three transits of WASP-33b of varying quality. The different methods for each transit are clumped together, and the points have been offset horizontally by an arbitrary amount for clarity. The green points are the values found by ETD; blue, TAP; purple, bootstrapping; and red, the Leiner (2010) routines from a joint fit to all WASP-33b transits. The Leiner (2010) routines failed to find a minimum χ^2 and thus returned no error for the Dec. 4 and Jan. 23 transits. Each set is labeled with the date. These data are presented in Table 3.2.

Chapter 4

Results

4.1 Transit Lightcurves

Our reduced, best-fit transit lightcurves are presented in Figs. 4.1, 4.2, and 4.3. All lightcurves shown in this chapter were fit with the Leiner (2010) routines. These plots show each transit fit individually. For systems where multiple planets were observed we also fit the transits simultaneously; these fits are shown later in this chapter. Additionally, we compile observed minus calculated ($O-C$) diagrams for our systems in order to investigate any TTVs. These diagrams simply show the difference between the observed and expected (calculated) transit centroids as a function of time. An error in the period of a planet would result in a linear trend in an $O-C$ diagram, while the presence of a perturbing planet resulting in TTVs (see §1.2.1) would manifest as a periodic or quasi-periodic trend in the $O-C$ diagram.

In order to properly compute $O-C$ diagrams and otherwise compare transit times it is critical that all of the transit times use the same time standard. In the exoplanet community at present there seems to be no agreement as to a common time standard, with both the Heliocentric Julian Date (HJD) and Barycentric Julian Date (BJD) systems enjoying roughly equal popularity. Although all of the transit times quoted in this work are listed in HJD, we compile the $O-C$

diagrams using BJD. Conversion from HJD to BJD is accomplished using the hjd2bjd IDL code of Eastman et al. (2010).

4.2 WASP-33b

Six transits of WASP-33b were observed (Table 2.6). Lightcurves for these transits, fit individually, are shown in Figs. 4.1, 4.2 and 4.3. The jointly fit lightcurves are shown in Fig. 4.4.

Like all of our systems, we calculate $O-C$ diagrams to search for transit timing variations. Such diagrams are shown in Figs. 4.5 and 4.6. Taken together with data from Herrero et al. (2011), our observations of WASP-33b suggest evidence for nonlinear transit timing variations, although only one VVO datapoint deviates from the $O - C = 0$ line by much greater than 1σ. The presented error bars for the VVO data, however, are from the TAP MCMC, and, as argued in §3.3.5, the errors from TAP should be regarded as conservative upper limits. As a comparison the TTVs derived from the Leiner (2010) and ETD fitting routines are shown in Fig. 4.7. The transit centroids and $O - C$ values computed by the two different methods are listed in Table 4.1.

In order to investigate the possibility of periodic TTVs, we construct a Lomb-Scargle periodogram (Scargle 1982; Horne & Baliunas 1986) from the TTVs in Fig. 4.5. This periodogram is presented in Fig. 4.8. The strongest peak has a period of 14.1739 days; however, this peak has a low power spectral density, indicating that it is not particularly significant. Furthermore, the data are significantly under-Nyquist sampled, as defined in Horne & Baliunas (1986); the minimum period which is Nyquist-sampled is ∼239 days, considering all of the data, and ∼36 days, considering only the data from VVO and (Herrero et al. 2011). This reduces

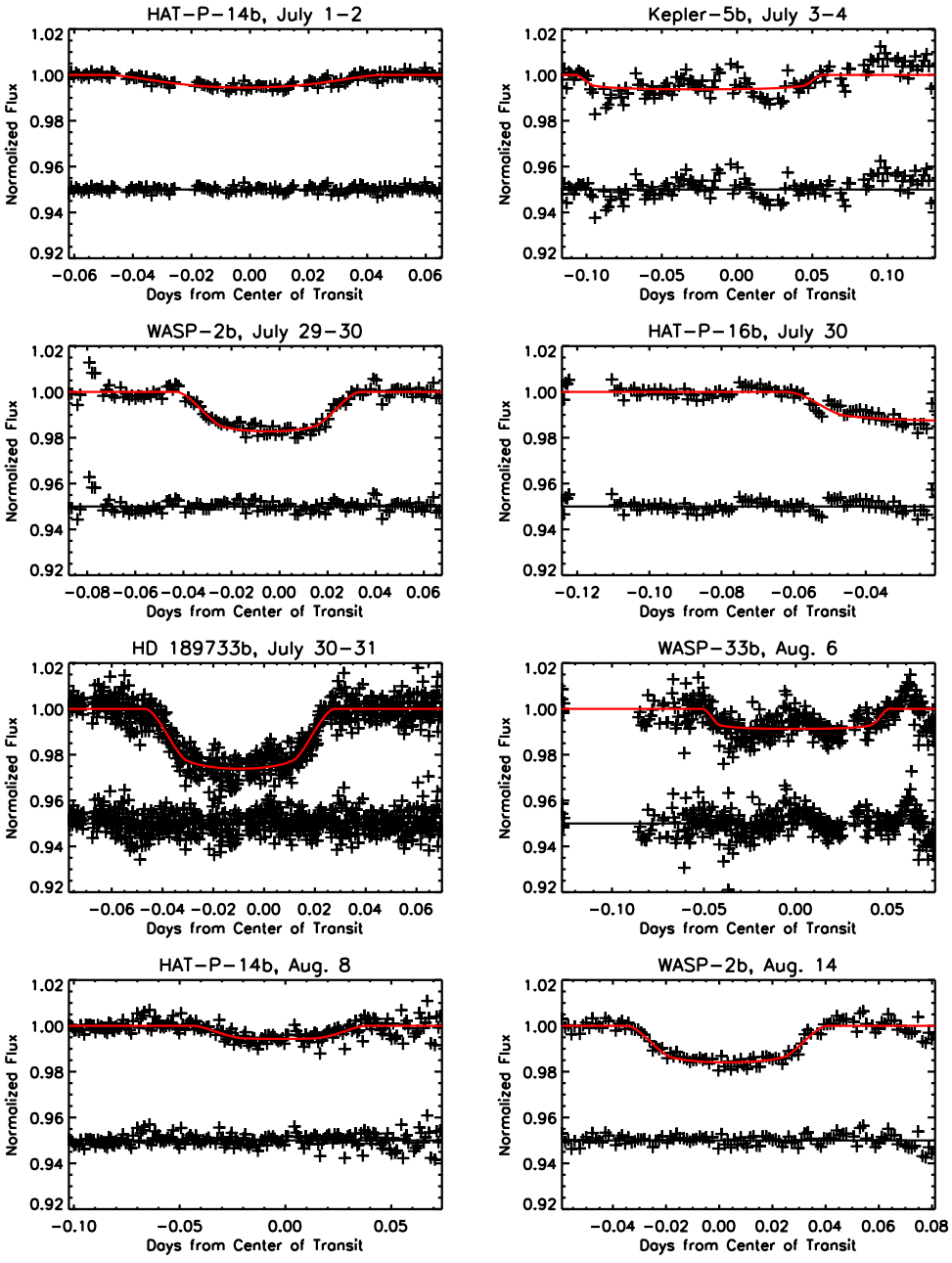

Figure 4.1: Fitted lightcurves of transits observed during the 2010-2011 observing season. All transits have been fitted individually using the Leiner (2010) routines. Note the varying transit depths, noise levels, and sampling frequencies.

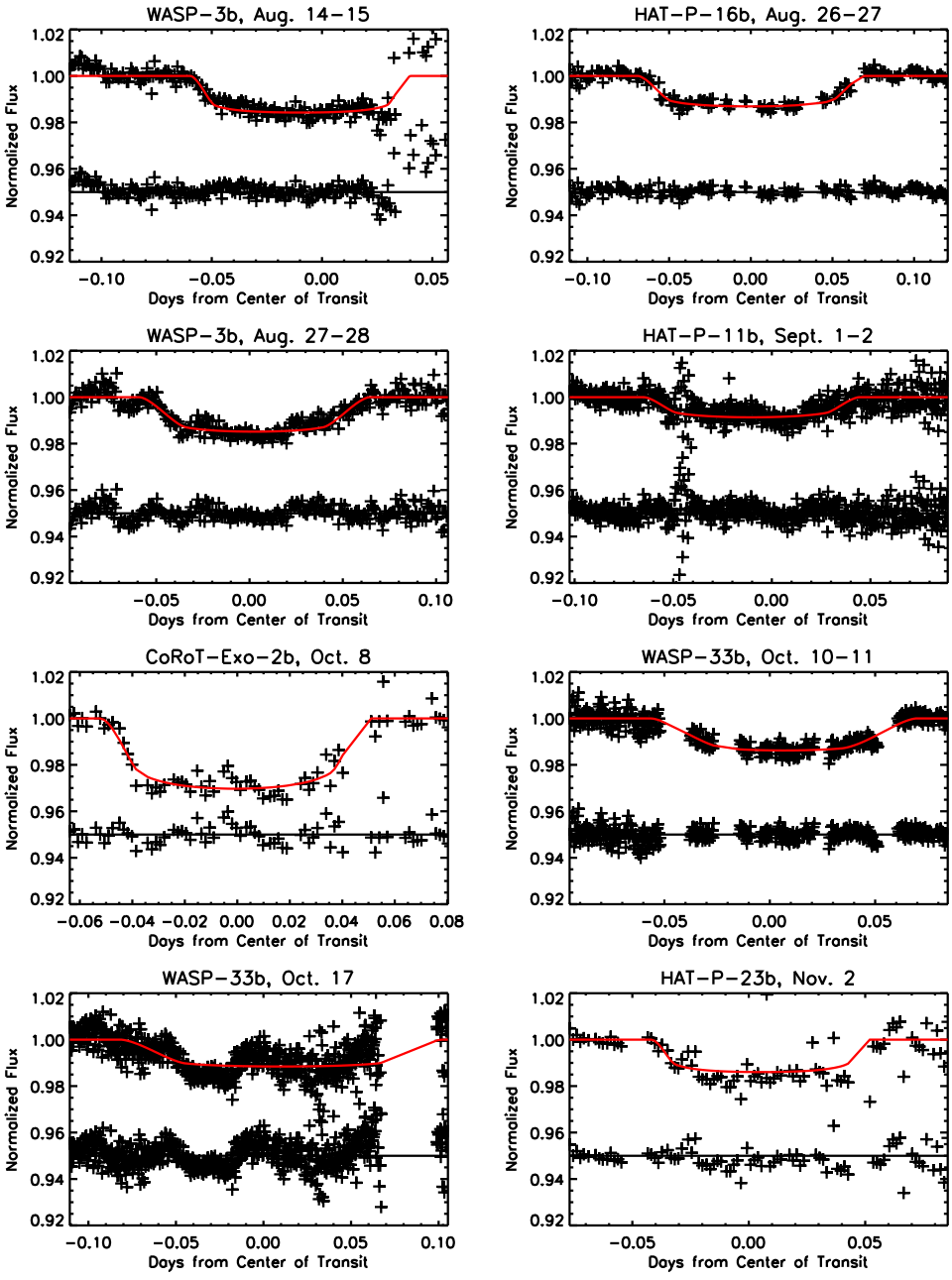

Figure 4.2: Fitted lightcurves of transits observed during the 2010-2011 observing season. All transits have been fitted individually using the Leiner (2010) routines. Note the varying transit depths, noise levels, and sampling frequencies.

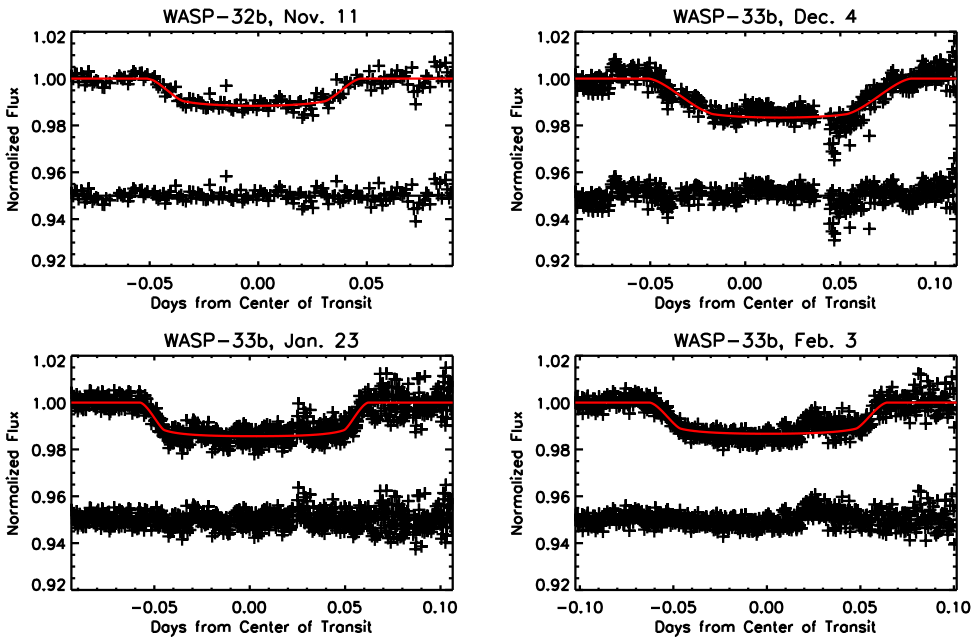

Figure 4.3: Fitted lightcurves of transits observed during the 2010-2011 observing season. All transits have been fitted individually using the Leiner (2010) routines. Note the varying transit depths, noise levels, and sampling frequencies.

even further the significance of this peak. Nonetheless, the data are presented in Fig. 4.9 when phased with this period. While there does appear to be a periodic trend visible in the data, when amateur transit observations from the Exoplanet Transit Database are included no such trend is visible with this period. As the errors on these points are estimated using the ETD fitting routines, which as we have seen tend to do a poor job on noisy transits, these transit times are likely not particularly reliable.

4.3 Other Systems

The transit centroids for other systems are presented in Table 4.2.

4.3.1 WASP-3b

WASP-3b was suggested by Maciejewski et al. (2010a) to show periodic transit timing variations; we therefore observed two transits of this planet to investigate this possibility. The jointly fit transit lightcurves are shown in Fig. 4.10. The TTVs are shown in Fig. 4.11, while they are phased with the period found by Maciejewski et al. (2010a) in Fig. 4.12. Our data alone are consistent with the periodic trend found by Maciejewski et al. (2010a). However, since the publication of that work, Christiansen et al. (2011) presented observations of six WASP-3b transits obtained using the ex-*Deep Impact* spacecraft under NASA's *EPOXI* mission. These data do not fit with the TTVs proposed by Maciejewski et al. (2010a), but are still not consistent with zero TTVs.

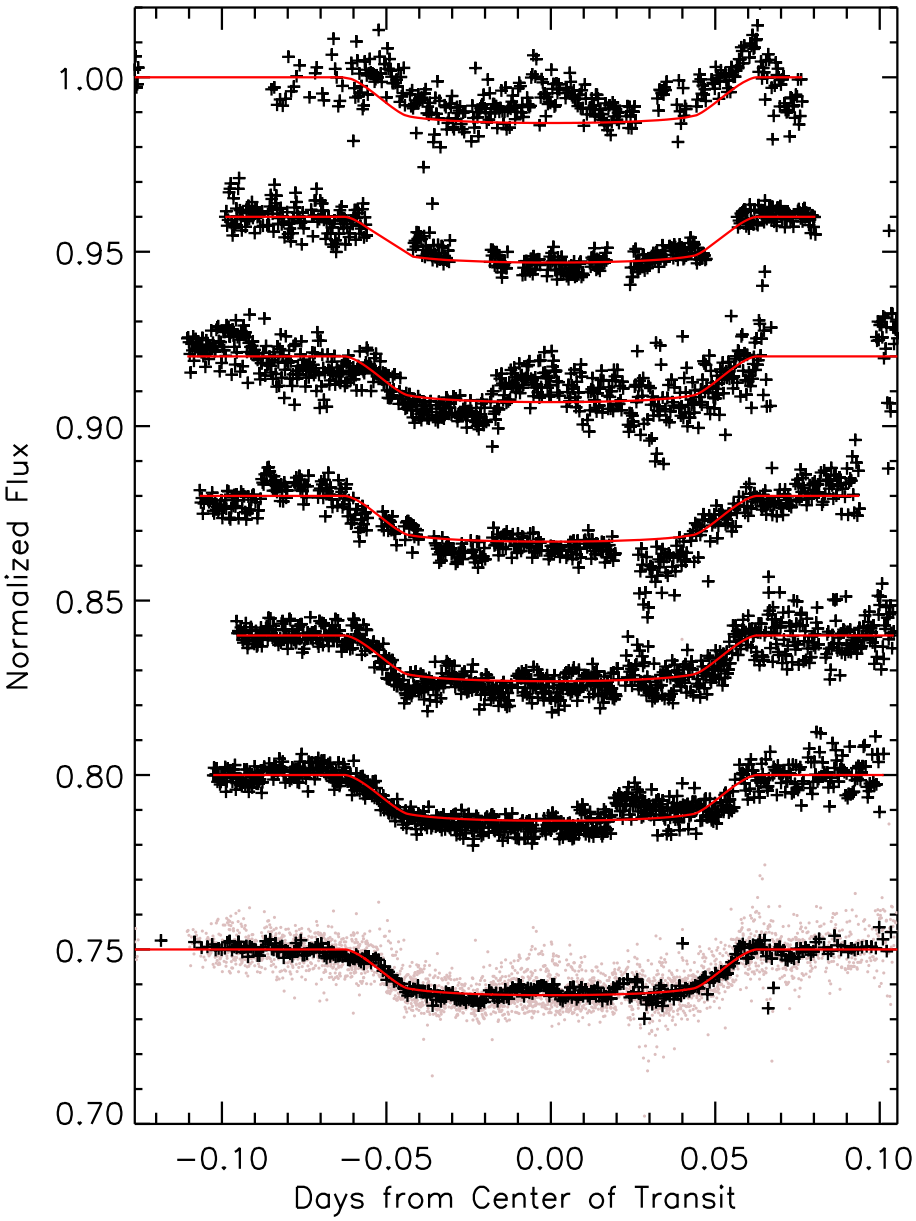

Figure 4.4: Jointly fitted lightcurves of the six observed transits of WASP-33b. Individual transits have been offset vertically for clarity. Top to bottom: transits of August 6, October 10-11, October 17, December 4, January 23, February 3, and the combined lightcurve of the six transits. For the combined curve all data points are shown in gray, while the black points show the data after binning each 10 data points. Error bars are not shown for clarity.

Table 4.1. Transit centroids for WASP-33b

Date	TAP Center (HJD)	TAP $O-C$ (d)	Leiner (2010) Center (HJD)[a]	Leiner (2010) $O-C$ (d)
Aug. 6	$2455414.8077^{+0.0040}_{-0.0074}$	$-0.0023^{+0.0040}_{-0.0074}$	2455414.80317 ± 0.00160	-0.00147 ± 0.00169
Oct. 10-11	$2455480.6825^{+0.0018}_{-0.0016}$	$-0.0005^{+0.0019}_{-0.0017}$	2455480.68628 ± 0.00112	0.00387 ± 0.00125
Oct. 17	$2455486.7823^{+0.0016}_{-0.0016}$	$-0.0001^{+0.0017}_{-0.0017}$	2455486.78103 ± 0.00114	0.00132 ± 0.00127
Dec. 4	$2455535.5850^{+0.0120}_{-0.0041}$	$0.0079^{+0.0120}_{-0.0041}$	2455535.58560 ± 0.00054	0.01199 ± 0.00078
Jan. 23	$2455585.5929^{+0.0011}_{-0.0011}$	$0.0011^{+0.0012}_{-0.0012}$	2455585.59217 ± 0.00040	-0.00003 ± 0.00071
Feb. 3	$2455596.5720^{+0.0011}_{-0.0010}$	$0.0012^{+0.0012}_{-0.0012}$	2455596.57107 ± 0.00045	-0.00004 ± 0.00074

Note. — The columns labeled TAP are the relevant values as fit to the transits by TAP. The TAP fits to the transits of Oct. 10-11, Dec. 4, Jan. 23, and Feb. 3 are from a joint fit; the transits of Aug. 6 and Oct. 17 were fit individually due to their noisy nature. The transits were all fit jointly by the Leiner (2010) routines.

[a]For transits where the Leiner (2010) routines fail to find a minimum χ^2 and therefore an error on the transit centroid the corresponding errors from ETD have been substituted. This is for demonstrative purposes only.

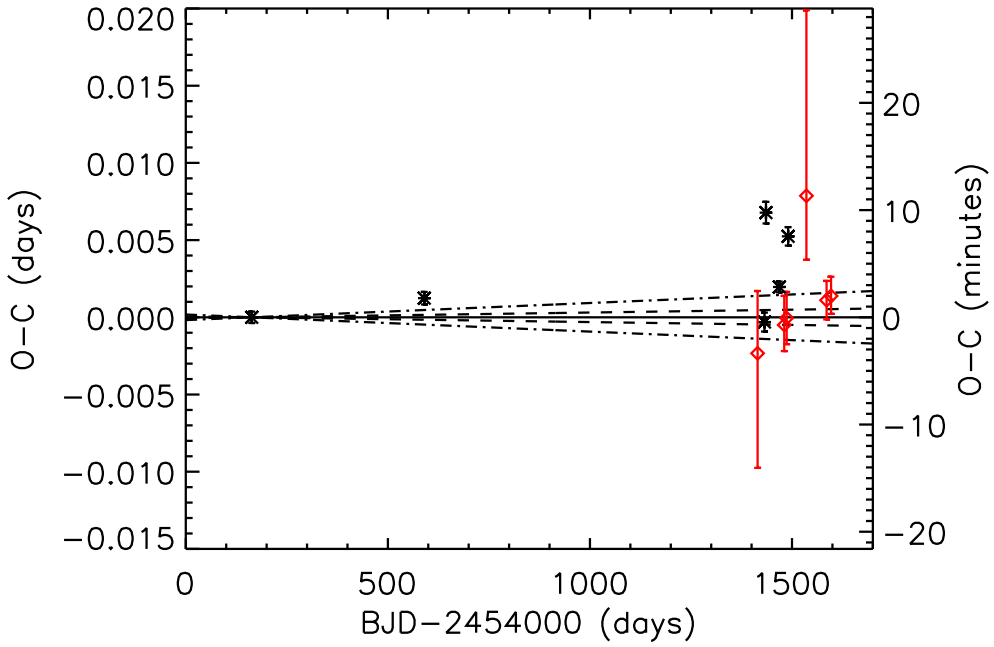

Figure 4.5: $O - C$ diagram for WASP-33b, with data from the literature (Collier Cameron et al. 2010; Smith et al. 2011; Herrero et al. 2011) in black and the VVO observations in red. Transit times and errors are those calculated by TAP, and the period is that from Collier Cameron et al. (2010). The dashed lines show the level of linear TTVs that would be caused by a 1σ error in the period, while the dash-dotted lines show that from a 3σ error.

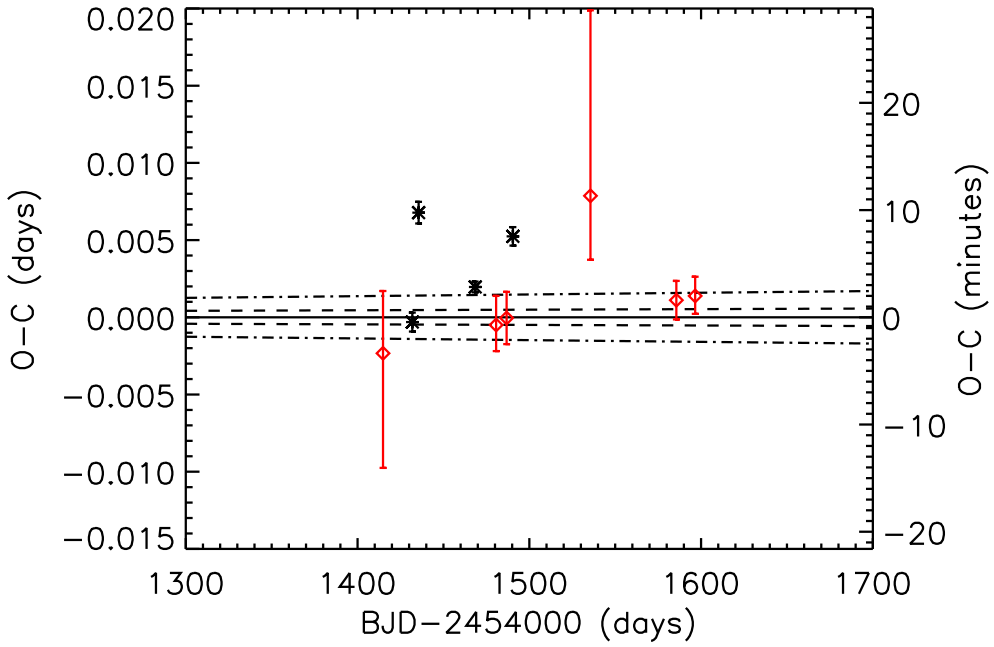

Figure 4.6: $O - C$ diagram for WASP-33b, showing only the portion of Fig. 4.5 with VVO transits. Data from the literature (Herrero et al. 2011) are in black and the VVO observations are in red. Transit times and errors are those calculated by TAP, and the period is that from Collier Cameron et al. (2010). The dashed lines show the level of linear TTVs that would be caused by a 1σ error in the period, while the dash-dotted lines show that from a 3σ error.

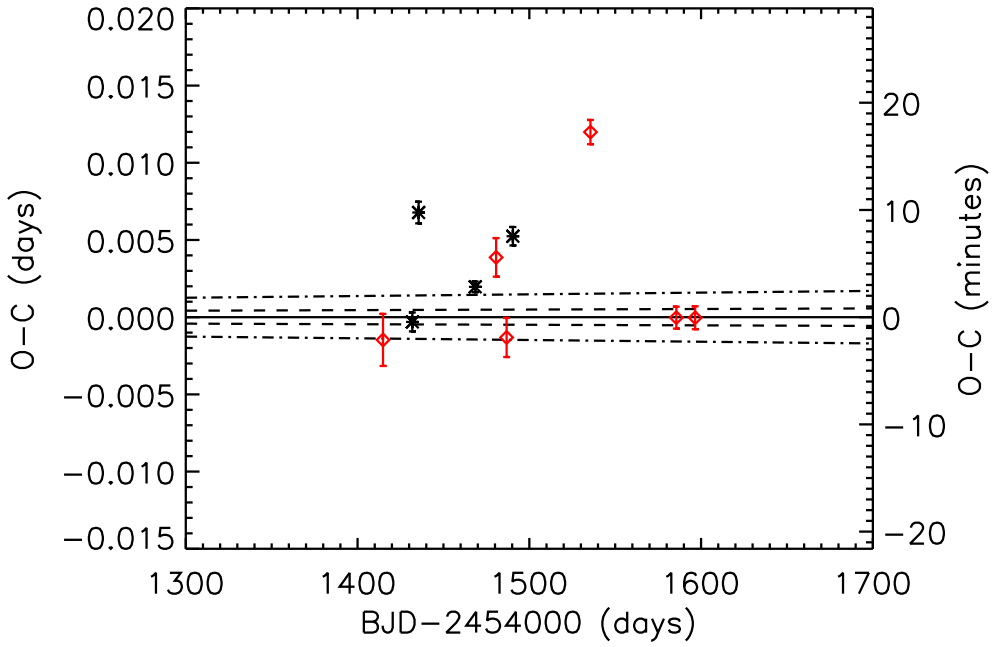

Figure 4.7: $O - C$ diagram for WASP-33b, showing only the portion of Fig. 4.5 with VVO transits. Data from the literature (Herrero et al. 2011) are in black and the VVO observations are in red. Transit times and errors are those calculated by the Leiner (2010) routines, with errors from Leiner (2010) and ETD, using the joint fit to the data. The ETD errors are substituted for the Leiner (2010) errors for cases where the latter routine fails to find an error. The period is that from Collier Cameron et al. (2010). The dashed lines show the level of linear TTVs that would be caused by a 1σ error in the period, while the dash-dotted lines show that from a 3σ error.

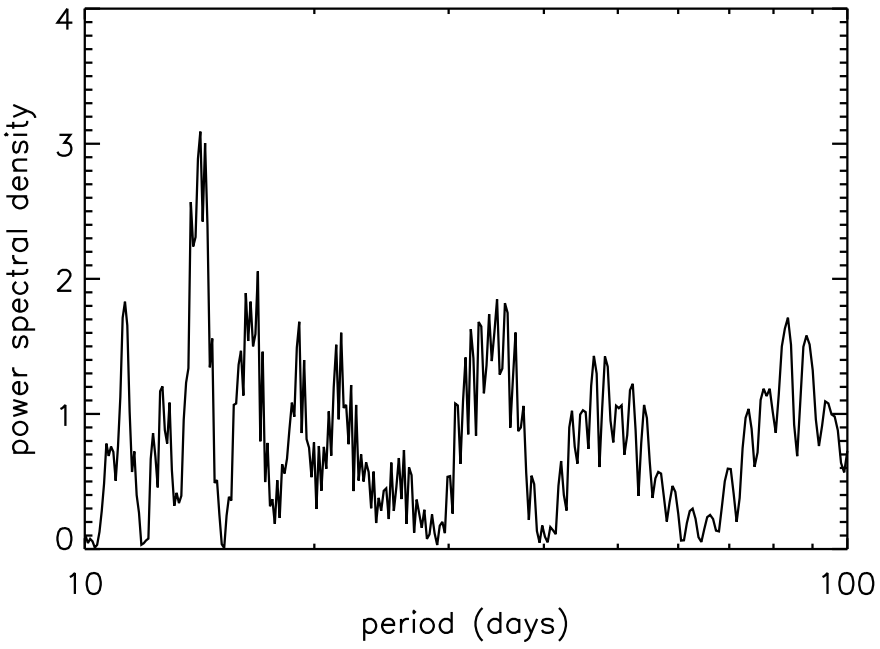

Figure 4.8: Lomb-Scargle periodogram for TTVs of WASP-33b calculated from the data in Fig. 4.5. The peak with the greatest power spectral density and a period of > 10 days has a period of 14.1739 days. The power spectral density is related to the significance of a given period; values in the range shown here are not significant.

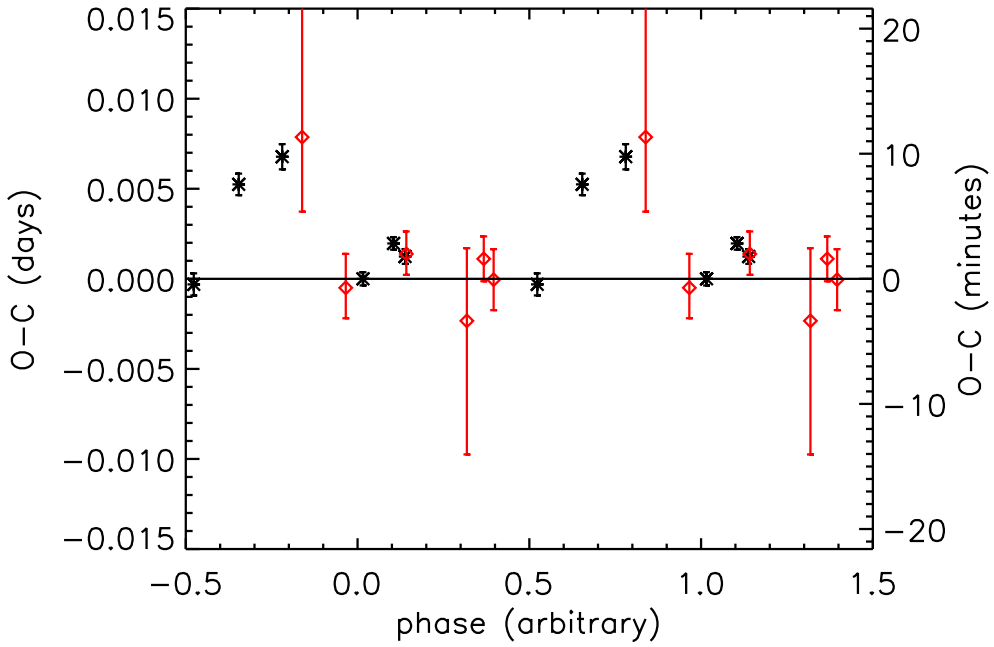

Figure 4.9: TTVs of WASP-33b phased with the 14.1739 period shown in Fig. 4.8. The phase is arbitrary, and the points are duplicated across two full periods for clarity. The data from the literature (Collier Cameron et al. 2010; Smith et al. 2011; Herrero et al. 2011) are in black and the VVO observations are in red.

Table 4.2. Transit centroids for observed systems from individual fits

Name	Date	TAP Center (HJD)	TAP $O-C$ (d)	Leiner (2010) Center (HJD)[a]	Leiner (2010) $O-C$ (d)
HAT-P-14b	July 1	$2455379.70560^{+0.00160}_{-0.00150}$	$0.00237^{+0.00175}_{-0.00166}$	$2455379.70549 \pm 0.00173$	0.00226 ± 0.00187
WASP-2b	July 29	$2455407.67480^{+0.00240}_{-0.00210}$	$-0.00146^{+0.00241}_{-0.00211}$	2455407.67507 ± 0	-0.00119 ± 0.00017
HAT-P-16b	July 29	$2455407.90000^{+0.03200}_{-0.00480}$	$0.00130^{+0.03200}_{-0.00483}$	2455407.90016 ± 0	0.00146 ± 0.00051
HD 189733b	July 30-31	$2455408.69030^{+0.00076}_{-0.00075}$	$0.00014^{+0.00090}_{-0.00060}$	2455408.68966 ± 0	-0.00050 ± 0.00026
HAT-P-14b	Aug. 7	$2455416.72690^{+0.00570}_{-0.00500}$	$0.00242^{+0.00575}_{-0.00506}$	$2455416.72777 \pm 0.00095$	0.00329 ± 0.00121
WASP-2b	Aug. 14	$2455422.74080^{+0.00190}_{-0.00180}$	$-0.00101^{+0.00191}_{-0.00181}$	$2455422.74126^{+0.00019}_{-0.00025}$	$-0.00055^{+0.00026}_{-0.00030}$
WASP-3b	Aug. 14-15	$2455423.70668 \pm 0.00072$	-0.00007 ± 0.00272	$2455423.70774 \pm 0.00024$	0.00037 ± 0.00041
HAT-P-16b	Aug. 26-27	$2455435.66080^{+0.00140}_{-0.00130}$	$0.00250^{+0.00150}_{-0.00141}$	$2455435.66026 \pm 0.00067$	0.00196 ± 0.00086
WASP-3b	Aug. 27-28	$2455436.63209 \pm 0.00062$	$-0.00112^{+0.00153}_{-0.00173}$	$2455436.63154 \pm 0.00040$	-0.00368 ± 0.00052
HAT-P-11b	Sept. 1-2	$2455441.69980 \pm 0.00480$	-0.00515 ± 0.00486	$2455441.70069^{+0.00009}_{-0.00018}$	$-0.00426^{+0.00075}_{-0.00076}$
CoRoT-Exo-2b	Oct. 8	$2455478.55070^{+0.00180}_{-0.00220}$	$0.00239^{+0.00217}_{-0.00251}$	2455478.54999 ± 0	0.00168 ± 0.00122
HAT-P-23b	Nov. 2	$2455503.58610^{+0.00380}_{-0.00340}$	$0.00350^{+0.00395}_{-0.00357}$	$2455503.58337^{+0.00016}_{-0}$	$0.00077^{+0.00110}_{-0.00109}$
WASP-32b	Nov. 11	$2455512.63800 \pm 0.00240$	0.00295 ± 0.00267	$2455512.63880^{+0.00160}_{-0.00109}$	$0.00375^{+0.00160}_{-0.00199}$

Note. — See Table 4.1 for the transit centroids for WASP-33b.

[a]The Leiner (2010) error-calculation routine sometimes fails to find a minimum χ^2 value; in these cases the error has been reported as zero even though this obviously cannot be the case.

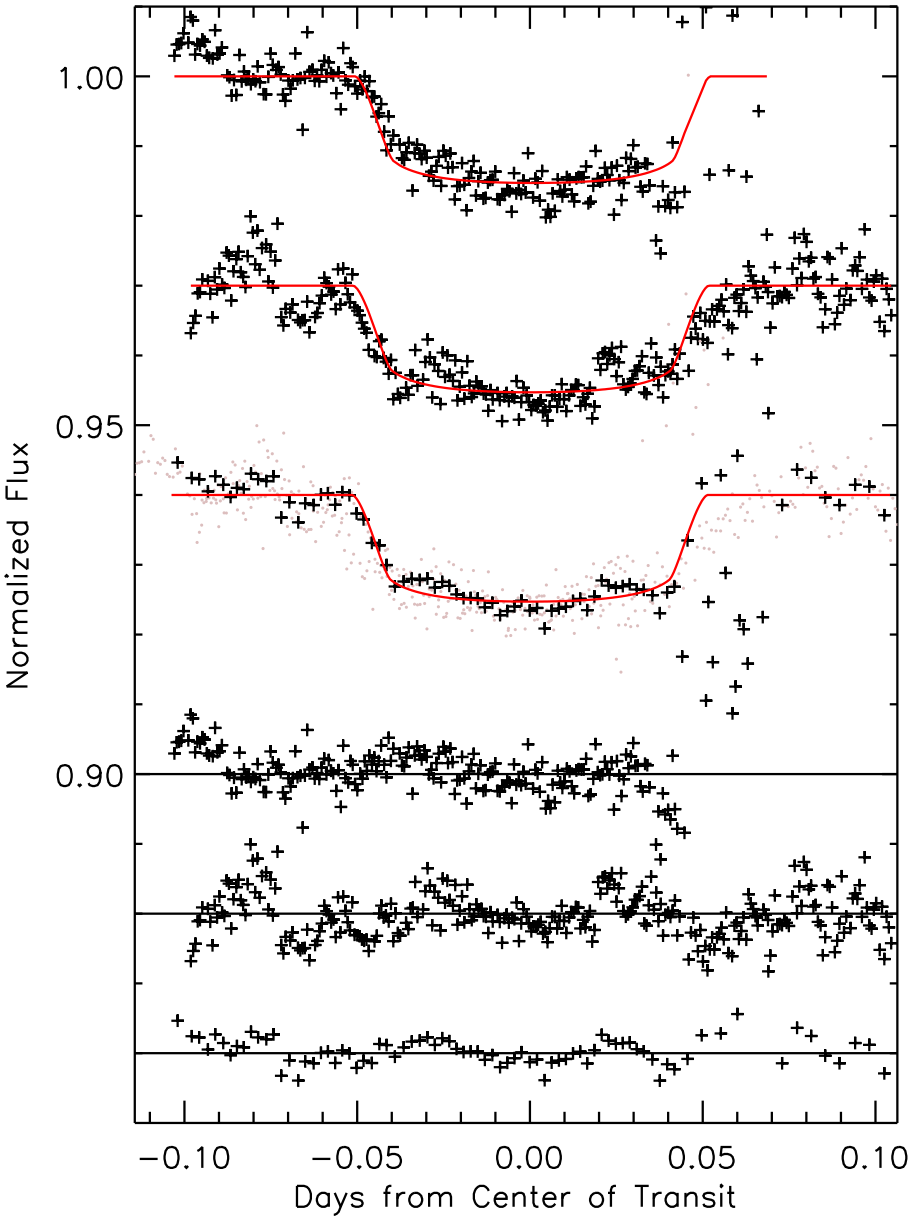

Figure 4.10: Jointly fitted lightcurves of the two observed transits of WASP-3b. Individual transits have been offset vertically for clarity. Top to bottom: transits of August 14-15, August 27-28, and the combined lightcurve of the two transits. For the combined curve all data points are shown in gray, while the black points show the data after binning each 6 data points. Error bars are not shown for clarity.

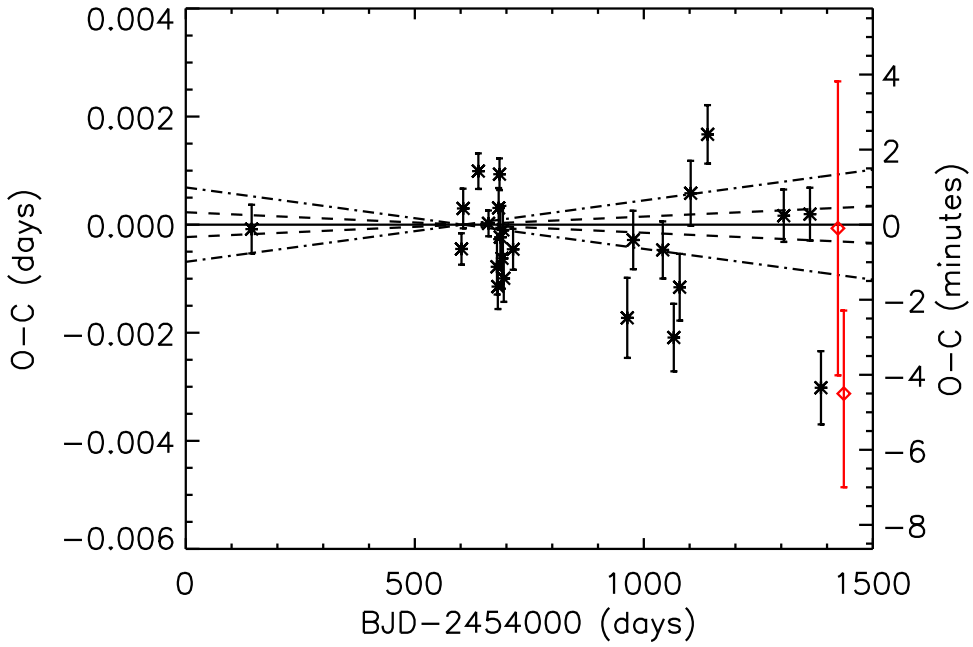

Figure 4.11: $O - C$ diagram for WASP-3b, with data from the literature (Pollacco et al. 2008; Tripathi et al. 2010; Gibson et al. 2008; Christiansen et al. 2011; Maciejewski et al. 2010a) in black and the VVO observations in red. Transit times and errors are those calculated by TAP. The dashed lines show the level of linear TTVs that would be caused by a 1σ error in the period, while the dash-dotted lines show that from a 3σ error. Compare to Fig. 2 of Maciejewski et al. (2010a) (presented here as Fig. 1.9).

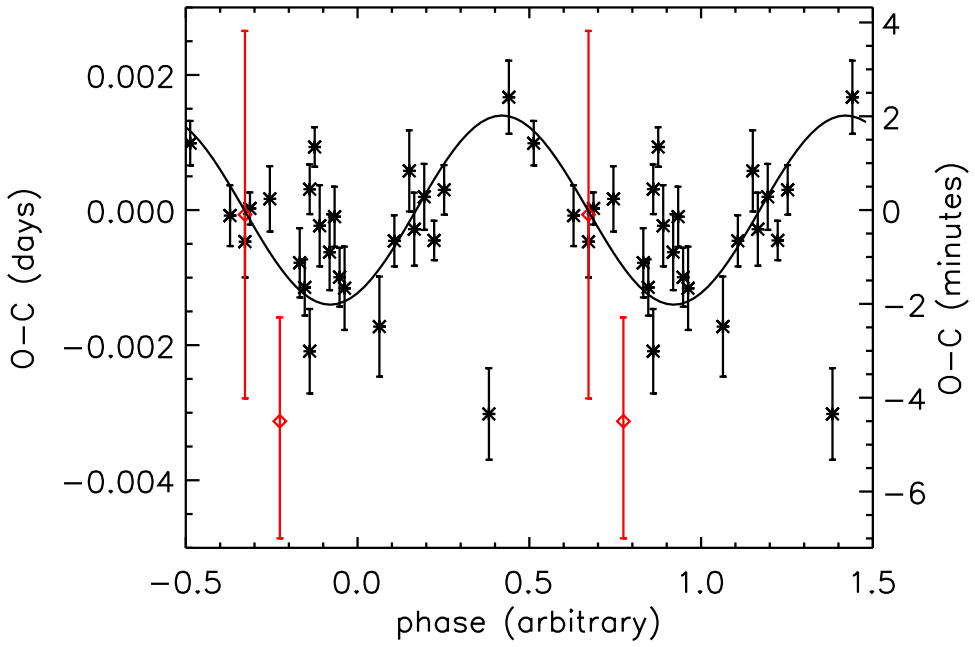

Figure 4.12: TTVs of WASP-3b phased with the period of ∼129 days (∼69 times the orbital period of WASP-3b), with a sinusoidal trend superposed for comparison, following Maciejewski et al. (2010a). The phase is arbitrary, and the points are duplicated across two full periods for clarity. Data from the literature (Pollacco et al. 2008; Tripathi et al. 2010; Gibson et al. 2008; Christiansen et al. 2011; Maciejewski et al. 2010a) is in black and the VVO observations are in red. Compare to Fig. 3.b. of Maciejewski et al. (2010a) (presented here as Fig. 1.10).

4.3.2 HAT-P-16b

One full and one partial transit of HAT-P-16b were observed, as shown in Fig. 4.13; the partial transit was cut off by sunrise. The $O-C$ diagram for HAT-P-16b is shown in Fig. 4.14. While the three literature points (Buchhave et al. 2010) all lie along the $O-C=0$ line, the one reliable VVO data point lies above this line with a significance of $\sim 1.8\sigma$. This could in theory be due to a nonlinear TTV; however, no conclusions can be drawn from only one deviant data point. More observations of this system are thus warranted.

4.3.3 HAT-P-14b

The orbit of HAT-P-14b has a relatively high inclination, resulting in nearly grazing transits and a shallow slope during ingress and egress; the transits are additionally rather shallow. This makes the determination of the exact time of first and fourth contact, and thus the transit centroid, difficult to determine; unfortunately this results in a larger error on the transit centroid than one would expect from the quality of the photometry. The jointly fit lightcurves are presented in Fig. 4.15.

The $O-C$ diagram for HAT-P-14b is presented in Fig. 4.16. It is obvious that there is a linear trend in the data points, indicating that the original period calculated by Torres et al. (2010) is not precisely correct. We fit a linear trend to the data, as shown in Fig. 4.16, from which we calculate a new period of 4.627696 ± 0.000012 days. Our period is 2.1σ away from that of Torres et al. (2010), and 1.1σ away from that of Nascimbeni et al. (2011). Unfortunately due to the large error bars on our points, our period actually has a larger error than those of Torres et al. (2010) or Nascimbeni et al. (2011).

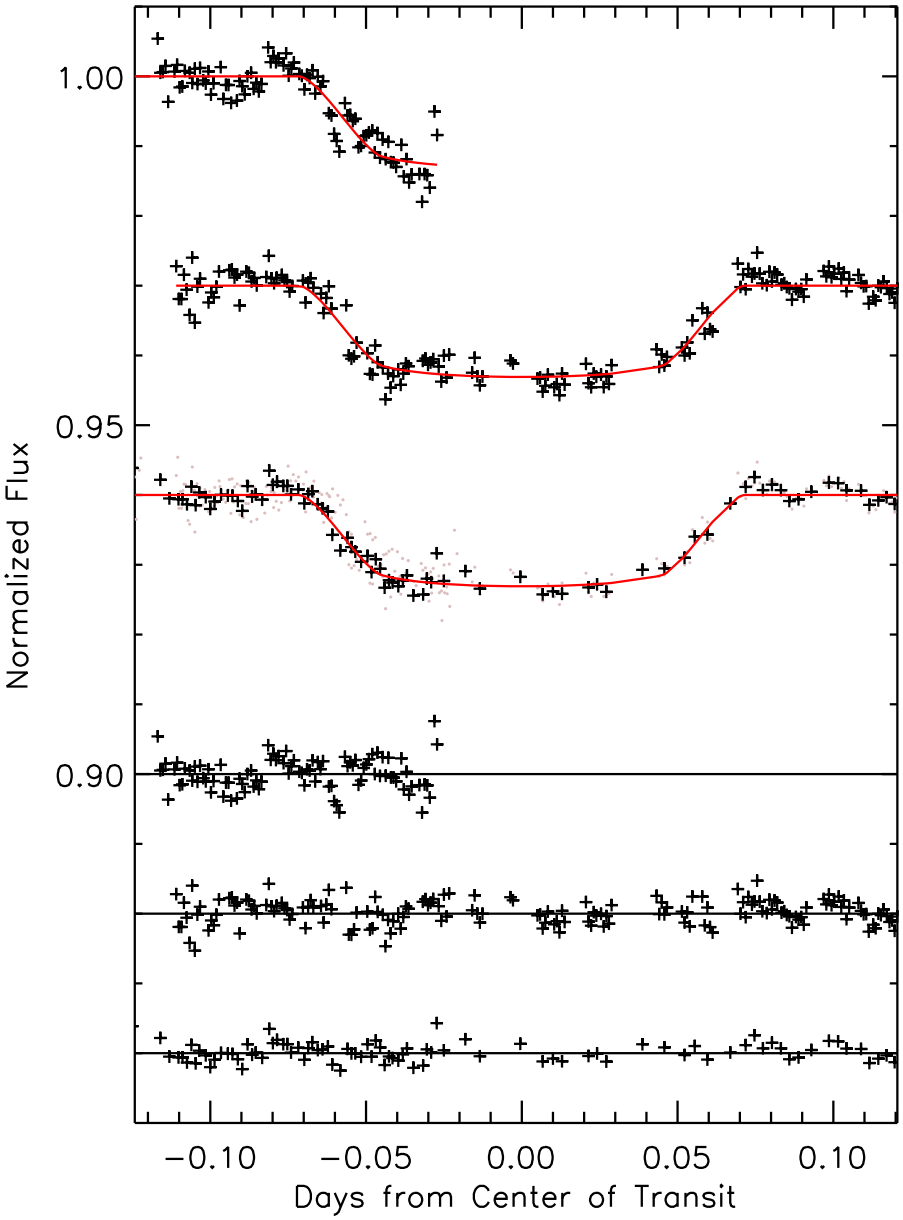

Figure 4.13: Jointly fitted lightcurves of the two observed transits of HAT-P-16b. Individual transits have been offset vertically for clarity. Top to bottom: transits of July 29, August 26-27, and the combined lightcurve of the two transits. For the combined curve all data points are shown in gray, while the black points show the data after binning each 3 data points. Error bars are not shown for clarity.

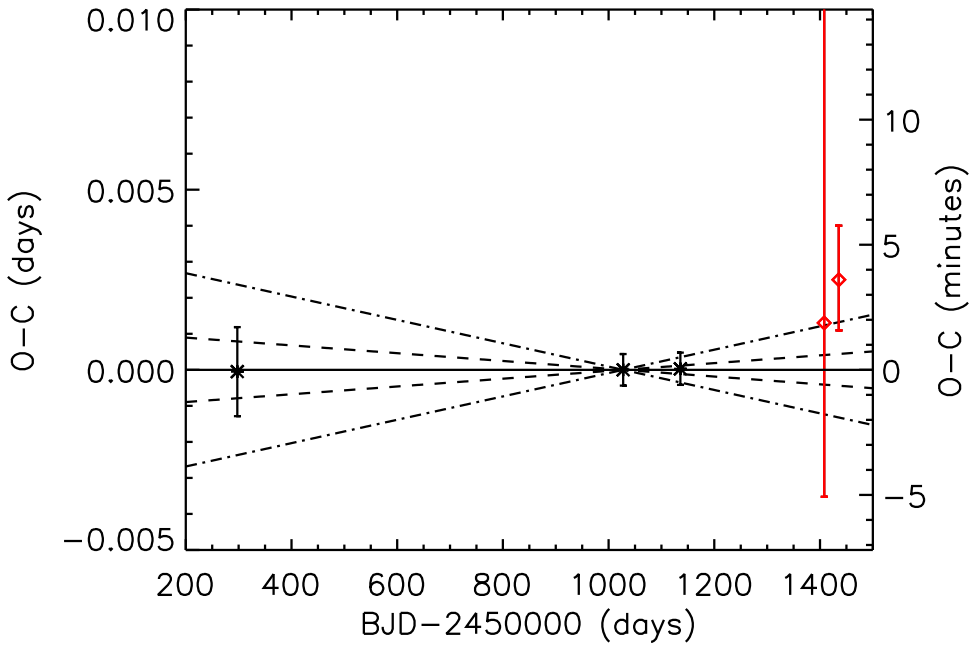

Figure 4.14: $O-C$ diagram for HAT-P-16b, with data from the literature (Buchhave et al. 2010) in black and the VVO observations in red. The transit times and errors are those calculated by TAP. The dashed lines show the level of linear TTVs that would be caused by a 1σ error in the period, while the dash-dotted lines show that from a 3σ error.

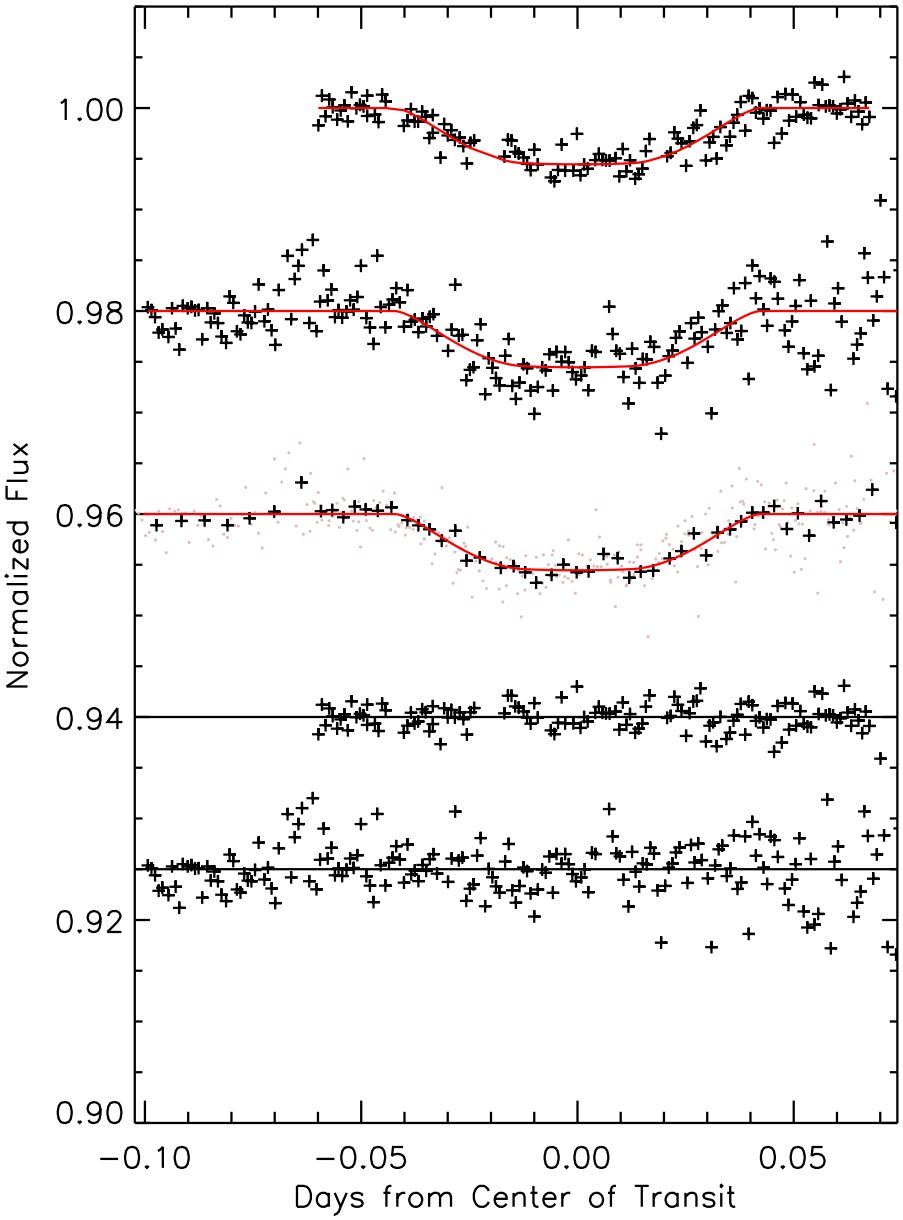

Figure 4.15: Jointly fitted lightcurves of the two observed transits of HAT-P-14b. Individual transits have been offset vertically for clarity. Top to bottom: transits of July 1-2, August 8, and the combined lightcurve of the two transits. For the combined curve all data points are shown in gray, while the black points show the data after binning each 3 data points. Error bars are not shown for clarity.

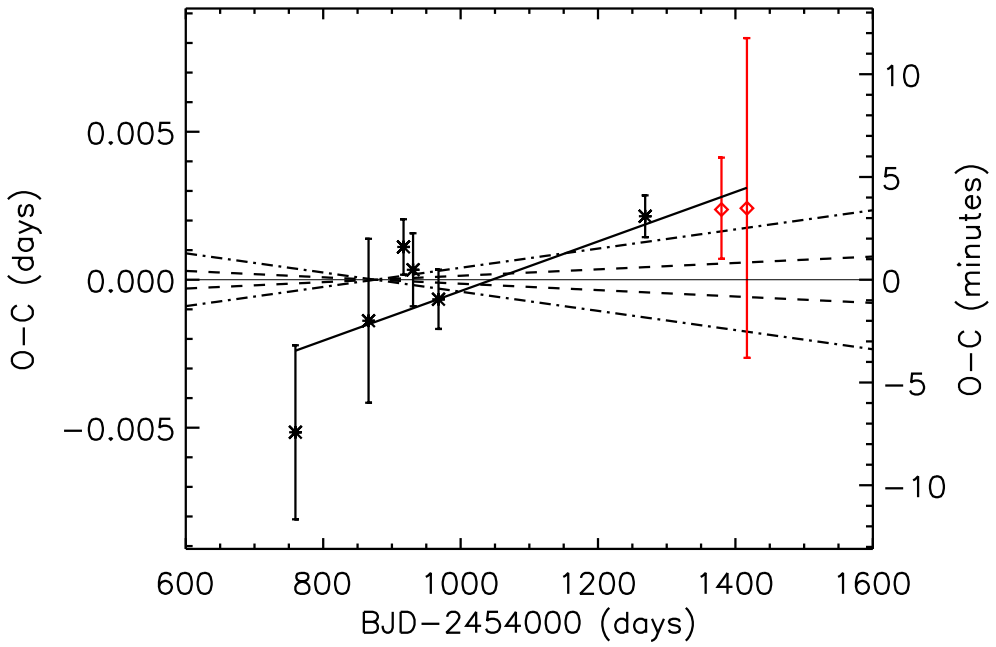

Figure 4.16: $O - C$ diagram for HAT-P-14b, with data from the literature (Torres et al. 2010; Nascimbeni et al. 2011) in black and the VVO observations in red. Transit times and errors are those calculated by TAP. The solid black line shows the best fit to the linear TTVs, resulting in a new period of 4.627696 ± 0.000012 days. The dashed lines show the level of linear TTVs that would be caused by a 1σ error in the period, while the dash-dotted lines show that from a 3σ error.

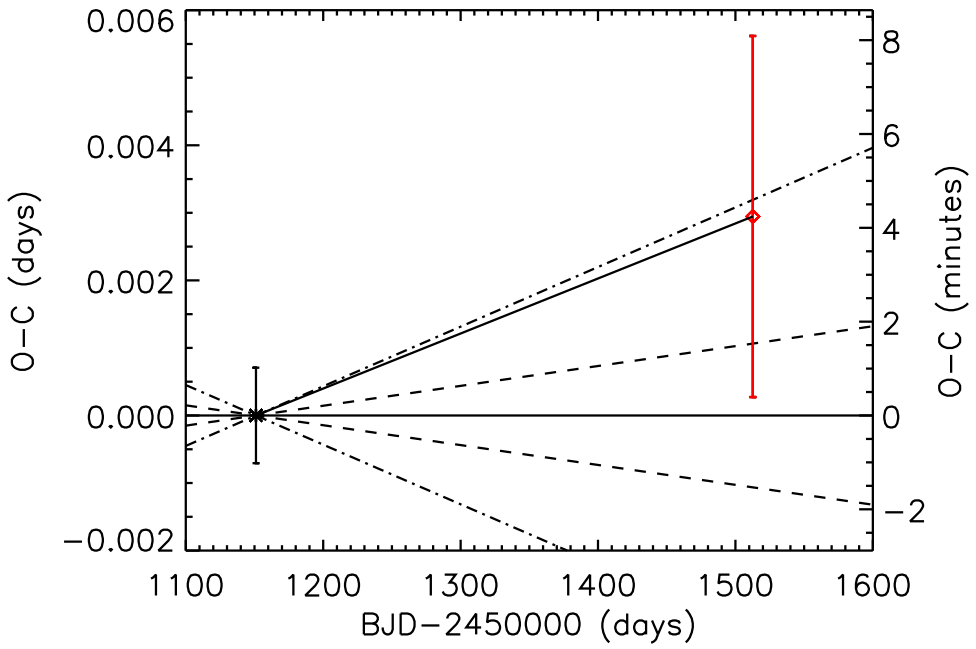

Figure 4.17: $O - C$ diagram for WASP-32b, with data from the literature (Maxted et al. 2010) in black and the VVO observation in red. The transit time and error is that calculated by TAP. The solid black line shows the best fit to the linear TTVs, resulting in a new period of 2.718672 ± 0.000008 days. The dashed lines show the level of linear TTVs that would be caused by a 1σ error in the period, while the dash-dotted lines show that from a 3σ error.

4.3.4 WASP-32b

One transit of WASP-32b was observed; its lightcurve is shown in Fig. 4.3. The $O - C$ diagram is presented in Fig. 4.17. We calculate a new period for this planet of 2.718672 ± 0.000008 days, although this is based on only two data points. Additionally, our one transit observation is only consistent with a period error at a significance of slightly over 1σ, so this result should be taken with some caution. Our calculated period differs from that of Maxted et al. (2010) by 1.6σ.

4.3.5 WASP-2b

Two transits of WASP-2b were observed, as shown in Fig. 4.18; this is perhaps the lowest noise data set for any of the planets with multiple observed transits. The $O - C$ diagram for this planet is presented in Fig. 4.19. No transit timing variations are visible over the baseline of nearly 1500 days, although, given that there are only seven data points over this span, periodic TTVs cannot be entirely excluded. That said, there is no evidence for such variations.

4.3.6 HD 189733b

HD 189733b was one of the first dozen transiting planets to be detected (Bouchy et al. 2005; Schneider 2011), and has been extensively observed. It orbits a very bright star (V=7.67; Schneider 2011), allowing for a high photometric cadence, as is evident in the lightcurve (Fig. 4.1). Additionally, it has been shown to have no detectable TTVs (Agol et al. 2010). Thus, our observed transit should lie along the zero TTV line. As can be seen in Fig. 4.20, our data point does indeed lie very close to the $O - C = 0$ line, which is well within the 1σ error bars.

4.3.7 HAT-P-11b

HAT-P-11b is unique in being the only hot neptune observed thus far at VVO. The transit is very shallow but detectable (Fig. 4.2). Unfortunately this results in a rather imprecise transit time, but this calculated transit centroid is, as shown in Fig. 4.21, just over 1σ away from the $O - C = 0$ line. While this is not particularly significant, it does suggest that HAT-P-11 could be a good target for future observations at VVO.

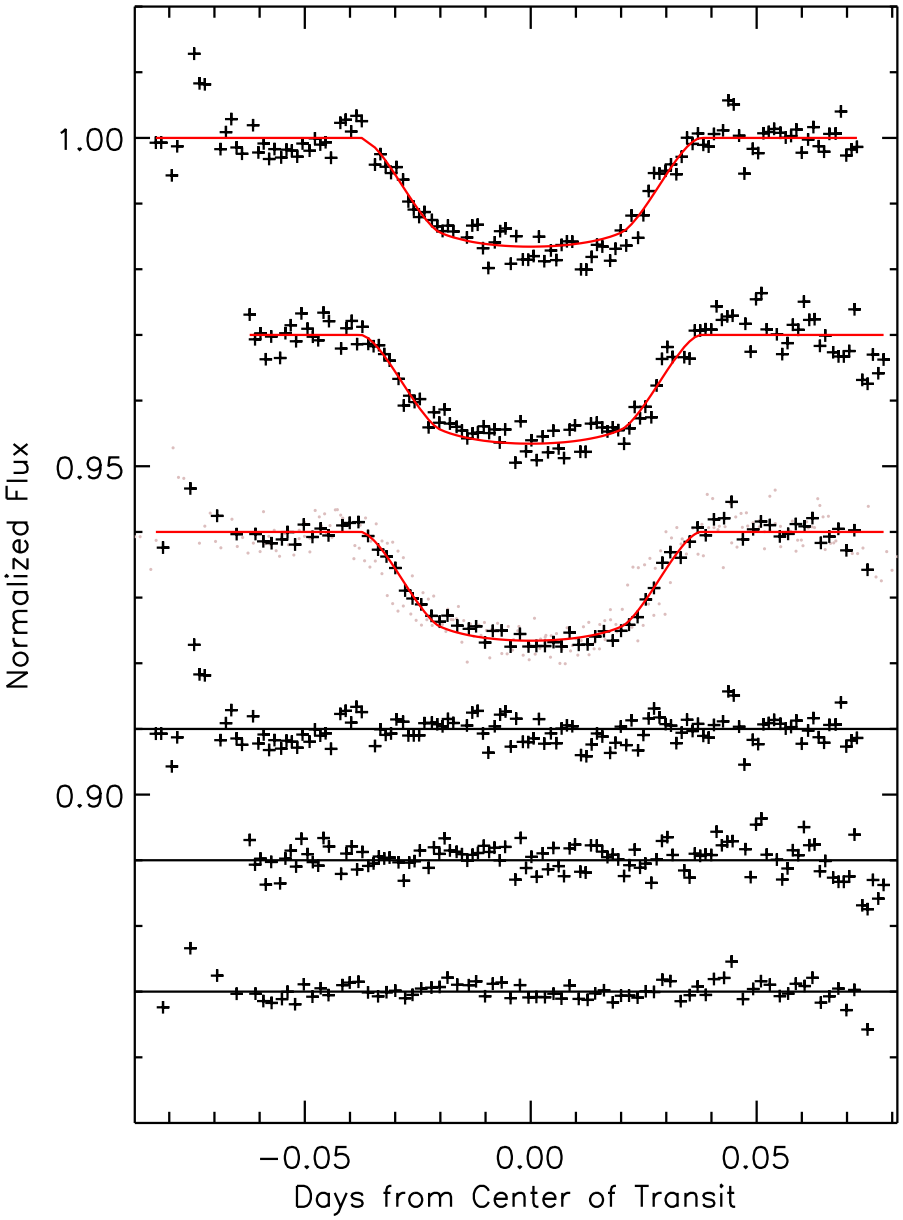

Figure 4.18: Jointly fitted lightcurves of the two observed transits of WASP-2b. Individual transits have been offset vertically for clarity. Top to bottom: transits of July 29-30, August 14, and the combined lightcurve of the two transits. For the combined curve all data points are shown in gray, while the black points show the data after binning each 3 data points. Error bars are not shown for clarity.

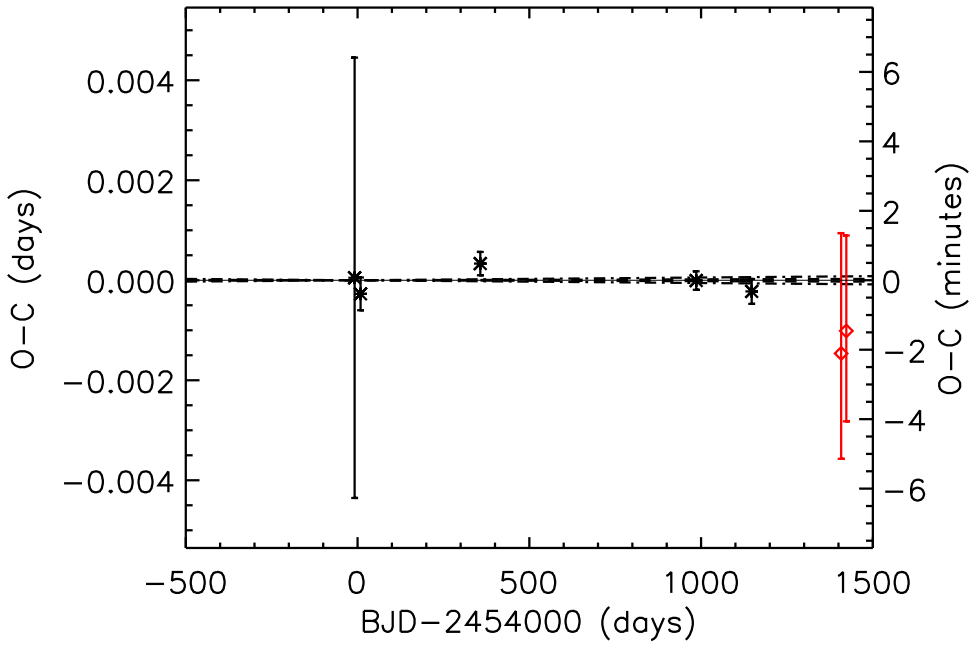

Figure 4.19: O-C diagram for WASP-2b, with data from the literature (Collier Cameron et al. 2007; Charbonneau et al. 2007; Hrudková et al. 2009; Southworth et al. 2010) in black and the VVO observations in red. The transit times and errors are those calculated by TAP. The dashed lines show the level of linear TTVs that would be caused by a 1σ error in the period, while the dash-dotted lines show that from a 3σ error.

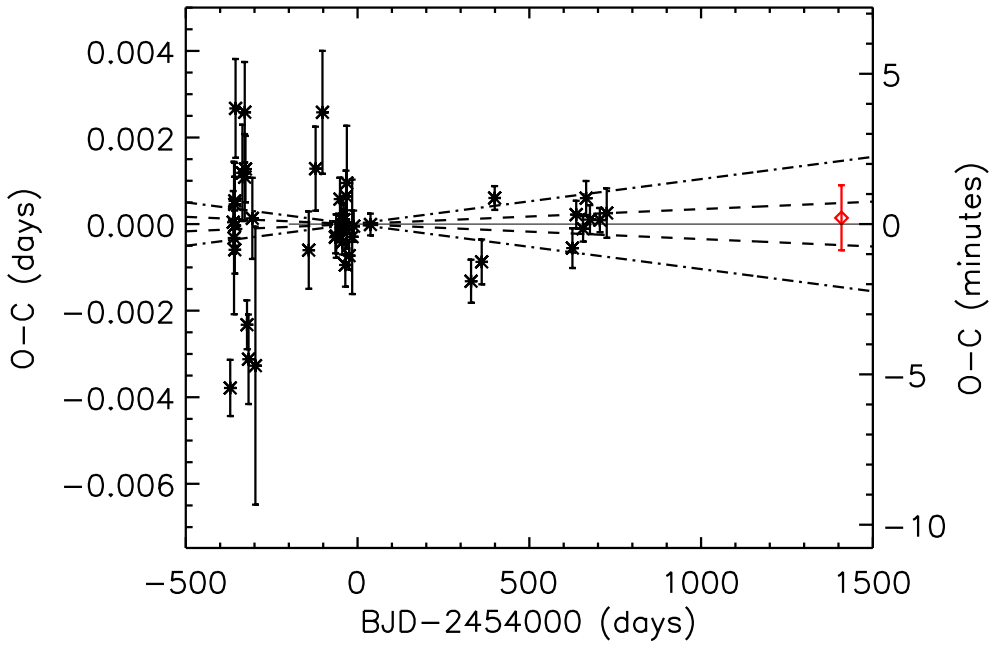

Figure 4.20: O-C diagram for HD189733b, with data from the literature (Bakos et al. 2006; Winn et al. 2007c; Miller-Ricci et al. 2008; Knutson et al. 2009; Hrudková et al. 2010) in black and the VVO observation in red. The transit times and errors are those calculated by TAP. The dashed lines show the level of linear TTVs that would be caused by a 1σ error in the period, while the dash-dotted lines show that from a 3σ error.

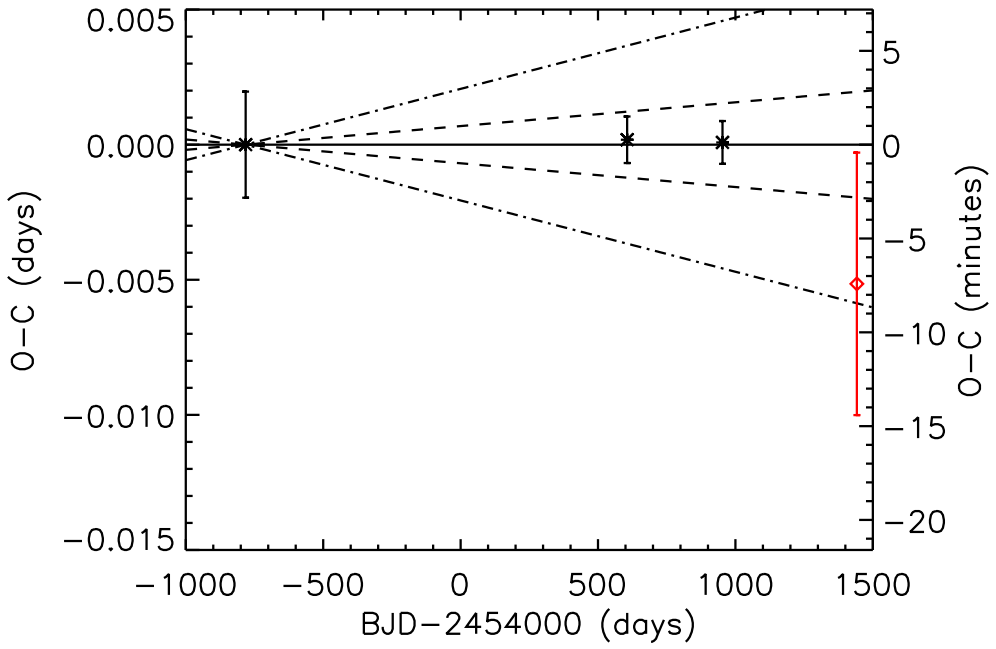

Figure 4.21: $O - C$ diagram for HAT-P-11b, with data from the literature (Bakos et al. 2010a; Dittmann et al. 2009) in black and the VVO observation in red. The transit time and error is that calculated by TAP. The dashed lines show the level of linear TTVs that would be caused by a 1σ error in the period, while the dash-dotted lines show that from a 3σ error.

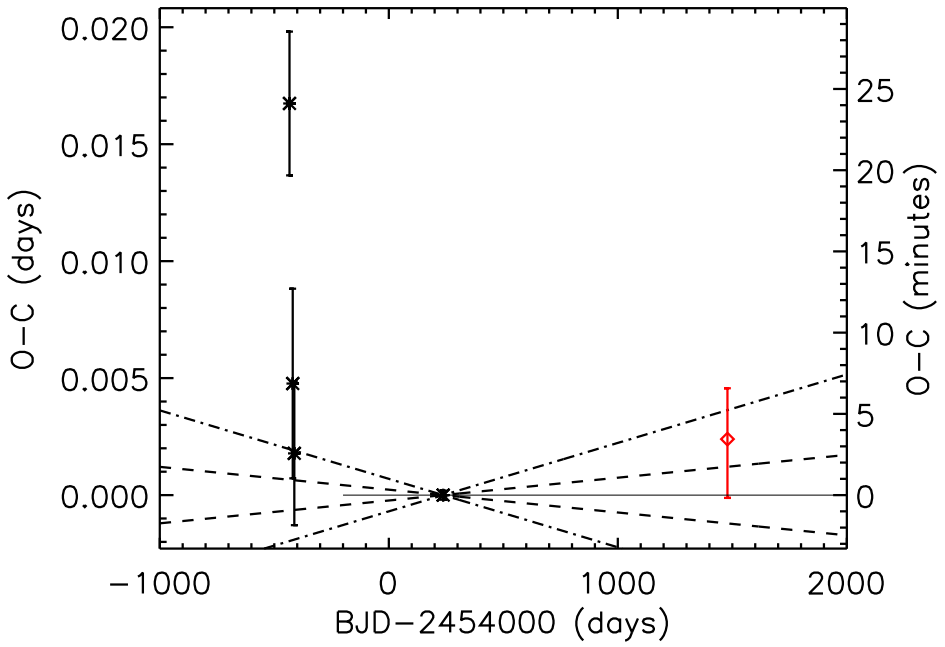

Figure 4.22: $O-$C diagram for CoRoT-Exo-2b, with data from the literature (Rauer et al. 2010; Alonso et al. 2008) in black and the VVO observation in red. The transit time and error is that calculated by TAP. The dashed lines show the level of linear TTVs that would be caused by a 1σ error in the period, while the dash-dotted lines show that from a 3σ error.

4.3.8 CoRoT-Exo-2b

CoRoT-Exo-2b is one of the planets discovered by the European *CoRoT* mission; one transit of this planet was observed at VVO. The lightcurve is shown in Fig. 4.2. Our data are consistent with no TTVs (see Fig. 4.22).

4.3.9 HAT-P-23b

One transit of HAT-P-23b was observed; the lightcurve is shown in Fig. 4.2. No evidence for TTVs is found, as shown in Fig. 4.23, although there are currently only two data points from which to judge.

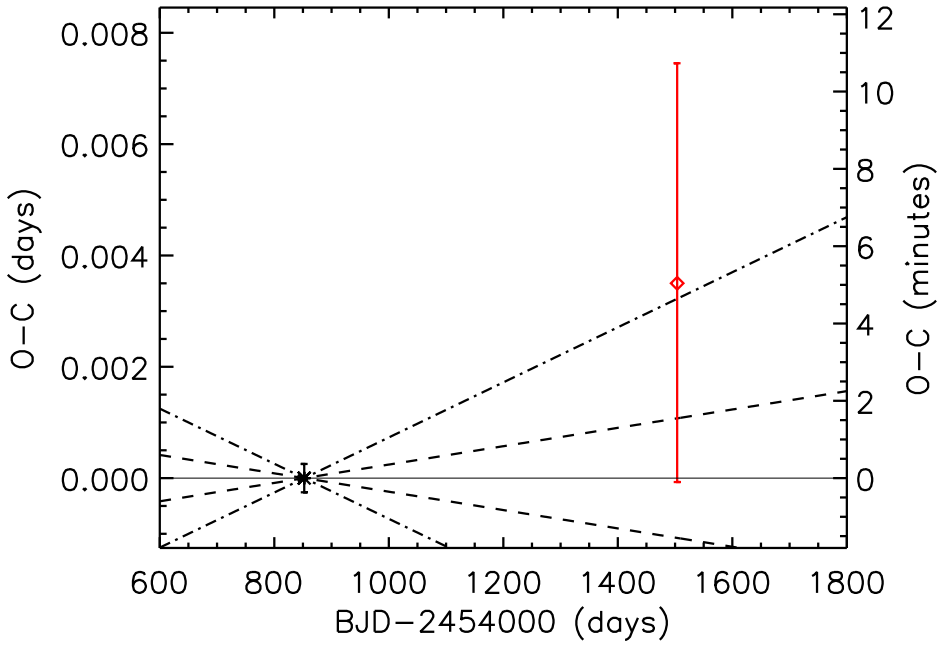

Figure 4.23: $O - C$ diagram for HAT-P-23b, with data from the literature (Bakos et al. 2010b) in black and the VVO observation in red. The transit time and error is that calculated by TAP. The dashed lines show the level of linear TTVs that would be caused by a 1σ error in the period, while the dash-dotted lines show that from a 3σ error.

Chapter 5

Discussion

5.1 WASP-33b

As outlined in §4.2, the significance of the transit timing variation findings for the observed transits of WASP-33b depends strongly upon which fitting and error-reduction method is used. The transit timing variations, if real, could be caused by another planet in the system, which would be a very intriguing result. In at least some cases the TAP error bars appear to be too large; for instance, for the WASP-33b transit of 2010 December 4, the large positive error bar (0.0120 days from the individual fit, 0.61 days from the joint fit; see Fig. 5.1) takes the lightcurve well outside the scatter of data points, assuming a fixed transit duration. We may thus safely regard the TAP error bars as a conservative upper limit. However, are these error bars too large, masking real TTVs?

One method of investigating whether the error bars are appropriate is to compare our observations with observations of the same transits taken at other observatories. The last two WASP-33b transits, those of 2011 January 23 and February 3, were simultaneously observed using the 24" telescope at Swarthmore College's Peter van de Kamp Observatory (E. Jensen, personal communication 2011). A comparison of the respective transit times is currently in progress (J. Sokol, personal communication 2011).

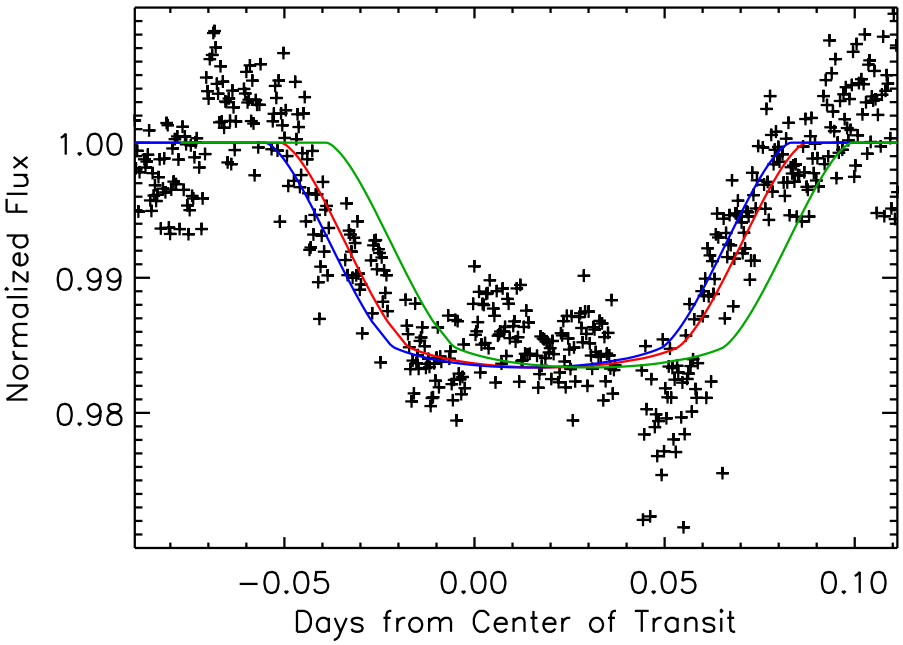

Figure 5.1: WASP-33b transit of 2010 December 4. The red curve shows the best fit lightcurve, while the blue and green curves show the best fit shifted by the negative (−0.0041 days) and positive (+0.012 days) 1σ transit centroid error bar from the TAP individual fit, respectively. The error bar from the TAP joint fit (+0.61 days) is not shown. Photometric error bars are not shown for clarity.

Even if the TTVs are real, many more transit observations will be necessary to fully characterize any perturbing body. Veras et al. (2011) find that > 50 transits, preferably consecutive transits, are necessary to unambiguously characterize a perturbing body. Thus even with collaborations with other observatories it will likely be several years before any firm conclusions can be drawn on this system.

If the TTVs are indeed real, then it is possible that the perturbing body would need to be in a non-resonant orbit in order to produce the frequency of $\sim$14 days found by the periodogram analysis, as suggested by the representative TTV patterns in Fig. 1.8. This should be taken with caution, however, as TTVs depend on the properties of the perturbing body in a complicated manner and it is possible that the mass ratio might be able to influence the TTV period. Qualitatively, it would seem that a higher mass ratio between the perturbing and transiting bodies should result in a greater TTV amplitude. Thus, the larger amplitude of the observed possible TTVs with respect to those shown in Fig. 1.8 suggests that the mass ratio could be greater than that used to compile these figures. In the absence of rigorous dynamical simulations, however, we cannot draw any conclusions with certainty as to the orbital period or mass of a perturbing body from the TTVs alone.

What other effects could possibly cause the TTVs, if not a perturbing planet? Ford & Holman (2007) find that the TTV signature caused by a Trojan planet is similar to that of a perturbing exterior or interior planet, so we cannot exclude this effect *a priori*; however, much more data would be needed to determine whether this is the case. As many examples of resonant or near-resonant planets have been found but thus far no examples of Trojan planets have been found, it seems reasonable to conclude that while this could explain our data, a perturbing exterior planet is the more likely explanation. WASP-33b orbits so close to its host star

that an interior perturber is unlikely. The Applegate effect only applies to cooler, active stars with convective outer layers (Watson & Marsh 2010), whereas WASP-33 is a hot, early-type star which should have radiative outer layers (e.g., Gray 2005). Moreover, the timescale for TTVs caused by the Applegate Effect should be much longer than the span of observations in this work (Watson & Marsh 2010). Weidner & Horne (2010) find that since WASP-33b orbits extremely close to its host star it can only support moons over a small range of radii, and these authors have excluded the presence of moons more massive than $\sim 5 \times 10^{-2} M_{\oplus}$. Precessional effects should change solely the duration of transits, not the timing thereof, and such effects should only be visible over timescales of ∼10 years (Iorio 2010). It thus seems that there is no known astrophysical mechanism except for another planet which could cause the observed TTVs. Unfortunately as we have not been able to find or construct a fitting method which unambiguously gives good results for the error bars, we cannot say what the level of significance of this result may be.

WASP-33b is unique among transiting planets (excluding planet candidates detected by *Kepler*) in that it does not have a radial velocity (RV)-measured mass, but only an upper mass limit, as its hot, fast-rotating host star does not possess the narrow absorption lines required for precise RV measurements (Collier Cameron et al. 2010). However, using this upper limit on the mass of WASP-33b, we can compute the maximum RV semi-amplitude which could exist, and use this to place constraints on the mass of any perturbing planet.

The radial velocity semi-amplitude is, from eqn. 13 of Lovis & Fischer (2010),

$$K = \frac{28.4329 \text{ m s}^{-1}}{\sqrt{1-e^2}} \frac{m_2 \sin i}{M_J} \left(\frac{m_1 + m_2}{M_\odot} \right)^{-2/3} \left(\frac{P}{1 \text{ yr}} \right)^{-1/3} \tag{5.1}$$

where K is the RV semi-amplitude, m_1 and m_2 are the masses of the star and planet, respectively, i is the inclination of the planet's orbit relative to the line of sight, with $i = 90°$ corresponding to edge-on to the line of sight, P is the period of the planet's orbit, and e is the eccentricity of the planet's orbit, with all quantities in the indicated units (M_J is Jupiter masses).

From Smith et al. (2011), the 3σ upper limit on the mass of WASP-33b is 4.59 M_J. According to my calculations, this corresponds to an RV semi-amplitude of $K \sim 666$ m s^{-1}. We cannot simply use this as the maximum amplitude that could be produced by a second planet WASP-33c as well, because now we have *two* signals which must sum to less than this value.

In order to explore the possible range of parameters of a second planet which are consistent with the RV data I conducted a Monte Carlo simulation. This simulation computed the RV signal from the two planets. The mass of WASP-33b and the mass and period of WASP-33c were randomly selected. 4.59 M_J was used as the maximum mass for WASP-33b; for the lower limit I calculated the minimum plausible mass given the known radius. In order to accomplish this I assumed that the minimum mass would be that if WASP-33b had the same density as the planet with the lowest known density. This is WASP-17b, which has a radius of 1.991 ± 0.081 R_J and a mass of 0.486 ± 0.032 M_J (Anderson et al. 2010; Schneider 2011). If WASP-33b had the 1σ lowest density implied by these values then it would have a mass of 0.142 M_J. I therefore adopted this as the minimum mass for WASP-33b for the Monte Carlo.

For WASP-33c, I restricted the period to between the 4:3 mean-motion resonance with WASP-33b and 15 days, as, qualitatively, planets should not be able to produce TTVs with periods much shorter than the orbital period. As a maximum mass I chose that which would produce an RV semi-amplitude of 666 m

s^{-1} at a period of 15 days, i.e., 10.6 M_J. For the minimum mass I arbitrarily chose $\sim 1/3\ M_\oplus$. The values of each of these parameters were selected from a uniform random distribution within these limits. The initial true anomaly f of WASP-33c was also selected randomly from a uniform distribution between 0 and 2π. Additionally, in order to simplify the simulation, I assumed that the orbit of WASP-33c has zero eccentricity and is coplanar with that of WASP-33b. This is not likely to be true in detail, but serves as a useful starting point.

The radial velocity of the star from the two orbiting planets was calculated every 0.1 day over a period of one year. One million realizations of the system were run with parameters randomly selected from within the above limits, and only those which produced a maximum RV semi-amplitude of less than 666 m s^{-1} were selected; ∼390,000 sets of parameters were thus selected.

The results of this Monte Carlo are presented in Fig. 5.2. This figure shows the maximum and median mass for WASP-33c from the selected iterations of the Monte Carlo. Obviously the maximum possible masses for WASP-33c correspond to the minimum possible masses and therefore minimum possible densities for WASP-33b, so a more realistic maximum mass is likely lower than this line.

We can also put some limits on WASP-33c from the transit data. As defined in eqn. 7 of Winn (2010), the impact parameter b is, for zero eccentricity,

$$b = \frac{a \cos i}{R_S} \tag{5.2}$$

where a is the semi-major axis, i is the inclination and R_S is the radius of the star. The impact parameter measures the minimum sky-projected separation between the centers of the star and the planet in units of stellar radii. Thus (for $R_P \ll R_S$), if $b \leq 1$ a transit will occur, whereas for $b > 1$ no transit will occur.

We can use this to find at what radius WASP-33c would cease to transit if it was coplanar with WASP-33b. With this condition I calculate that WASP-33c would transit if it was at $a < 0.165$ AU, or $P < 20.0$ days. Thus, if coplanar with WASP-33b, WASP-33c would likely need to have a radius of approximately Neptune size or smaller in order to have escaped detection by SuperWASP. Of course, given WASP-33b's highly inclined orbit there is no *a priori* reason to expect that WASP-33c would have to be coplanar with the inner planet. In order to illustrate the implications for this, in Fig. 5.3 I illustrate the probability that WASP-33c would transit for random inclination, assuming that $R_c \ll R_S$, $m_c \ll M_S$ (calculated using eqn. 11 of Winn 2010). There is significant ($\sim 20\%$) transit probability near the inner mean-motion resonances, but it drops to $< 10\%$ farther from the star.

Ideally we would compute synthetic $O-C$ diagrams and compare them to our data, and use this to constrain the properties of any perturbing body and compare these values to the maximum masses found by the Monte Carlo. Unfortunately we do not currently have the time to conduct this sort of analysis. A faster method would be to use the TTV inversion method of Nesvorný & Beaugé (2010), but their code is not publicly available and we do not have the time to write our own implementation of their algorithm, presented in Nesvorný & Morbidelli (2008).

We can only infer so much from the limited amount of data we have—our six transits, plus the six from the literature (Collier Cameron et al. 2010; Smith et al. 2011; Herrero et al. 2011). The only way to determine conclusively if the TTVs are real or not is to obtain data on more WASP-33b transits. Unfortunately the 2010-2011 WASP-33 observing season has ended (see Table 2.6), and the next transit will not occur until July of 2011. Once this occurs, however, I recommend that WASP-33 be one of the highest priority targets for WesTEP, as well as for our collaborators at other institutions. Up to four observatories could participate

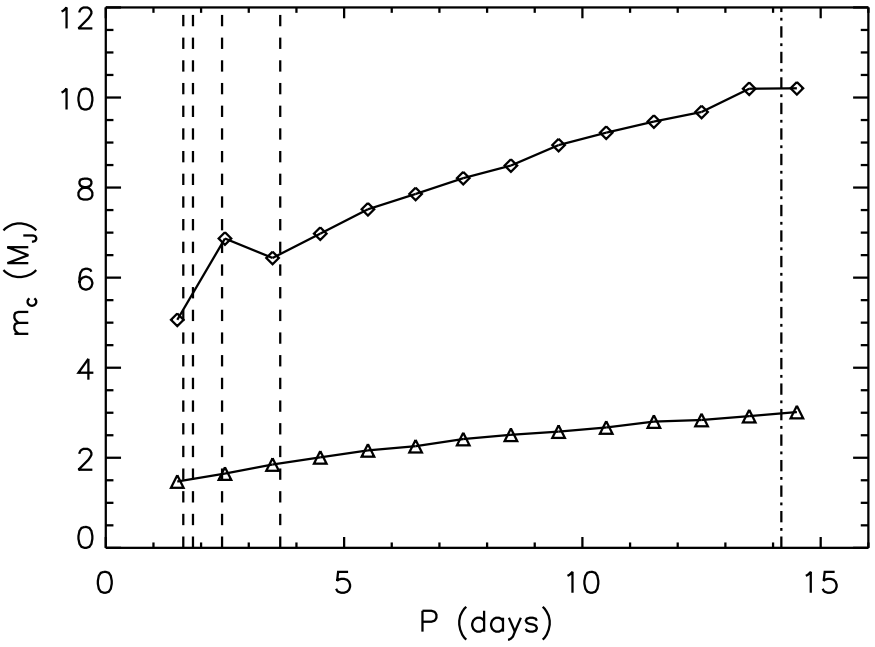

Figure 5.2: Masses of WASP-33c as a function of period from the Monte Carlo described in the text. The diamonds show the maximum mass for WASP-33c in each bin, while the triangles show the median mass for each bin. The bins size is 1 day, and the points are displayed in the center of each bin. The vertical dashed lines display the locations of (from left to right) the 4:3, 3:2, 2:1, and 3:1 mean-motion resonances with respect to WASP-33b, while the dash-dotted line displays the location of the 14.1739 day period found by the Lomb-Scargle periodogram (see Fig. 4.8).

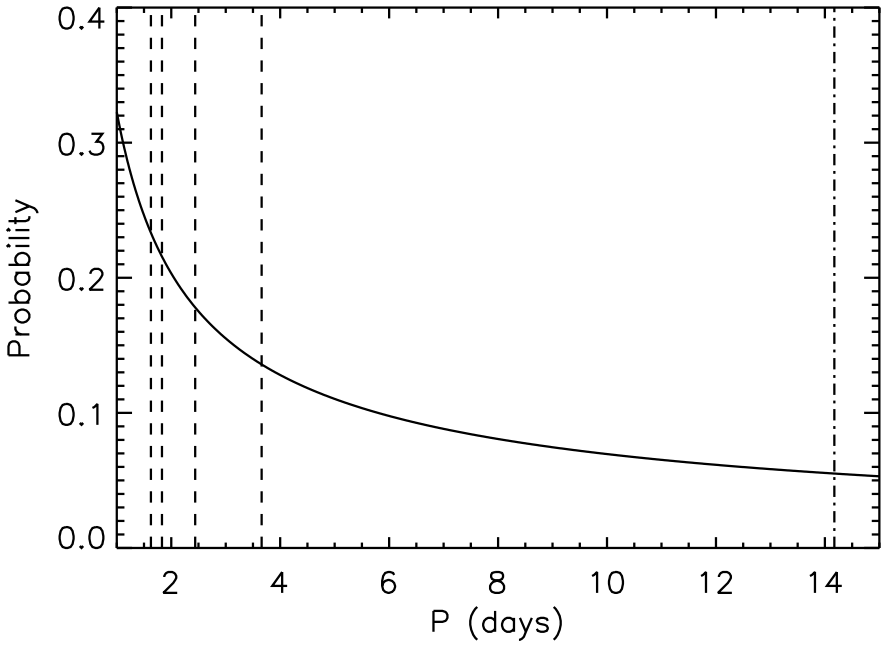

Figure 5.3: Transit probability of WASP-33c for random inclination, assuming $R_c \ll R_S$, $m_c \ll M_S$. The vertical dashed lines display the locations of (from left to right) the 4:3, 3:2, 2:1, and 3:1 mean-motion resonances with respect to WASP-33b, while the dash-dotted line displays the location of the 14.1739 day period found by the Lomb-Scargle periodogram (see Fig. 4.8).

in this program (VVO and the observatories of Swarthmore College, Appalachian State University, and Pomona College; E. Jensen, D. Caton, P. Choi, private communications, all 2011). With these four sites observing, I estimate that it would still take 1-2 more years to gather the ~ 50 transits found to be necessary by Veras et al. (2011) to confidently calculate the properties of a perturbing planet.

Should there turn out to be a perturbing planet WASP-33c, it could allow the mass of WASP-33b to be determined even without radial velocity data, as has been done for five of the six planets around Kepler-11 (Lissauer et al. 2011a). Additionally, as WASP-33b exists on a highly inclined orbit ($\sim 250^\circ$ angle between the sky-projected stellar rotation and planetary orbital angular momentum vectors; Collier Cameron et al. 2010), it would be intriguing to find the angle between the orbital plane of a perturbing planet and that of WASP-33b. This would likely have important consequences for the orbital migration mechanism that caused WASP-33b to end up on such a highly inclined orbit.

5.2 WASP-3b

WASP-3b is one of our most intriguing targets, as Maciejewski et al. (2010a) published data indicating periodic TTVs in this system. Our two data points on this system are consistent with the periodic TTVs found by these authors (see Fig. 4.12). However, the more recent data of Christiansen et al. (2011) appear to not precisely fit the Maciejewski et al. (2010a) TTVs, as also displayed in that figure. It thus appears that, at minimum, the period of the TTVs must be adjusted.

Our observations have been part of the follow-up effort in collaboration with Maciejewski et al., and our two transits will form part of their further analysis of the system which will no doubt be published at some future date. Thus the final

conclusions on the existence of WASP-3c must be deferred to that publication.

5.3 HAT-P-16b

While the case for transit timing variations in WASP-33b is unclear, we have some evidence for TTVs for HAT-P-16b, with one of our two points lying $\sim 1.8\sigma$ from the zero TTV line (see Fig. 4.14); the other point, derived from a partial transit, has a large error and is not particularly reliable. Given that the somewhat deviant point and error are from TAP, which, as argued earlier, should be regarded as an upper limit on the error, this result is marginally significant. While with only five data points it is too early to draw any conclusions, there exists the intriguing possibility that this TTV is due to another planet in the system. However, given that the three literature points all lie along the zero TTV line, this should still be taken with some caution. It is clear, however, that HAT-P-16b is a promising target for future transit observations at VVO.

5.4 HAT-P-14b and WASP-32b

We have calculated new periods for two planets, HAT-P-14b and WASP-32b. Our new periods deviate from the previously-calculated periods by less than 2σ. For HAT-P-14b, due to the larger size of our errors relative to those of Torres et al. (2010) or Nascimbeni et al. (2011) our calculated period is actually less precise than those of these authors. Future observations at VVO and elsewhere will help to further refine the orbital periods of these planets.

5.5 Other Systems

We find no evidence of TTVs in any of the other systems which we have observed. This null result, particularly for HD 189733b, which has been demonstrated not to show any TTVs, shows that our data are reliable. If we had seen any TTVs in this system it would have been an indication that some part of our data collection and reduction pipeline was not working properly.

Indeed, the calculated mid-transit time for HD 189733b is very close ($\sim 0.2\sigma$) to the $O - C = 0$ line, leaving room for the error bars to be significantly smaller and still be consistent with zero TTVs. The two WASP-2b points, however, also in a system in which no TTVs have been found (although much less data are available), are $\sim 0.5 - 0.7\sigma$ away from $O - C = 0$. Here there is less room to argue for a reduction of the error bars. Thus it appears that the error bars are, in general, likely not more than $\sim 1.5 - 2\times$ too large.

Chapter 6

Conclusions and Future Work

6.1 Conclusions

After millenia of speculation, humanity has, in the last two decades, entered the era in which we know of planets around other stars. With the recent launch of the *Kepler* mission and the deluge of planet candidates that it has detected, as well as the increased use of follow-up techniques such as measurements of TTVs, TDVs, and transmission spectroscopy, it appears that exoplanetary science is currently entering a golden age.

We have shown that observations on a relatively small telescope in a nonoptimal observing location such as Connecticut can still return relatively precise data on exoplanetary transits, which can be used to search for transit timing variations. We find preliminary suggestions of TTVs for two planets, WASP-33b and HAT-P-16b, and further refine the periods of two more planets, HAT-P-14b and WASP-32b. In addition, we have contributed to the follow-up observations on a report of periodic TTVs of WASP-3b.

Thus, small telescopes such as those operated by Wesleyan can clearly have an impact on the follow-up observations of newly discovered exoplanets; as the rate of planetary discoveries increases there will be insufficient large telescope resources to follow up all new planets, making this a valuable niche to fill. No

doubt WesTEP will notch up many more successes in the years to come.

6.2 Future Work

While WesTEP is now operational, there remains much work to be done. Currently work is in progress to add an autoguider to the 24", alleviating the need for manual guiding. This will improve the data as the PSF will now remain on a very small set of pixels, and will also improve the duty cycle, eliminating gaps in data due to recentering (see the WASP-33b transit of 2010 October 10-11, Fig. 4.4). This system may be in place as soon as the 2011-2012 observing season. (J. Schaeffer, personal communication 2011). Another field for experimentation could be to only read out part of the CCD chip, decreasing the readout time and increasing the duty cycle and observing cadence.

Additional improvements can also be made in the reduction and transit fitting pipeline. As noted earlier, the fitting routine could be adapted to properly fit transits of planets with non-zero eccentricities. The aperture photometry process could also be optimized to adaptively select the aperture that results in the lowest RMS of the residuals. Finally, a differential airmass correction routine could be implemented, to correct for the fact that the target and comparison stars do not have precisely the same airmass, a relationship that changes over the course of an observation (W. Herbst, private communication 2010).

Our work on exoplanetary transits can be strengthened by collaborations with astronomers at other institutions. Simultaneous observations of the same transit can help to evaluate the proper size of the error bars and thus to obtain more precise transit centroids. Conversely, observations at multiple observatories can observe more transits; if one observatory is clouded out for a given transit the oth-

ers will not necessarily be. Additionally, observatories widely spaced in longitude can observe a greater range of transits, as one observatory will be able to observe a transit that is lost in twilight at another location. We have been actively collaborating with colleagues at Swarthmore College/Peter van de Kamp Observatory (E. Jensen, private communications 2010, 2011) and Appalachian State University (D. Caton, private communication 2011). Additionally, a transit program is being initiated at Pomona College (P. Choi, private communication 2011), which may be operational by the start of the next WASP-33b transit season.

Bibliography

Agol, E., Cowan, N. B., Knutson, H. A., Deming, D., Steffen, J. H., Henry, G. W., & Charbonneau, D. 2010, ApJ, 721, 1861

Agol, E., Steffen, J., Sari, R., & Clarkson, W. 2005, MNRAS, 359, 567

Alonso, R. et al. 2008, A&A, 482, L21

Anderson, D. R., Hellier, C., Gillon, M., Triaud, A. H. M. J., Smalley, B., Hebb, L., Collier Cameron, A., Maxted, P. F. L., Queloz, D., West, R. G., Bentley, S. J., Enoch, B., Horne, K., Lister, T. A., Mayor, M., Parley, N. R., Pepe, F., Pollacco, D., Ségransan, D., Udry, S., & Wilson, D. M. 2010, ApJ, 709, 159

Andrae, R., Schulze-Hartung, T., & Melchior, P. 2010, ArXiv e-prints: 1012.3754

Applegate, J. H. 1992, ApJ, 385, 621

Bakos, G., Noyes, R. W., Kovács, G., Stanek, K. Z., Sasselov, D. D., & Domsa, I. 2004, PASP, 116, 266

Bakos, G. Á. et al. 2006, ApJ, 650, 1160

—. 2010a, ApJ, 710, 1724

—. 2010b, ArXiv e-prints: 1008.3388

Bean, J. L., Kempton, E., & Homeier, D. 2010, Nature, 468, 669

Beaulieu, J. P. et al. 2010, MNRAS, 409, 963

Beuermann, K. et al. 2010, A&A, 521, L60

Borucki, W. J. et al. 2011, ArXiv e-prints: 1102.0541

Bouchy, F. et al. 2005, A&A, 444, L15

Bruno, G. 1584, De l'infinito universo et Mondi

Buchhave, L. A. et al. 2010, ApJ, 720, 1118

Carter, J. A. & Winn, J. N. 2009, ApJ, 704, 51

Charbonneau, D., Brown, T. M., Latham, D. W., & Mayor, M. 2000, ApJL, 529, L45

Charbonneau, D., Winn, J. N., Everett, M. E., Latham, D. W., Holman, M. J., Esquerdo, G. A., & O'Donovan, F. T. 2007, ApJ, 658, 1322

Chauvin, G., Lagrange, A., Dumas, C., Zuckerman, B., Mouillet, D., Song, I., Beuzit, J., & Lowrance, P. 2004, A&A, 425, L29

Christiansen, J. L. et al. 2011, ApJ, 726, 94

Claret, A. 2000, A&A, 363, 1081

Claret, A., Diaz-Cordoves, J., & Gimenez, A. 1995, AAS, 114, 247

Collier Cameron, A. et al. 2007, MNRAS, 375, 951

—. 2010, MNRAS, 407, 507

Colon, K. D., Ford, E. B., Redfield, S., Fortney, J. J., Shabram, M., Deeg, H. J., & Mahadevan, S. 2010, ArXiv e-prints: 1008.4800

Croll, B., Lafreniere, D., Albert, L., Jayawardhana, R., Fortney, J. J., & Murray, N. 2011, AJ, 141, 30

Crossfield, I. J. M., Hansen, B. M. S., Harrington, J., Cho, J., Deming, D., Menou, K., & Seager, S. 2010, ApJ, 723, 1436

Dittmann, J. A., Close, L. M., Green, E. M., Scuderi, L. J., & Males, J. R. 2009, ApJL, 699, L48

Dittmann, J. A., Close, L. M., Scuderi, L. J., Turner, J., & Stephenson, P. C. 2010, ArXiv e-prints: 1006.3580

Dyson, F. W., Eddington, A. S., & Davidson, C. 1920, Royal Society of London Philosophical Transactions Series A, 220, 291

Eastman, J., Siverd, R., & Gaudi, B. S. 2010, PASP, 122, 935

Einstein, A. 1936, Science, 84, 506

Epicurus. 300 B.C.E., Letter to Herodotus

Ford, E. B. & Holman, M. J. 2007, ApJL, 664, L51

Gatewood, G. & Eichhorn, H. 1973, AJ, 78, 769

Gaudi, B. S. et al. 2008, Science, 319, 927

Gazak, J. Z., Johnson, J. A., Tonry, J., Eastman, J., Mann, A. W., & Agol, E. 2011, ArXiv e-prints: 1102.1036

Gibson, N. P. et al. 2008, A&A, 492, 603

Gilliland, R. L. et al. 2010, ApJL, 713, L160

Gray, D. F. 2005, Stellar Photospheres (Cambridge: Cambridge University Press)

Herbst, W., LeDuc, K., Hamilton, C. M., Winn, J. N., Ibrahimov, M., Mundt, R., & Johns-Krull, C. M. 2010, AJ, 140, 2025

Herrero, E., Morales, J. C., Naves, R., & Ribas, I. 2011, A&A, 526, L10

Holman, M. J. & Murray, N. W. 2005, Science, 307, 1288

Holman, M. J., Winn, J. N., Latham, D. W., O'Donovan, F. T., Charbonneau, D., Bakos, G. A., Esquerdo, G. A., Hergenrother, C., Everett, M. E., & Pál, A. 2006, ApJ, 652, 1715

Holman, M. J. et al. 2010, Science, 330, 51

Horne, J. H. & Baliunas, S. L. 1986, ApJ, 302, 757

Hrudková, M., Skillen, I., Benn, C., Pollacco, D., Gibson, N., Joshi, Y., Harmanec, P., & Tulloch, S. 2009, in Proc. IAU Symp. 253, 446

Hrudková, M., Skillen, I., Benn, C. R., Gibson, N. P., Pollacco, D., Nesvorný, D., Augusteijn, T., Tulloch, S. M., & Joshi, Y. C. 2010, MNRAS, 403, 2111

Iorio, L. 2010, ApSS, 331, 485

Jacob, W. S. 1855, MNRAS, 15, 228

Janson, M., Bergfors, C., Goto, M., Brandner, W., & Lafrenière, D. 2010, ApJL, 710, L35

Kalas, P., Graham, J. R., Chiang, E., Fitzgerald, M. P., Clampin, M., Kite, E. S., Stapelfeldt, K., Marois, C., & Krist, J. 2008, Science, 322, 1345

Kipping, D. & Bakos, G. 2011, ApJ, 730, 50

Kipping, D. M. 2009, MNRAS, 392, 181

Knutson, H. A., Charbonneau, D., Cowan, N. B., Fortney, J. J., Showman, A. P., Agol, E., Henry, G. W., Everett, M. E., & Allen, L. E. 2009, ApJ, 690, 822

Knutson, H. A., Charbonneau, D., Noyes, R. W., Brown, T. M., & Gilliland, R. L. 2007, ApJ, 655, 564

Konon, J. 2008, Master's Thesis, Wesleyan University

Latham, D. W. et al. 2011, ArXiv e-prints: 1103.3896

Leiner, E. M. 2010, Honors Thesis, Wesleyan University

Lissauer, J. J. et al. 2011a, Nature, 470, 53

—. 2011b, ArXiv e-prints: 1102.0543

Lovis, C. & Fischer, D. A. 2010, in Exoplanets, ed. S. Seager (Tucson: University of Arizona Press), 27–53

Lovis, C. et al. 2011, A&A, 528, 112

Maciejewski, G., Dimitrov, D., Neuhäuser, R., Niedzielski, A., Raetz, S., Ginski, C., Adam, C., Marka, C., Moualla, M., & Mugrauer, M. 2010a, MNRAS, 407, 2625

Maciejewski, G. et al. 2010b, MNRAS, 411, 1204

Mandel, K. & Agol, E. 2002, ApJ, 580, L171

Marcy, G. W., Butler, R. P., Vogt, S. S., Fischer, D. A., Henry, G. W., Laughlin, G., Wright, J. T., & Johnson, J. A. 2005, ApJ, 619, 570

Marois, C., Macintosh, B., Barman, T., Zuckerman, B., Song, I., Patience, J., Lafrenière, D., & Doyon, R. 2008, Science, 322, 1348

Marois, C., Zuckerman, B., Konopacky, Q. M., Macintosh, B., & Barman, T. 2010, Nature, 468, 1080

Maxted, P. F. L. et al. 2010, PASP, 122, 1465

Mayor, M. & Queloz, D. 1995, Nature, 378, 355

McArthur, B. E., Benedict, G. F., Barnes, R., Martioli, E., Korzennik, S., Nelan, E., & Butler, R. P. 2010, ApJ, 715, 1203

Miller-Ricci, E. et al. 2008, ApJ, 682, 593

Naef, D. et al. 2001, A&A, 375, L27

Nascimbeni, V., Piotto, G., Bedin, L. R., & Damasso, M. 2011, A&A, 527, 85

Nelder, J. A. 1965, Computer Journal, 7, 308

Nesvorný, D. & Beaugé, C. 2010, ApJL, 709, L44

Nesvorný, D. & Morbidelli, A. 2008, ApJ, 688, 636

Pál, A., Sárneczky, K., Szabó, G. M., Szing, A., Kiss, L. L., Mezö, G., & Regály, Z. 2011, MNRAS, in press

Payne, M. J., Ford, E. B., & Veras, D. 2010, ApJL, 712, L86

Pejcha, O. 2008, Exoplanet Transit Parameters from Amateur-Astronomers Observations, http://var2.astro.cz/ETD/FitProcedureDescription-Pejcha2008.pdf

Pollacco, D. et al. 2008, MNRAS, 385, 1576

Pollacco, D. L. et al. 2006, PASP, 118, 1407

Press, W. H. 1988, Numerical Recipes in C: The Art of Scientific Computing (New York: Cambridge University Press)

Rauer, H. et al. 2010, AJ, 139, 53

Redfield, S., Endl, M., Cochran, W. D., & Koesterke, L. 2008, ApJL, 673, L87

Scargle, J. D. 1982, ApJ, 263, 835

Schneider, J. 2011, The Extrasolar Planets Encyclopaedia, exoplanet.eu

Silvotti, R. et al. 2007, Nature, 449, 189

Simon, A., Szatmáry, K., & Szabó, G. M. 2007, A&A, 470, 727

Sing, D. K. et al. 2011, A&A, 527, 73

Smith, A. M. S., Anderson, D. R., Skillen, I., Cameron, A. C., & Smalley, B. 2011, ArXiv e-prints: 1101.2432

Southworth, J., Wheatley, P. J., & Sams, G. 2007, MNRAS, 379, L11

Southworth, J. et al. 2009, MNRAS, 396, 1023

—. 2010, MNRAS, 408, 1680

Steele, I. A., Bates, S. D., Gibson, N., Keenan, F., Meaburn, J., Mottram, C. J., Pollacco, D., & Todd, I. 2008, in Presented at the Society of Photo-Optical Instrumentation Engineers (SPIE) Conference, Vol. 7014, Society of Photo-Optical Instrumentation Engineers (SPIE) Conference Series

Swain, M. R., Vasisht, G., & Tinetti, G. 2008, Nature, 452, 329

Tegmark, M. et al. 2004, Phys.Rev.D, 69, 103501

Torres, G. et al. 2010, ApJ, 715, 458

Tripathi, A. et al. 2010, ApJ, 715, 421

van de Kamp, P. 1963, AJ, 68, 515

—. 1969, AJ, 74, 757

Veras, D., Ford, E. B., & Payne, M. J. 2011, ApJ, 727, 74

Vidal-Madjar, A., Lecavelier des Etangs, A., Désert, J., Ballester, G. E., Ferlet, R., Hébrard, G., & Mayor, M. 2003, Nature, 422, 143

Watson, C. A. & Marsh, T. R. 2010, MNRAS, 405, 2037

Weidner, C. & Horne, K. 2010, A&A, 521, 76

Winn, J. N. 2010, in Exoplanets, ed. S. Seager (Tucson: University of Arizona Press), 55–77

Winn, J. N., Holman, M. J., & Fuentes, C. I. 2007a, AJ, 133, 11

Winn, J. N., Holman, M. J., & Roussanova, A. 2007b, ApJ, 657, 1098

Winn, J. N. et al. 2007c, AJ, 133, 1828

Wolszczan, A. & Frail, D. A. 1992, Nature, 355, 145